Formation and characterization of metal nanoparticle

coatings on oxide nanospheres

Dissertation

zur Erlangung des akademischen Grades

Doctor rerum naturalium (Dr. rer. nat.)

vorgelegt der

Mathematisch-Naturwissenschaftlich-Technische Fakultät
(mathematisch-naturwissenschaftlicher Bereich)
der Martin-Luther-Universität Halle-Wittenberg

von Herrn Paul - Tiberiu Miclea
geb.: 23.01.1971 in: Petrosani

Gutachter:

1. Doz. Dr. Manfred Dubiel

2. Prof. Dr. Urlich Gösele

3. Prof. Dr. Friedrich Huisken

Halle (Saale), am 24. Juni 2002

To my wife

Manuela

Contents

List of Figures

List of Tables

1 Introduction

This work is dedicated to the study of small metal particles (nanoparticles) deposited on the surface of small non-coherent oxide grains of spherical shape (nanospheres) with the aim of forming core-shell structures. This issue was intensively studied in the last years because such structures exhibit peculiar properties which make them attractive for applications in optical and biological sensors and in optoelectronics. The attenuation of light through composite materials containing metal particles is governed by collective surface plasmon modes. The optical properties depend, besides size and shape of the metal particles, rather sensitively on their surrounding, i. e., the dielectric medium, as well as on their arrangement. Novel optical effects are expected from appropriately combining matrix material and specific ways of particle arrangements, such as aggregate structures or core-shell structures. For these particular geometries oxide nanospheres of nearly equal size are well suited as building blocks of prospective nanostructured materials, offering a great flexibility of composition.

Different from metal deposition on planar substrates, uniform coating of oxide nanospheres requires access of the deposit from all directions. Deposition from solution by chemical means with metal particle formation directly on the oxide surface is right appropriate to this purpose. A corresponding route of synthesis is approached in several steps under consideration of two main determinations: it should avoid uncontrolled surface chemical interaction of the metal particles with functionalizing agents which seriously may influence the surface plasmon resonances, and it should enable control of the metal precursor decomposition kinetics, and therefore the particle size, at moderate temperature conditions.

The thesis consist of six chapters which present fundamental and experimental aspects of metal nanoparticles deposited on various kinds of non-planar oxide substrates. The experimental results are explained and sustained by theoretical calculations in order to fit analytical and numerical models to the experimental data.

In Chapter 2 the physical properties of small metal particles are presented from a structural, morphological and electronic point of view. The conditions of particle formation on substrates, the role of substrate-deposit interaction across the interface for the particle shape, and the superparamagnetic properties of nanoparticles are briefly theoretically described. One property concerning the discretness of the energy levels depending on the particle size - the well known **quantum size effect** - is also treated. The equations containing the extinction function of nanoparticles in a dielectric matrix for attenuation of light are derived from the Mie theory. The optical absorption

spectra of nanoparticles from IB group are discussed. The particular case of core-shell structures is emphasized, taking into account the quantum size effect.

In Chapter 3 the experimental methods used to characterize the nanoparticle coatings are described. Transmission electron microscopy (TEM) is reviewed to assist understanding of image formation and contrast interpretation. A brief description of high resolution electron microscopy (HREM) is given because from that crystallographic information of the samples can be extracted and discussed. The other techniques pointed out are electron paramagnetic resonance (EPR), ferromagnetic resonance (FMR) and optical absorption spectroscopy. All these methods together shall give solid information on the formation and evolution of nanoparticles deposited via various routes on oxide materials.

Chapter 4 presents experimental results of the study aimed at finding appropriate oxide materials for metal deposition. In order to achieve sufficient coverage of the oxide substrate by metal particles, in a first approach a non-planar hydride-modified mesoporous oxide was used. The modification of the surface terminating groups shall improve the reduction of metal precursor compounds and promote particle formation. The second approach makes use of polydisperse oxide nanospheres. Because of their origin from pyrolysis techniques they contain a low number of OH-groups on the surface, but provide a smooth and uniform surface structure. The third approach concerns monodisperse silica nanospheres of commercial and laboratory-made origin. The Stöber method used for the preparation of these oxides is shortly described and some examples are given.

Chapter 5 presents experimental results of the exploration of transition metal particle coatings on hydride-modified non-planar oxide materials. Various types of metal nanoparticles of VIIIB and IB groups synthesized from two generic precursor types ($MX_n \cdot n$Lig, MX_n) were studied. Metal particle formation and coverage of the oxide substrates were controlled by changing deposition conditions like metal precursor concentration and temperature. For superparamagnetic particles (Fe, Co, Ni) the interaction with the magnetic field is discussed. Accordingly, the particle size is calculated and compared with TEM results. Quantum size effects of non-superparamagnetic group VIIIB metal particles were evidenced by conduction electron spin resonance (CESR) and compared to Kawabata theory calculations. Because of their strong plasmon resonance effects in the visible range the group IB metal (Cu, Ag, Au) particles are of special interest.

In Chapter 6 the results of studying metal particle coatings on oxide nanospheres are presented. First the deposition from organometallic Pt and Pd precursors of the type $[Li(THF)_2]_2 \cdot [MR]_4$ is tested on non-planar oxide surfaces and applied to polydisperse oxide nanospheres. These first attempts to achieve core-shell structures proved to be well suited as prenucleation step at which subsequent steps by complementary processes may follow. The result of such coating experiments on silica and titania nanospheres are presented with respect to the parameters involved.

The availability of monodisperse silica nanospheres improved decisively the exploration of appropriate coating conditions. Another route of nanoparticle coating was explored with Ag and Au where no organometallic precursors could be employed. Instead, incipient wetness impregnation was successfully applied as either a single-step or a multi-step procedure. Here the coating charac-

teristics depending on synthesis conditions are presented for Ag and Au core-shell-like structures and the corresponding optical properties are discussed.

Besides a summary of the research introduced in this thesis, the last chapter gives an outlook concerning the possible implementation of core-shell structures in various fields of optoelectronics and biotechnology. Emphasis is given also to potential improvements of the coating characteristic and adhesion strength of metal nanoparticles on oxide nanospheres to be considered in future studies.

Einleitung

Diese Arbeit ist dem Studium kleiner Metallpartikel (Nanopartikel) gewidmet, die auf die Oberfläche kleiner, nicht-zusammenhängender, sphärischer Oxidkörner (Nanokugeln) aufgebracht werden, um Kern-Hülle-Strukturen zu bilden. Diese Problematik wurde in den vergangenen Jahren ausgiebig untersucht, weil solche Strukturen besondere Eigenschaften aufweisen, die sie für Anwendungen in optischen und biologischen Sensoren und in der Optoelektronik interessant machen. Die Abschwächung von Licht in metallpartikel-enthaltenden Kompositmaterialien wird durch kollektive Oberflächenplasmonen-Moden hervorgerufen. Die optischen Eigenschaften hängen, neben Größe und Form der Metallpartikel, empfindlich von deren Umgebung, d.h. dem dielektrischen Medium, sowie auch ihrer Anordnung ab. Neuartige optische Effekte werden von geeigneten Kombinationen des Matrixmaterials mit speziellen Anordnungen der Partikel erwartet, wie z.B. Aggregatstrukturen oder Kern-Hülle-Strukturen. Für diese besonderen Geometrien sind Oxidnanokugeln von annähernd gleicher Grösse, die hohe Flexibilität der Gestaltung bieten, als Bausteine für künftige nanostrukturierte Materialien gut geeignet.

Anders als auf planaren Substraten erfordert eine einheitliche Bedeckung von Oxidnanokugeln Zugang des Deposits aus allen Richtungen. Abscheidung aus der Lösung, auf chemischem Wege, mit Bildung der Metallpartikel direkt auf der Oxidoberfläche ist genau das Richtige für diesen Zweck. Eine entsprechende Syntheseroute wird in mehreren Schritten angenähert unter Berücksichtigung von zwei Hauptbedingungen: es sollen unkontrollierte chemische Wechselwirkungen der Metallpartikel mit funktionalisierenden Agentien vermieden werden, die nachhaltig die Oberflächenplasmonresonanzen beeinflussen; und es soll eine Kontrolle der Zersetzungskinetik von Metallvorläuferkomplexen, und damit der Partikelgröße, bei moderaten Temperaturen ermöglich werden.

Diese Arbeit besteht aus sechs Kapiteln, in denen grundlegende und experimentellen Aspekte metallischer Nanopartikel präsentiert werden, die auf verschiedene Arten nichtplanarer Oxidsubstrate abgeschieden wurden. Die experimentellen Ergebnisse werden erläutert und durch theoretischen Berechnungen ergänzt, um die erhaltenen Daten mit Modellen zu vergleichen.

In Kapitel 2 werden die physikalischen Eigenschaften kleiner Metallpartikel unter strukturellen, morphologischen und elektronischen Aspekten sowie die Bedingungen der Partikelbildung auf Substraten, der Einfluss der Substrat-Deposit-Wechselwirkung durch die Grenzfläche auf die Par-

tikelform, und die superparamagnetischen Eigenschaften der Nanopartikel beschrieben. Die Diskretheit der Energieniveaus in Abhängigkeit von der Partikelgröße - bekannt als "Quantum-Size-Effekt" - wird behandelt und die Lichtabschwächung durch Nanopartikel in dielektrischer Matrix aus der Mie-Theorie unter Berücksichtigung von Kern-Hülle-Strukturen abgeleitet.

Kapitel 3 beschreibt die experimentellen Methoden, wie Transmissionselektronenmikroskopie (TEM), magnetische Resonanz und optische Absorptionsspektroskopie im sichtbaren Spektralbereich, die zur Charakterisierung der Nanopartikel-Beschichtungen herangezogen wurden.

Kapitel 4 präsentiert experimentelle Ergebnisse der Suche nach geeigneten Oxidmaterialien für die Metallabscheidung. In einer ersten Annäherung wurden nicht-planare, hydridmodifizierte mesoporöse Oxide verwendet. Ein weiterer Ansatz nutzt polydisperse Oxidnanokugeln und der dritte Weg betrifft kommerziell erhältliche bzw. labor-gefertigte, monodisperse SiO_2 Nanokugeln.

In Kapitel 5 werden experimentelle Ergebnisse zur Untersuchung der Bedeckung nichtplanarer Oxidmaterialien mit Partikeln der Übergangsmetalle gezeigt. Verschiedene Typen von Metallpartikeln der Gruppen VIIIB und IB, synthetisiert aus zwei allgemeinen Vorläufern ($MX_n \cdot nLig$ und MX_n) wurden untersucht. Metallpartikelbildung und Bedeckung der Oxidsubstrate wurden durch Änderung der Abscheidebedingungen wie Metallvorläufer-Konzentration und Temperatur geregelt.

In Kapitel 6 werden die Ergebnisse der Experimente zur Beschichtung von Oxidnanokugeln mit Metallpartikeln vorgestellt. Die Abscheidung aus organometallischen Pt- und Pd-Vorläuferkomplexen des Typs $[Li(THF)_2]_2 \cdot [MR]_4$ wurde auf polydisperse Oxidnanokugeln angewendet. Sie erwies sich als gut geeignet für einen Vorbekeimungsschritt, an den sich weitere Schritte mit komplementären Prozessen anschliessen können. Mit monodispersen SiO_2 Nanokugeln wurde dann für Ag und Au, weil keine organometallischen Vorläufer verfügbar waren, Nanopartikel-Beschichtung durch Inzipient-Wetness-Imprägnierung erfolgreich als Ein- und Mehrstufenprozedur angewendet.

Neben einer Zusammenfassung der in dieser Arbeit vorgestellten Ergebnisse gibt das letzte Kapitel einige Schlussfolgerungen über mögliche Anwendungen von Kern-Hülle-Strukturen in diversen Bereichen von Optoelektronik und Biotechnologie. Hervorgehoben werden auch Verbesserungen der Beschichtungsmerkmale und der Adhäsionsstärke von Metallnanopartikeln auf Oxidnanokugeln, die in späteren Untersuchungen berücksichtigt werden sollten.

2 Properties of small particles and particulate nanostructured materials

The application of nanostructured materials [Gle95] in technologies like optoelectronics, data storage or biotechnology implies the understanding of their physical and chemical properties and the response to different perturbations. Nanostructured materials can be found, e.g., in the form of ultrathin films or small particles deposited on substrates [Bäu99, Lue01]. It is already known that the physical and chemical properties of such systems are different from the bulk material, but also cannot be characterized by the physics of single atoms. At this scale (less than 100 nm) the optical [Kre97b], magnetical [Kaw70], electrochemical [And75] or thermodynamic [Bor81] properties are size-dependent. The control of the particle size and morphology and also the filling factor (the volume ratio of the metal particles to the total volume of the structure) enable a certain flexibility in creating new types of nanostructures.

An important category of nanostructured materials consists of metal particles on oxide substrates. Metal nanoparticles on planar oxide subtrates were intensively studied during the last century from an experimental [Pil01] and theoretical [Cam97] point of view. The confinement of the electron spatial distribution and the discreteness of the energy levels are properties which depend on the finite size of metal particles. The electron energy band structure depends on the lattice constant [Hal86]. Small metal particles mostly exhibit nearly spherical shape. Their curvature-induced surface stress (lattice contraction) implies modifications in the electronic properties. The quantum size effect induces splitting of the continuum conduction band into discrete levels, which may cause modifications of the magnetic properties like changes from diamagnetic to paramagnetic and from ferromagnetic to superparamagnetic behaviour [Dor97]. The enlargement of this splitting is also responsible for the shift observed in the peak of the surface plasmon resonance (optical absorption) [Kre97b, Hua97, Zho93].

The electrical properties of small metal particles in an insulator matrix depend, beside the structure of the matrix, on the filling factor. With an increase of this factor the particles agglomerate, form conducting chains and the sample becomes conductive.

The catalytic properties of small particles depend on the coordination number and the dispersion, i. e., the ratio between the number of surface atoms and the total number of atoms (see fig. 2.3).

This chapter presents general considerations on the structural, morphological and electronic properties of small metal particles which are dependent on the substrate surface or deposition

method. The special case of small metal particles deposited on non-planar substrates, in particular spherical surfaces, which is the subject of this work, will be described in more detail in the following chapters.

2.1   Structural and morphological properties of small particles

The study of the structure of metallic particles is primarily devoted to explain their physical and chemical properties. The shape of a deposit on a non-deformable substrate as a function of the substrate surface tension and the contact (wetting) angle is described thermodynamically by the Young equation [Hen98]. The contact angle is a measure of the interaction strength between the deposit and the substrate. The minimization of the free surface energy is given by the Wulff equation

$$\frac{\gamma_j}{h_j} = const. \tag{2.1}$$

where γ_i is the surface free energy of the corresponding face j and h_j is the central distance from the center of the crystal to the facet as represented in fig. 2.1(a). In general, the surface energy is different for different crystallographic planes ($\gamma_{(110)} > \gamma_{(100)} > \gamma_{(111)}$). In the case of a spherical nanoparticle the surface has to contain high index crystallographic planes which induce higher surface energy [Wan00]. If the particles are supported on a substrate (fig. 2.1(b)) the equilibrium shape is truncated by the height Δh_s at the interface depending on the *adhesion energy*. This is
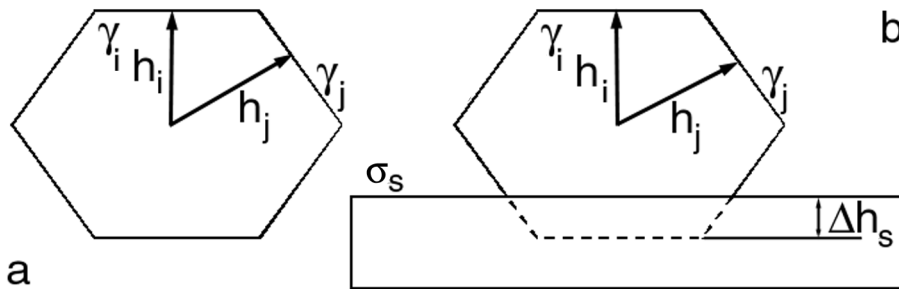
Fig. 2.1: *Wulff (a) and Wulff-Kaichew (b) constructions of the equilibrium shape.*

known as Wulff-Kaichew model and is described by

$$\frac{\Delta h_s}{h_j} = \frac{E_{adhesion}}{\gamma_j} \tag{2.2}$$

where $E_{adhesion} = \gamma_j + \gamma_{substrate} - \gamma_{interface}$, with $\gamma_{substrate}$ and $\gamma_{interface}$ being the free surface energy of the substrate and deposit/substrate interface energy, respectively.
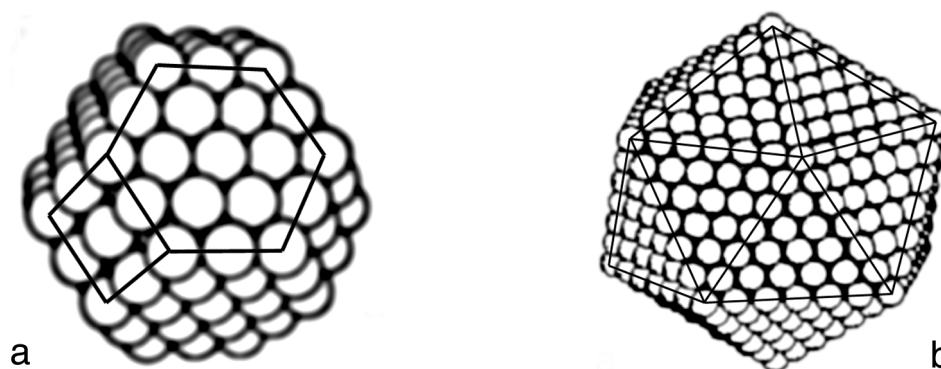
Fig. 2.2: *Atomic models of (a) cuboctahedral and (b) icosahedral nanoparticles.*

In order to obtain three-dimensional particles (Volmer-Weber growth) the sum of the free surface energy of the deposit and the interface energy must be greater than the surface energy of the substrate

$$\gamma_{interface} + \gamma_{metal} > \gamma_{oxide} \tag{2.3}$$

Whether the nuclei or aggregates are two-dimensional or three-dimensional depends on the number of deposit atoms and their interaction with the substrate. If the interaction strength of the deposit with the substrate is weaker than the interaction between deposit atoms, the result is formation of three-dimensional particles [Hen98]. Molecular dynamic calculations show that for very small sizes the structure of the particles depends on the number of atoms and is, in general, different from that of the bulk material. Comparison between particles with icosahedral or cuboctahedral shape (fig. 2.2) shows that the icosahedron is more stable in the case of small particles, depending also on the metal [Hen98]. Such *multiply twinned particles* occur preferentially for crystallites with face centered cubic (fcc) or diamond cubic (dc) lattice. These structures have been studied since more than forty years from a geometrical and physical point of view [Hof98].
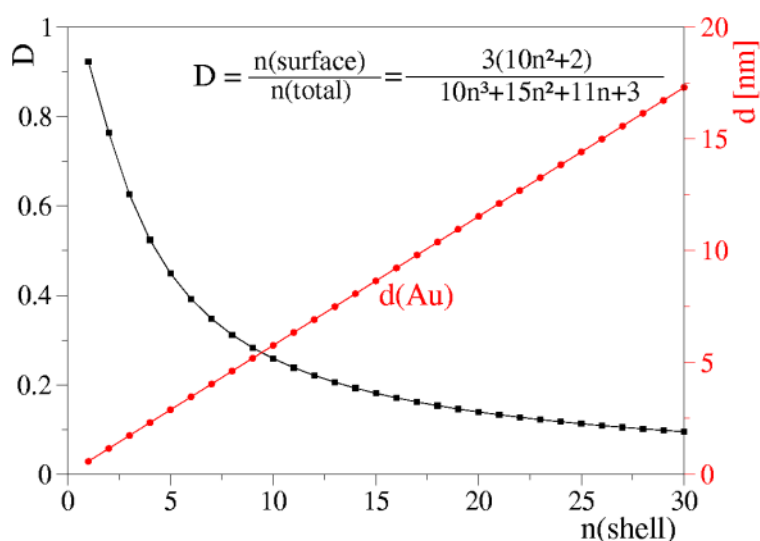
Fig. 2.3: *Calculated dispersion (black) and the size of the particles (red) as a function of the number of shells in the case of Au.*

$$D = \frac{n(\text{surface})}{n(\text{total})} = \frac{3(10n^2+2)}{10n^3+15n^2+11n+3}$$

Montejano-Carrizales [MC97] calculated the dispersion (D = ratio between the number of atoms on the surface and the total number of atoms of a particle) as a function of the number

of shells for different shapes. Fig. 2.3 shows as an example the calculation of the dispersion (black line) and the size of gold particle (red line) taking into consideration that the lattice spacing of the particle is not subjected to stress or strain.

2.2   Superparamagnetism of small metal particles

Néel [Née49] demonstrated in 1949 that decreasing the size of a ferromagnetic material (e.g. Fe, Co, Ni) leads for a critical size to a loss of ferromagnetism and it becomes superparamagnetic. The collective magnetization of metal particles which exhibit collective magnetic behaviour, can be characterized using **Ferromagnetic resonance** (FMR). Information on the nanoparticles and the interaction between particles and matrix or support can be obtained from FMR powder spectra and the temperature dependence of the spectra parameters. This technique is based on the influence of an external static magnetic field $\vec{H}_0$ applied along one direction of the coordinate system where the sample is placed. A polarized dc field applied perpendicular to the direction of the static magnetic field is used to detect the influences on the magnetic moment of the electrons which execute the Larmor precession with the angular frequency $\vec{\omega}_0 = \gamma \vec{H}_0$, $\gamma = -g\mu_B/\hbar$ being the gyromagnetic ratio, μ_B the Bohr magneton, g the spectroscopic splitting factor and $\hbar$ the reduced Planck constant. The application of these techniques and the main results will be shortly described below.

Interpretation and evolution of the absorption spectra are performed according to the "independent grain approach" of the "weak anisotropy" model discussed first by Schlömann [Sch58] and developed by Suran [Sur73] and Mörke [Mör96]. The free energy of a polycrystalline material for a constant temperature and magnetic field is a function of the magnetization vector $\vec{M}(x,y,z)$ according to the equation of motion [Mor80]

$$\frac{d\vec{M}}{dt} = -\gamma \vec{M} \times \vec{H}_{eff} = -\gamma E \tag{2.4}$$

where $\vec{H}_{eff}$ is the effective magnetic field which contains different types of contributions like: demagnetization, magnetocrystalline, magnetoelastic, etc. This model considers the free energy of a system in the presence of a magnetic field to be given by

$$E = E_Z + E_d + E_{me} + E_k \tag{2.5}$$

where E_Z is the Zeeman energy, E_d demagnetization energy (consist of the shape anisotropy and the strain field interaction with other particles), E_{me} magnetoelastic energy, and E_k magnetocrystalline anisotropy energy. The equation of motion (2.4) in polar coordinates (ϑ, φ) has a pair of solutions which vary harmonically if the resonance frequency ω satisfies

$$H_0 = \left(\frac{\omega}{\gamma}\right)^2 = \frac{1}{M^2 sin^2 \vartheta}(E_{\vartheta\vartheta}E_{\varphi\varphi} - E_{\vartheta\varphi}^2) \tag{2.6}$$

where E_{ii} are the second derivatives of the free energy function with respect to the polar coordinate system. The second derivatives of the free energy function are calculated for the equilibrium position where the first derivatives satisfy $E_{\vartheta} = E_{\varphi} = 0$. Equation (2.6) gives the resonance frequency as a function of the direction of the applied magnetic field which in general does not coincide with the direction of the magnetization vector. In a first approximation it is considered that the particles subjected to the magnetic field have also a magnetocrystalline anisotropy field H_a depending on the particle nature and a demagnetizing field H_d depending on the shape of the particles. Then the angular dependence of the resonance field $H(\theta, \phi)$ can be expressed for single spherical particles using the Sharma model [Sha81]

$$H(\theta, \phi) = H_0 - H_a\big(1 - 5U(\theta, \phi)\big) \tag{2.7}$$

with $H_a = 2|K|/M_s$, M_s the saturation magnetization of single particles, K the magnetic anisotropy and $U(\theta, \phi) = \sin^2 \theta \cos^2 \theta + \sin^4 \theta \sin^2 \phi \cos^2 \phi$. The resonance occurs at [Lue01]

$$H_{res} = K H_a^{sp} \tag{2.8}$$

where H_a^{sp} is the superparamagnetic anisotropic field defined as

$$H_a^{sp} = H_a \frac{1 - cos^{-1}L(x) + 35x^{-2} - 105x^{-3}L(x)}{L(x)} \tag{2.9}$$

$L(x) = \cosh x - 1/x$ being the Langevin function and $x = M_s vH/kT$, v the volume of the metal particle.

The second model used was developed by Suran et al. [Sur73] and it takes into consideration not only the crystalline anisotropy, but also the magnetoelastic anisotropy and demagnetization anisotropy as described by the equation (2.5). In this case the angular dependence of the resonance magnetic field $H(\theta, \phi)$ is given by

$$H(\theta, \phi) = H_0\big(1 - K_{\sigma 1} + (K_0 - 3K_{\sigma 2})[1 - 5S(\theta, \phi)]\big) \tag{2.10}$$

where $K_{\sigma 1} = 3\lambda_{S,T}\sigma/M_{S,T}H_0$ represents the isotropic part and $K_{\sigma 2} = 3(\lambda_{100} - \lambda_{111})\sigma/5M_{S,T}H_0$ is the anisotropic part of the magnetoelastic interaction, σ is the uniaxial strain ($\sigma > 0$) or stress ($\sigma < 0$), $K_0 = 2K_{1,T}/M_{S,T}H_0$ with $K_{1,T}$ the magnetocrystalline anisotropy constant. Here S is the function $S(\theta, \phi) = \alpha_1^2\alpha_2^2 + \alpha_2^2\alpha_3^2 + \alpha_1^2\alpha_3^2$ with α_i being the cosine direction of magnetization relative to the magnetic field. λ_{100} and λ_{111} are the anisotropic magnetostriction constants, $\lambda_{S,T}$ is the isotropic temperature depending on the magnetostriction constant. Comparison between the measured and the calculated spectra gives information on the size of the particles present in the sample and also on the different kinds of anisotropies.

2.3 Electronic properties of small particles

The theory of metallic bulk material gives a continuum spectrum of energy states as a limit of an infinitely large system. If the material has finite dimensions, for example particles with finite size, the states are not longer continuous and must be considered to be discrete with an average spacing between successive quantum levels denoted by δ [Kub84]. Since the number of states from the bottom of the valence band to the highest occupied level is equal to the half number of valence electrons, the average spacing is given by

$$\delta = 4E_F/3N \sim V^{-1} \tag{2.11}$$

where E_F is the Fermi energy and N is the total number of valence electrons in the system. Therefore, the discreteness of energy levels is expected to cause anomalies in some quantum statistical properties of metallic particles at low temperatures such as electron spin relaxation or optical absorption. Another important issue is the order of the electrical neutrality of the particles. The work W to charge a particle of a radius R by an elementary charge e is expected to satisfy the condition

$$W \simeq e^2/2R \gg k_B T \tag{2.12}$$

This energy is considerably larger than the thermal energy at room temperature. Therefore, the thermal fluctuation is never strong enough at low temperatures to allow any particle to loose or gain one more electron, even if the total amount of electrons within a particle is hundreds or thousands. The condition of neutrality is crucial in magnetic properties. In the case of small particles which have a reduced number of conduction electrons, specific heat and magnetic susceptibility are significantly altered at low temperature. In the free-electron theory the Fermi energy depends on the conduction electron density n_e and is independent of the particle size

$$E_F = \frac{\hbar^2}{2m}\left[3\pi^2 n_e\right]^{2/3} \tag{2.13}$$

The quantity δ is just the inverse of the average density of electronic states for a single spin at the Fermi energy. For nearly spherical particles with diameter d the level spacing varies with d^{-3} because of the proportionality between the density of electronic states and the volume, see equation (2.11).

The theory of the electronic properties of small particles was first presented by Kubo [Kub62, Kub84]. This theory uses the approximation that for low temperatures the energy spacing levels of a single particle is equal (i.e. all levels are equidistant). Using this model it is expected that at high temperatures no distinguishable differences between small particles and the bulk metal are observable. At sufficiently low temperature, however, the thermal energy $k_B T$ can be expected to be much lower than the work against the Coulomb interaction required to extract an electron from the particle.

As discussed also by Halperin [Hal86], the size dependent susceptibility of particles in strong magnetic fields at high temperature is given by

$$\chi_{even} = \chi_{odd} = \chi_{Pauli} = 2\mu_B/\delta \qquad\qquad \mu_B H >> \delta \qquad\qquad (2.14)$$

where μ_B is the Bohr magneton and H is the intensity of the magnetic field. At low temperature the magnetic susceptibility has a temperature dependence deviating from that of the bulk metal. In the case of particles with even number of electrons it was shown that the susceptibility is $\chi_{even} \simeq \mu_B^2/\delta$ depending also on the size distribution (which implies the distribution of level spacings). If the particles have an odd number of electrons then $\chi_{odd} = \mu_B^2/k_B T$ is independent of the particle size.

One of the experimental methods suitable to characterize this **quantum size effect** is the electron spin resonance due to the conduction electrons (**CESR**). The CESR signals of the small particles are observed at higher temperatures than for the bulk materials. Decreasing the particle size the level spacing increases and the line width decreases due to the longer relaxation time. As demonstrated by Kawabata [Kaw70] the electron relaxation time τ_s depends on the *resistivity* relaxation time $\tau_r = 2R/v_F$, where v_F is the Fermi velocity, and on the bulk g-shift $\Delta g_\infty = g_{bulk} - g_{free\ electron}$. This dependence can be expressed as

$$\frac{1}{\tau_s} = \frac{1}{\tau_r}(\Delta g_\infty)^2 \qquad\qquad (2.15)$$

In the case of very small particles, when the number of atoms on the surface of the particle and the total number of atoms are comparable, a shift of the resonance position (g-factor) [Kaw70] is observed which makes interpretation of the CESR spectra difficult. The particles show quantum size effect if the following conditions are fulfilled

$$\delta >> \hbar\omega \qquad\qquad (2.16)$$

$$\delta >> \frac{\hbar}{\tau_s} \qquad\qquad (2.17)$$

where $\hbar = h/2\pi$ is the reduced Planck constant and $\hbar\omega$ the Zeeman energy. Not only the g-factor is subjected to the quantum size effect but also the CESR peak-to-peak line width (ΔH_{pp}). The peak-to-peak line width of the bulk metal can be expressed in terms of the spin relaxation time as

$$\Delta H_{pp} \simeq (\gamma_e \tau_s)^{-1} \qquad\qquad (2.18)$$

where γ_e represents the electron gyromagnetic ratio. Taking into account the definition of the electron relaxation time (2.15), the Kawabata conditions (2.16) (2.17) and the line width, the size of the nanoparticles can be estimated using

$$d = a\sqrt{\Delta H_{pp}} = \sqrt{\frac{h\nu}{\gamma_e \delta \tau_s}}\sqrt{\Delta H_{pp}} \qquad\qquad (2.19)$$

where ΔH_{pp} is given in mT, d in nm, and a being a constant. Fig. 2.4 represents the calculated average electron level spacing for different metals using the measurements of the heat capacity [Hal86]. From this graph the size of the particles can be extracted for $\delta/k_B = 1$ or 300 K (marked
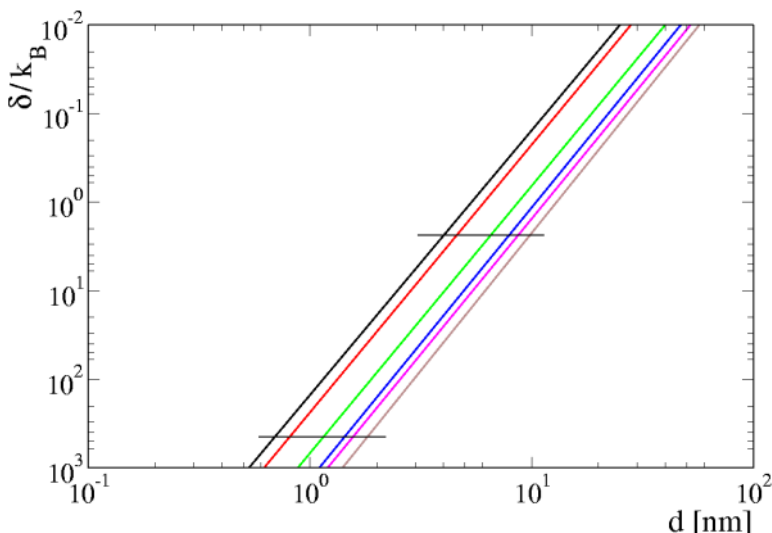
Fig. 2.4: Calculated average electron-level spacing as a function of particle size for different metals: Pd (black), Pt (red), Os (green), Cu (blue), Au (magenta), Ag (brown), [Hal86].

with bars) and taking into account the values of the Fermi velocity of the bulk material. Also the mean free path [Ash76] can be estimated from the proportionality constant between the peak-to-peak linewidth of the CESR signal and the particle size. A theoretical estimation of the above discussed parameters for room temperature taking into account the Fermi velocity from [Ash76] is summarized in Table 2.1. For materials were Δg_∞ is not listed in this table the value corresponding to Pd is considered. These calculated values give us the possibility to identify the CESR signal of each sample.

Table 2.1: Peak-to-peak linewidth of CESR signals and Kawabata conditions (2.16) and (2.17) calculated using the results of Halperin [Hal86]

Metal	v_F 10^6 [m/s]	Δg_∞	Kawabata I [nm]	Kawabata II [nm]	a
Pd	0.35	0.24	29	8.5	0.46
Pt	0.44	-	27	6.7	0.37
Rh	0.59	-	24	5	0.28
Ru	0.63	-	24	4.7	0.26
Ir	0.79	-	22	3.7	0.2
Cu	1.57	0.0032	17	14.5	0.8
Ag	1.45	-0.0019	18	25	1.4
Au	1.32	0.1	19	5.3	0.29

Another aim of the electron magnetic resonance measurements is to record also the paramagnetic species occurring in the process of particle formation on the oxide surface. For this task the **Electron Paramagnetic Resonance** (EPR) technique is applied. Such species may originate from possible modifications of the oxide surface or from the presence of residual metal ions on the surface.

The EPR spectra are very complex because of various paramagnetic species present. Our samples contain small metal particles which are randomly oriented on a nonplanar oxide surface. The EPR spectrum characteristic of such a system is the envelope over all elementary resonance lines corresponding to all possible orientations of the particles with respect to the applied magnetic field [Dyr97]. In order to characterize the interactions of the spins with each other and of the spins with the applied field, the spin Hamiltonian term has to be considered because it contains all possible interactions

$$\mathscr{H}_s = g\mu_B \vec{H} \cdot \vec{S} - 2\boldsymbol{J}\vec{S} \cdot \vec{S} + A\vec{I} \cdot \vec{S} \tag{2.20}$$

In general, for paramagnetic materials the g-factor and the hyperfine coupling constant (denoted A in equation (2.20)) are tensors. The g tensor is characterized by the principal values g_{xx}, g_{yy}, g_{zz} along the x, y, z coordinate axes. Considering that the magnetic field can be described with respect to the same axis using the angles θ and ϕ, it is possible to describe the magnetic field along the g-factor directions. In a first approximation only the contribution of the g-tensor is taken into account, which can be isotropic, axial or orthorhombic. The isotropic lines with $g_{xx} = g_{yy} = g_{zz} = g_{iso}$ are observed in general for samples with solid-state defects [Dyr97]. Such a signal, for example, is observed in SiO_2 as a result of the formation of ($\equiv$ Si•) known as E' centers [Gri84]. For axial symmetry the g tensor is characterized by two values $g_\parallel = g_{zz}$, and $g_\perp = (g_{xx} + g_{yy})/2$. Here, an example are the non-bridging oxygen hole centers ($\equiv$ Si-O•)(NBOHC or HC centers) [Gri84].

For orthorhombical symmetry the g tensor is characterized by all three values $g_1 = g_{xx}$, $g_2 = g_{yy}$, $g_3 = g_{zz}$. The orthorhombical symmetry can be better observed using a Q-band spectrometer (working at $\simeq 35$ GHz) were the signals are more narrow. In this work, all magnetic resonance measurements of the g values are determined from the magnetic field position at the center of the absorption line, and the hyperfine tensor values from the average spacing between the peak positions. The average value of the g-factor is given by

$$g_{av} = \frac{1}{3}\left(g_{xx} + g_{yy} + g_{zz}\right) \tag{2.21}$$

2.4   Optical properties of small particles

Small metal particles exhibit in the visible range optical properties different from those of the bulk material due to their size and shape. The interest in this field increased in recent years because of the importance of producing new materials with novel optical and electronic properties. At the beginning of the last century the study of color changes of various types of glasses [Mie08, Boh98] triggered this research area. Moreover, another area of interest was to find new materials with a dielectric function different from that of the bulk material that first were applied to improve photovoltaic conversion [MG04, Bru35]. In order to study the properties of nanoparticles on oxide surfaces from the optical point of view in this work the Mie theory and also the Maxwell-Garnet theory are applied for the case of small filling factor, and the Bruggeman model for higher values.

Mie [Mie08] explained the optical properties of spherical metal particles in a nonabsorbing matrix. He treated the dielectric function of the particles $\varepsilon(\omega)$ as a free parameter. This theory solves the Maxwell equation in spherical coordinates (r, θ, ϕ) with the boundary condition

$$E_\theta^{out} = E_\theta^{in}, \quad E_\varphi^{out} = E_\varphi^{in}, \quad \varepsilon^{out} E_r^{out} = \varepsilon^{ins} E_r^{ins} \qquad \text{at } r = R$$

where R is the radius of the particle. The solutions are given as infinite series of Bessel and Neumann functions and Legendre polynomials of different polar order. To obtain the incident, scattered and absorption intensities the Poynting law has to be applied. On one side the electric modes contain collective excitations of the conduction electrons. On the other side the magnetic modes are important for the exciting series expansion of the eddy currents but are not important via magnetic interactions. It is found that the spectral position $\hbar\omega$ and the resonance band widths Γ strongly vary with the cluster material. In the approximation of very small silver clusters the peak position $\hbar\omega$ and the halfwidth Γ can be analytically derived from the Mie theory

$$\omega_{res} \simeq \left(\frac{n_e e^2}{\varepsilon_0 m_{eff}} \right)^{1/2} + \left(2\varepsilon_{matrix} + 1 + \chi_{1,interband} \right)^{-1/2} \tag{2.22}$$

where n_e is the conduction electron density, m_{eff} the effective mass, ε_m the dielectric constant of the host matrix, $\chi_{1,interband}$ the interband transition excitation. The first term describes the Drude plasma frequency ω_p. However, for many metals, e.g. Pt, the resonance is fully suppressed due to the very strong energy dissipation which is not included in ω_p in equation (2.22) [Kre95]. If the particle radius R is smaller than the mean free path of the bulk material the conduction electrons are additionally scattered by the surface and the effective mean free path becomes size dependent

$$\frac{1}{l_{eff}} = \frac{1}{R} + \frac{1}{l_\infty} \tag{2.23}$$

and the resonance width is additionally broadened

$$\Gamma(R) = \Gamma(0) + \frac{Av_F}{R} \tag{2.24}$$

where $\Gamma(0)$ is the width of the resonance spectra of the bulk material, v_F the Fermi velocity, l_∞ the mean free path of the bulk material and A/R a term derived from the reduction of conduction electron mean free path due to collisions with the particle surface. This size dependence is observable in the modification of the dielectric function of the metal which according to Otter [Ott61] becomes

$$\varepsilon(\omega, R) = \varepsilon_{bulk}(\omega) + \omega_p^2 \left(\frac{1}{\omega^2 + \Gamma(0)^2} + \frac{1}{\omega^2 + \Gamma(R)^2} \right) + i \frac{\omega_p^2}{\omega} \left(\frac{\Gamma(R)}{\omega^2 + \Gamma(R)^2} - \frac{\Gamma(0)}{\omega^2 + \Gamma(0)^2} \right) \tag{2.25}$$

where the second term is the modified plasmon frequency and the third term the absorption due to free electrons.

Considering in the first approximation that the distance between particles is large enough to neglect any interaction between particles, and that the system contains particles of equal size, the Mie theory gives solutions for the extinction, scattering and absorption cross sections

$$\sigma_{ext} = \frac{2\pi}{|k|^2} \sum_{L=1}^{\infty} (2L+1)\Re(a_L + b_L) \tag{2.26}$$

$$\sigma_{sca} = \frac{2\pi}{|k|^2} \sum_{L=1}^{\infty} (2L+1)(|a_L|^2 + |b_L|^2) \tag{2.27}$$

$$\sigma_{abs} = \sigma_{ext} + \sigma_{sca} \tag{2.28}$$

where $k = 2\pi\varepsilon_m/\lambda$, and a_L, and b_L the scattering coefficients being derived from the boundary conditions in terms of Bessel-Ricatti functions, $\Re$ mean the real part.

2.4.1 Nanoparticles in a dielectric matrix

For particles embedded in a dielectric matrix Mie coefficients are given by [Boh98]

$$a_L = \frac{m\psi_L(mx)\psi_L'(x) - \psi_L(x)\psi_L'(mx)}{m\psi_L(mx)\xi_L'(x) - \xi_L(x)\psi_L'(mx)} \tag{2.29}$$

$$b_L = \frac{\psi_L(mx)\psi_L'(x) - m\psi_L(x)\psi_L'(mx)}{\psi_L(mx)\xi_L'(x) - m\xi_L(x)\psi_L'(mx)} \tag{2.30}$$

m is the complex relative refractive index $m = N/n_m$, $N = n + ik$ the complex refractive index of the metal particles, n_m the real refractive index of the matrix, $\psi_L(z), \xi_L(z)$ the Bessel-Ricatti functions with complex argument and $x = 2\pi NR/\lambda$ the size parameter. The prime means the derivative of the function with respect to the argument and L is the multipolar order (L=1, dipolar, L=2 quadrupolar, etc). From the extinction cross section and knowledge of the filling factor f and the volume of one particle v_0, it is straightforward to calculate the extinction coefficient of the sample $\alpha_{ext} = f\sigma_{ext}/v_0$. Spherical metal particles with sizes less than 10 nm have a dielectric function $\varepsilon = \varepsilon' + i\varepsilon''$ in the dipolar approximation and the extinction coefficient can be written as

$$\alpha_{ext} = 18\pi \frac{f v_0 \varepsilon_m^{3/2}}{\lambda} \frac{\varepsilon''}{\left[(\varepsilon' + \varepsilon_m)^2 + \varepsilon''^2\right]} \tag{2.31}$$

where the real and imaginary part of the dielectric function are described using the simple Drude model and ε_m is the real part of the host matrix dielectric function.

Fig.2.5 shows the extinction spectra of copper (black), gold (red) and silver (green) metal particles with a mean size $d = 5$ nm in a SiO_2 matrix with $n = 1.54$ calculated according to the above formalism by approximation of spherical particles with multipolar interaction. The theoretical calculation shows that with increasing size of the particles a red shift can be observed. For very small sizes (less then 10 nm) a small blue shift was also reported [Pal98].
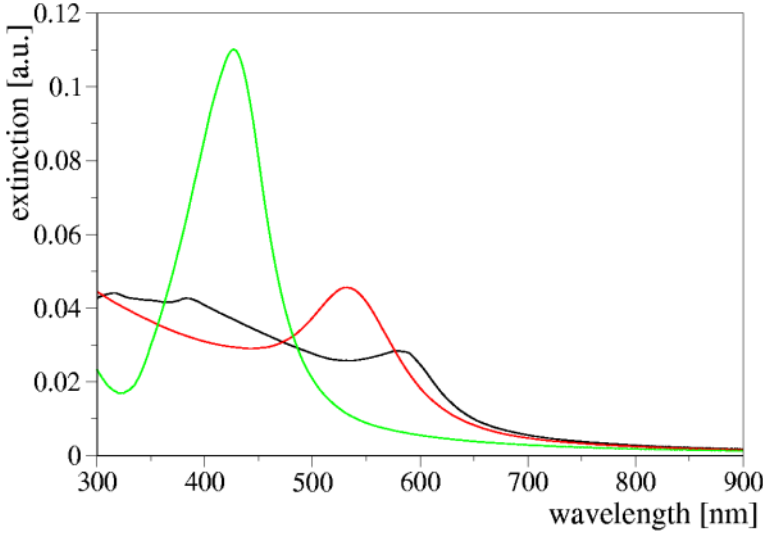
Fig. 2.5: *Calculated extinction spectra of copper (black), gold (red) and silver (green) particles with d=5 nm in SiO$_2$ matrix with n=1.54.*

However, a real sample has a distribution of particle sizes where the application of the Mie theory is not straightforward. In this work the extinction spectra are calculated from the size distribution histogram for each d_i and the resulting spectra are obtained by superposition of the calculated spectra taking into account the adequate filling factor for each size.

For very small particles ($d \leq 2$ nm) a damping and broadening of the resonance appears because of the reduced density of conduction electrons. The electrons reach the surface very fast and loose the coherence more quickly due to scattering than in large particles. As a consequence, the plasmon band width increases with decreasing particle size. The model described above is valid only for spherical particle shape. In general, this approximation is correct for very small particles, but with increasing size deviation from the spherical shape can occur. Also for this kind of particles there is a well developed theory. A comprehensive text about the calculation of extinction and scattering coefficient of spheroidal particles was presented by Porstendorfer [Por97]. In our calculations we apply the extension of Mie theory according to Gans [Gan15] in a dipolar approximation where the extinction cross section of a prolate ellipsoid is given by

$$\sigma_{ext} = \frac{v_0 \varepsilon_m^{3/2}}{3\lambda} \frac{\varepsilon''/P_j^2}{\left\{\varepsilon' + \left[(1-P_j)/P_j\right]\varepsilon_m\right\}^2 + \varepsilon''^2} \tag{2.32}$$

where P_j are the depolarisation factors along the axis a, b, c of the ellipsoid defined for $a > b = c$ by

$$P_a = \frac{1-e^2}{e^2}\left[\frac{1}{2e}\ln\left(\frac{1+e}{1-e}\right) - 1\right] \quad \text{and} \quad P_b = P_c = \frac{1-P_a}{2} \tag{2.33}$$

where

$$e = \left[1 - \left(\frac{c}{a}\right)^2\right]^{1/2}$$

is the eccentricity of the spheroid.

The Mie theory is valid for separated particles only when the distance between particles is much larger than the particle size and no aggregate structures occur. For higher particle concentration and agglomerate formation it is necessary to apply a different model in order to characterize the optical properties. In a first approximation which is also valid for small filling factors the Maxwell-Garnett effective medium theory [MG04] can be applied. With the obtained effective dielectric functions the absorption coefficient can be calculated using the optical definitions used for thin films. Another possibility is to use this dielectric function in Mie calculations. If the sample has a high filling factor, which means that part of the particles are aggregated, and if the distance between particles is smaller than their diameter, it is more adequate to apply the effective medium approximation method proposed by Bruggeman [Bru35] which yields for an effective dielectric function the second order equation

$$(1-f)\frac{\varepsilon_m - \varepsilon_B}{\varepsilon_m + 2\varepsilon_B} + f\frac{\varepsilon - \varepsilon_B}{\varepsilon + 2\varepsilon_B} = 0 \tag{2.34}$$

For small filling factors this approximation gives the same results as the Maxwell-Garnett theory, but for large values of f the results are different [Gra77].
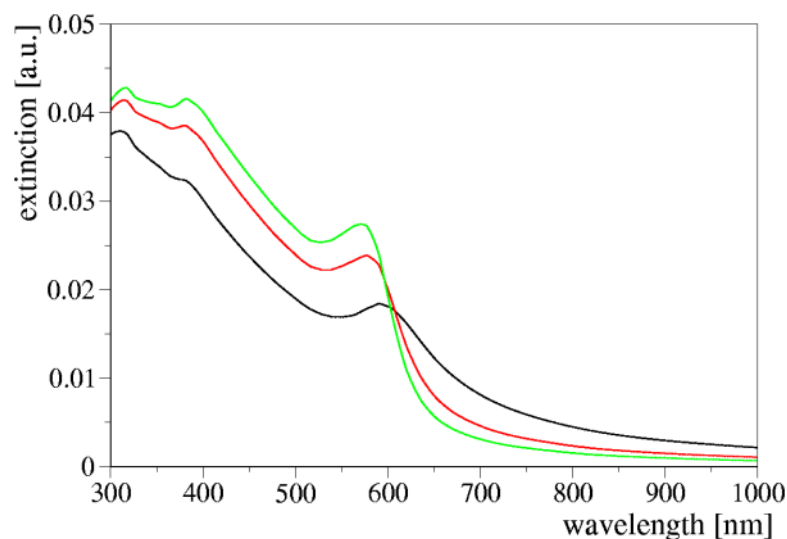
Fig. 2.6: *Optical extinction spectra calculated for Cu nanoparticles of various sizes: 2 nm (black), 5nm (red), and 10nm (green), in silica matrix.*

To get an indication how the optical properties of Cu nanoparticles change in the size range of the prepared sample the extinction spectra were calculated for various sizes by means of the Mie theory assuming particles of spherical shape without formation of aggregates. The calculations do not consider any dielectric matrix or support of the particles, but the intrinsic size effect is taken into account. The extinction spectra shown in fig. 2.6 exhibit a certain blue shift of the resonance position with increasing particle size as it was generally observed by other groups [Yok89, deC95, Kre95].

Ag nanoparticles exhibit surface plasmon resonances which are mostly sharp and well separated from interband transitions. The unique optical properties of free and matrix-embedded Ag particles were studied intensively over decades and also recently [Kre70, Kre74, Kre97b]. The evolution of the optical extinction of spherical Ag particles embedded in SiO_2 is represented by

calculated spectra in fig. 2.7. According to the second Kawabata condition (2.17) below 20 nm particle diameter the quantum size effect is taken into account. For larger particles multipolar interaction is considered which may result, e.g., for 50 nm particles, in quadrupol interactions as can be seen from the occurrence of a second peak in the spectrum.
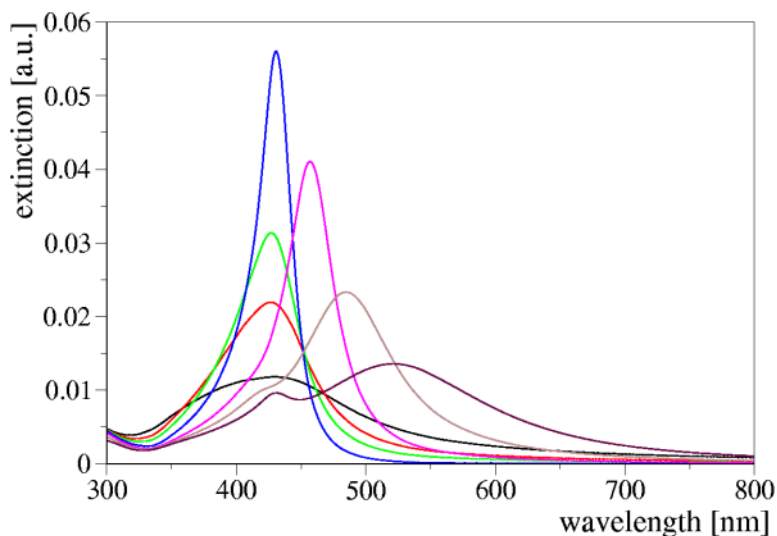
Fig. 2.7: *Optical extinction spectra calculated for Ag nanoparticles of various sizes: 2 nm (black), 5 nm (red), 10 nm (green), 20 nm (blue), 50 nm (magenta), 70 nm (brown), and 90 nm (maroon), in silica matrix.*

Similar to Ag, Au nanoparticles exhibit sharp surface plasmon resonances around 550 to 650 nm, well separated from interband transitions. Application of the optical properties by embedding Au nanoparticles in various matrices are known and studied as intensively as those of Ag particles. The issue of a certain distribution of particle sizes, e.g., and the presence of non-spherical particles have been treated by Granqvist [Gra77] using the effective medium theory. The same method was applied by Norman [Nor78] to study the optical behaviour of discontinuous films of such metals. How the optical properties of Au nanoparticles of spherical shape, embedded in a SiO_2 matrix of refraction index n = 1.54, change with particle size, may be recognized from the extinction spectra shown in fig. 2.8, calculated by means of the Mie theory. The calculations consider the size effect according to the Kawabata theory. For large particles also multipolar approximations as described by Bohren [Boh98] and Wiscombe [Wis79] have to be considered.
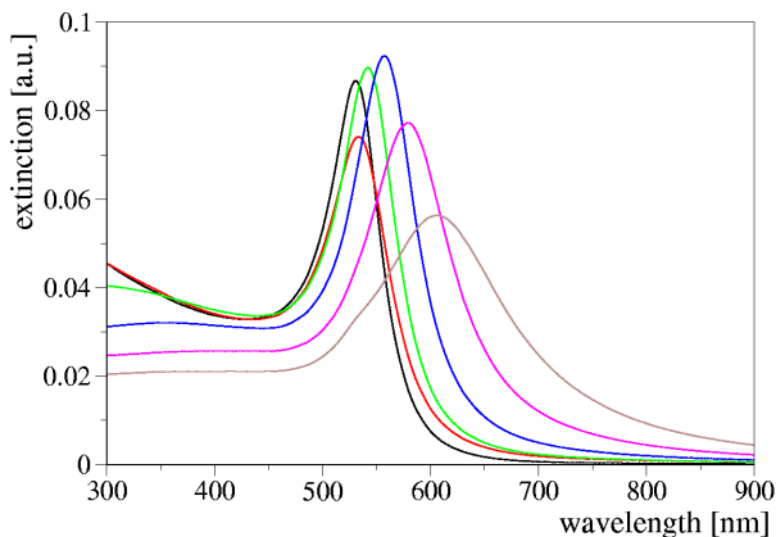
Fig. 2.8: *Optical extinction spectra calculated for gold nanoparticles of various size:* 2 nm *(black);* 20 nm *(red);* 40 nm *(green);* 60 nm *(blue);* 80 nm *(magenta);* 100 nm *(brown), in silica matrix.*

2.4.2 Core-shell structures

Particles, having a dielectric function ε_{core}, covered by multi-shell layers were studied first by Aden and Kerker, Güttler and Bhandari [Ade51, Güt52, Bha85]. They extended the Mie theory for a core particle covered by an arbitrary number of shells. Kreibig [Kre95] gives the recurrence solution for the case of k-shells (with $k = 1, 2, 3 ...$). The Mie coefficients can be determined using the relations

$$a_n = -\frac{m_k \psi_n(m_k y_k) \left[\psi_n{'}(y_k) + T_n^{k-1} \chi_n{'}(y_k)\right] - \psi_n{'}(m_k y_k) \left[\psi_n(y_k) + T_n^{k-1} \chi_n(y_k)\right]}{m_k \xi_n(m_k y_k) \left[\psi_n{'}(y_k) + T_n^{k-1} \chi_n{'}(y_k)\right] - \xi_n{'}(m_k y_k) \left[\psi_n(y_k) + T_n^{k-1} \chi_n(y_k)\right]} \quad (2.35)$$

$$b_n = -\frac{\psi_n(m_k y_k) \left[\psi_n{'}(y_k) + S_n^{k-1} \chi_n{'}(y_k)\right] - m_k \psi_n{'}(m_k y_k) \left[\psi_n(y_k) + S_n^{k-1} \chi_n(y_k)\right]}{\xi_n(m_k y_k) \left[\psi_n{'}(y_k) + S_n^{k-1} \chi_n{'}(y_k)\right] - m_k \xi_n{'}(m_k y_k) \left[\psi_n(y_k) + S_n^{k-1} \chi_n(y_k)\right]} \quad (2.36)$$

with

$$T_n^l = -\frac{m_l \psi_n(m_l y_l) \left[\psi_n{'}(y_l) + T_n^{l-1} \chi_n{'}(y_l)\right] - \psi_n{'}(m_l y_l) \left[\psi_n(y_l) + T_n^{l-1} \chi_n(y_l)\right]}{m_l \chi_n(m_l y_l) \left[\psi_n{'}(y_l) + T_n^{l-1} \chi_n{'}(y_l)\right] - \chi_n{'}(m_l y_l) \left[\psi_n(y_l) + T_n^{l-1} \chi_n(y_l)\right]} \quad (2.37)$$

$$S_n^l = -\frac{\psi_n(m_l y_l) \left[\psi_n{'}(y_l) + S_n^{l-1} \chi_n{'}(y_l)\right] - m_l \psi_n{'}(m_l y_l) \left[\psi_n(y_l) + S_n^{l-1} \chi_n(y_l)\right]}{\chi_n(m_l y_l) \left[\psi_n{'}(y_l) + S_n^{l-1} \chi_n{'}(y_l)\right] - m_l \chi_n{'}(m_l y_l) \left[\psi_n(y_l) + S_n^{l-1} \chi_n(y_l)\right]} \quad (2.38)$$

where $\psi_z = z j_n(z)$, $\chi_n(z) = z y_n(z)$ and $\xi_n(z) = h_n^{(1)}(z)$ are the Ricatti-Bessel functions, n is the order of the Bessel functions, and prime denotes the first derivative of the function in respect to its argument. $l = 1, 2, ...k$ are the number of shells and $m_l = n_{l+1}/n_l$ represents the relative complex refractive index from the shell $(l+1)^{th}$ to the lth one. For $l = k$ the refractive index $n_{k+1} = n_m$
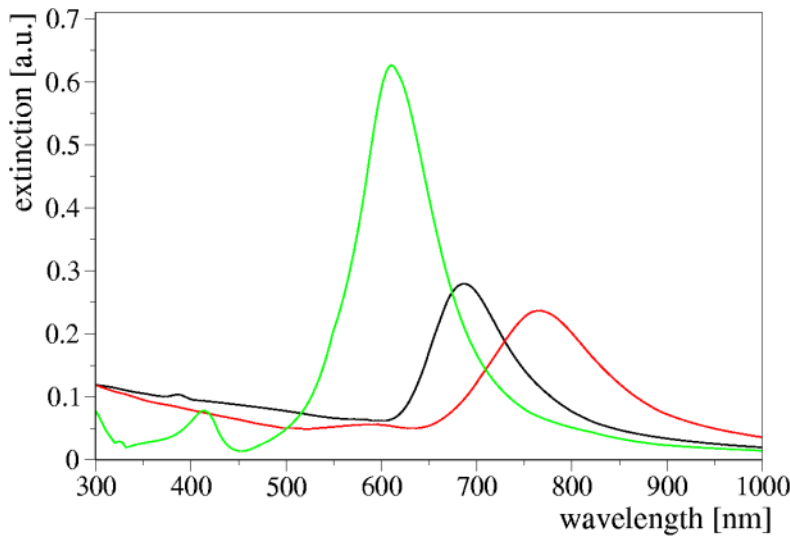
Fig. 2.9: Calculated extinction spectra of copper (black), gold (red) and silver (green) shells with d=10 nm on SiO$_2$ core of 25 nm radius with n=1.5.

corresponds to the refractive index of the matrix and $y_l = 2\pi n_l R_l/\lambda$ is the size parameter of the lth shell. For recurrence starting with the values $T_n^0 = S_n^0 = 0$, from the obtained Mie coefficients the extinction cross section can be calculated with the equation (2.26).

In the dipolar approximation using (2.35) and (2.36) for the case of a core with one shell, the absorption cross section can be calculated as [Fed93]

$$\sigma_{abs} = 18\pi \frac{V \varepsilon_m^{1/2}}{\lambda} \Im \left\{ \frac{(\varepsilon - \varepsilon_m)(\varepsilon_c + 2\varepsilon) + g(\varepsilon_c - \varepsilon)(\varepsilon_m + 2\varepsilon)}{(\varepsilon + 2\varepsilon_m)(\varepsilon_c + 2\varepsilon) - g(\varepsilon_c - \varepsilon)(2\varepsilon_m - 2\varepsilon)} \right\} \qquad (2.39)$$

where $\Im$ is the imaginary part, ε is the complex dielectric function of the shell, ε_m is the real dielectric function of the host medium, ε_c is the real dielectric function of the core material, V is the volume of the coated sphere and $g = \left(\frac{R}{R+d}\right)^3$, with R the radius of the core particle, and d the thickness of the shell. Fig. 2.9 shows the extinction spectra of copper (black), gold (red) and silver
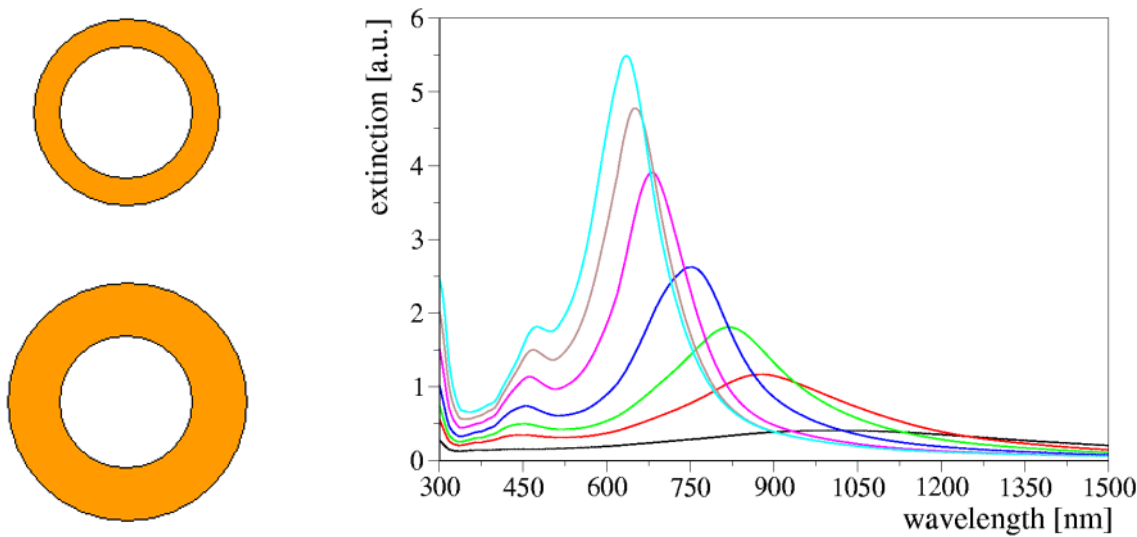
Fig. 2.10: *Calculated extinction spectra of Ag on silica (60 nm) core-shell structures of varying shell thickness: 2 nm (black), 5 nm (red), 7 nm (green), 10 nm (blue), 15 nm (magenta), 20 nm (brown), 25 nm (cyan).*

(green) shells with thickness of $d = 10$ nm on a SiO$_2$ core with $n = 1.5$ and radius of $R = 25$ nm calculated according to the above formalism by approximating spherical particles in terms of the dipolar interaction. With increasing the thickness of the shell, theoretical calculations predict a blue shift of the plasmon resonance and an increasing signal intensity. Oldenburg [Old98] studied the case of Au-SiO$_2$ core-shell structures with 120 nm silica core and he found a blue-shift of the plasmon resonance of about 200 - 300 nm if the shell thickness increases from 5 to 20 nm. Fig. 2.10 presents as an example calculations for Ag shell coatings on 60 nm SiO$_2$ core where the thickness ranges from 2 (black) to 25 (cyan) nm. This graph shows that the blue-shift amounts to about 450 nm, i. e., more than in the case of Au nanoshells. The core-shell structures can be designed in such a way that they cover a spectral range up to the infrared. Using the same parameters, the calculations for Au show a blue-shift of about 400 nm and of 500 nm for Cu.

An important influence on the optical properties comes also from the core size. Fig. 2.11 shows an example of the red-shift incuced by increasing the size of the core particles in the range of 20 to 100 nm covered with a Au shell of about 5 nm. It can be observed that for this configuration the extinction spectra are shifted to the boundary between visible and infrared ranges. This red-shift
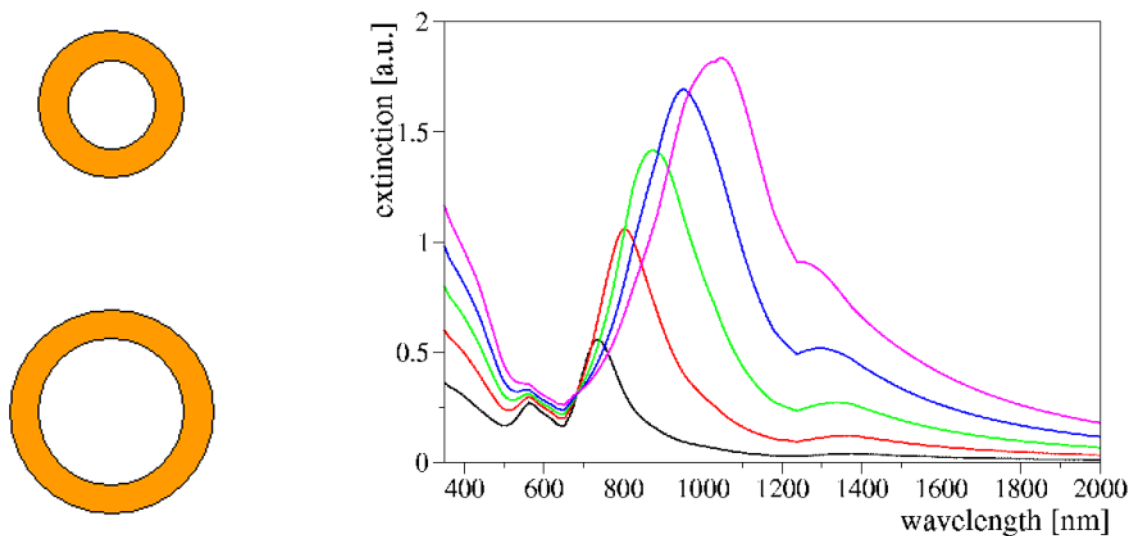
Fig. 2.11: *Calculated extinction spectra of Au (5 nm) on silica core-shell structures of varying core size: 20 nm (black), 40 nm (red), 60 nm (green), 80 nm (brown), 100 nm (magenta).*

calculated for a shell thickness of 5 nm was found to be about 320 nm in the case of Au, 450 nm for Ag and 350 for Cu.
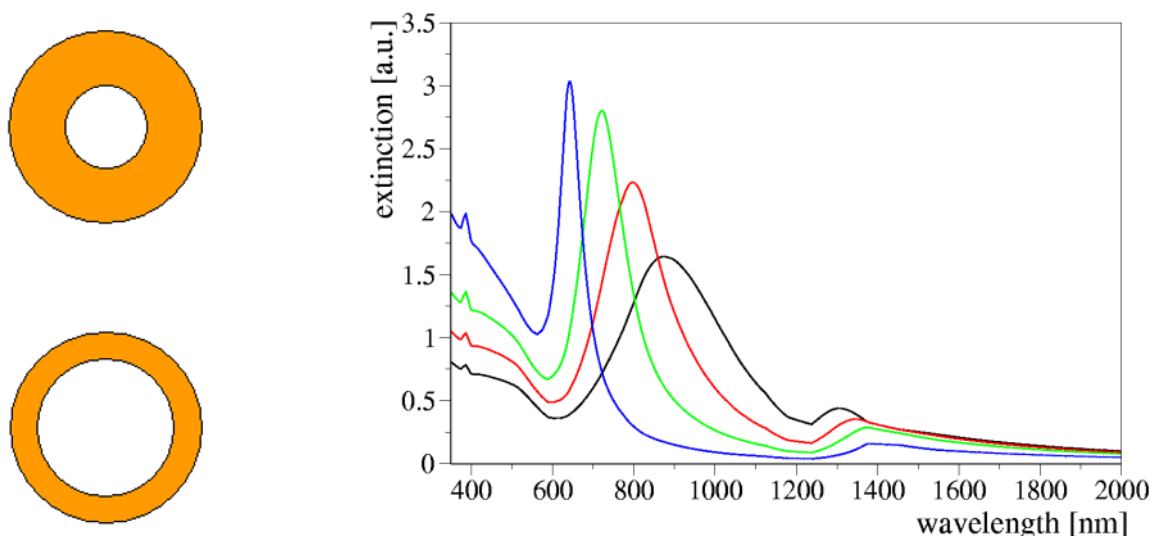
Fig. 2.12: *Calculated extinction spectra of Cu on silica core-shell structures of varying core:shell ratio: 35:5 nm (black), 33:7 nm (red), 30:10 nm (green), 20:20 nm (blue).*

In the same way core-shell structures can be designed with different surface plasmon resonances keeping the external radius constant. Fig. 2.12 shows an example of 40 nm nanoshells formed using different core-shell ratios. Also in this case a blue-shift can be observed which means that the shell thickness is decisive for the position of the plasmon resonance. The calculations predict a blue-shift of about 320 nm in the case of Ag, 220 nm for Au and 250 in case of Cu.

Taking these theoretical calculations into account it is possible to design core-shell structures for various applications in optical devices and sensors.

3 Characterization methods for small particles

From the great number of analyzing techniques that may be applied for characterizing physical properties of nanostructured materials here only those are introduced which were extensively used in the present work. These are electron microscopy, electron magnetic resonance and optical spectroscopy. By **electron microscopy** at its highest level structural characteristics of specimens under investigation may be retrieved down to the atomic scale of resolution. While electron microscopy is used for directly imaging a certain specimen area, the other methods use the response of a sample upon perturbations by a magnetic field or by visible light. The general name electron magnetic resonance is used for **electron paramagnetic resonance** (EPR) applied to the study of paramagnetic species like ions from a physical and chemical point of view, and for **ferromagnetic resonance** (FMR) applied to the study of the magnetic properties of superparamagnetic nanoparticles. The optical absorption and elastic scattering of light by particulate matter is extensively studied and corresponding **optical spectroscopy** measurements allow to draw conclusions on a number of structural features. Therefore, the optical properties of the materials prepared sensitively reflect how close a certain approach meets the intended structures.

3.1 Transmission electron microscopy

Electron microscopy is a powerful method to investigate nanoparticle composite materials from the morphological and structural point of view. Morphological properties of the samples are studied using transmission electron microscopy (TEM) and the structural characterization of nanoparticles is performed with high resolution electron microscopy (HREM). Because in the following only a short description can be given, for complete understanding of the electron microscopy technique numerous textbooks are available [Bet87, Wil96].

3.1.1 Image formation

Fig. 3.1 shows a schematic drawing of the main components of a transmission electron microscope. They cooperate in the following functional units: *(i)* illumination system composed of electron source and condenser lenses, *(ii)* specimen stage for shift, titling and rotation, *(iii)* image formation
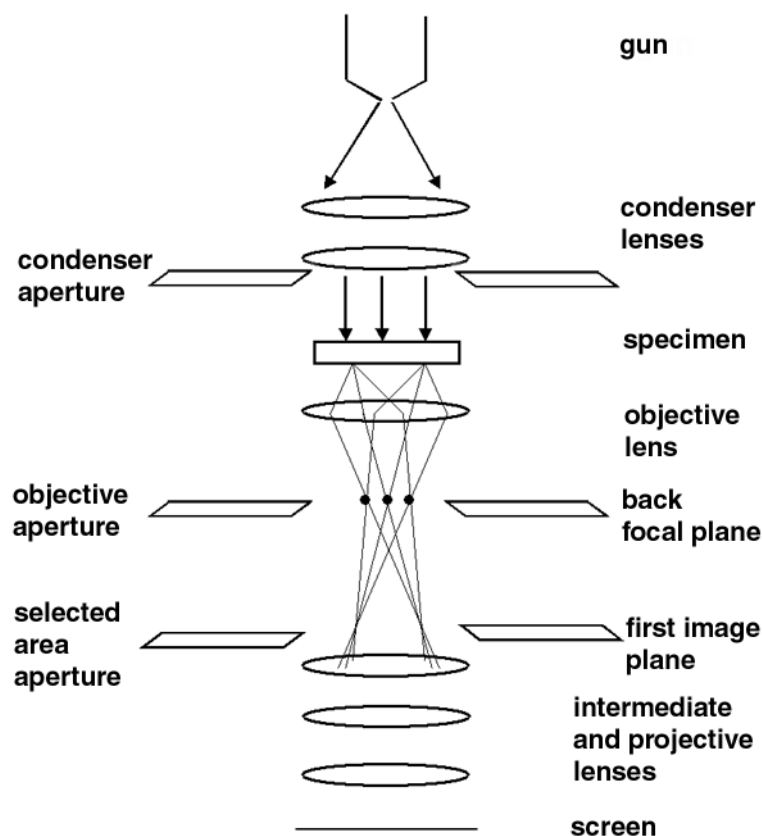
Fig. 3.1: *Schematic representation of a transmission electron microscope.*

system that consists of objective lense and aperture, intermediate and projective lenses and *(iv)* image recording system formed by the screen and photo recorder (camera or video).

The interaction of the electron beam with the object results in scattering of the electrons in the all directions. In the particular case of crystalline materials this results in electron diffraction. The variation of the image intensity due to variation of the object characteristics like thickness or composition defines the image contrast. For crystalline materials the image contrast depends on the orientation and lattice type. Additional contrast features may be due to lattice defects and to superposition of crystal slabs. Two types of imaging modes depending on the scattering processes can be applied. Bright-field imaging provides a distinct image contrast, available when excluding scattered or diffracted beams by means of an objective lens apperture. Dark-field imaging, i. e. selection of certain diffracted beams of the scattered electron wave by beam tilting or objective aperture displacement, is used for imaging specimen regions of specific orientation, structure or composition [Yac80, Hof82b, Hof82a].

TEM images provide only projections of three-dimensional objects. Information on the object topography (e.g. thickness changes) of crystalline objects is available by the weak-beam dark-field imaging mode [Yac80, Hof82b].

A crystal may be described in terms of a periodic arrangement of scattering elements (atoms, ions or molecules). The crystal lattice expresses this periodicity in three dimensions. Elastic scattering of an incident plane wave (electrons) by a crystal, i.e., a periodical distribution of identical scattering elements, causes diffraction effects. A geometric formulation of the diffraction condition is given by the Bragg equation

$$2d(hkl)\sin\theta = n\lambda \tag{3.1}$$

which describes the diffraction of electrons of wavelength λ by a set of lattice planes (hkl) of spacing d, n being the reflection order. Interaction of the electron beam with the object, situated in the front focal plane of the ojective lens, produces an intensity distribution in the back-focal plane where, e.g., beams diffracted by object regions of equal lattice characteristics (orientation, spacing) meet at the same position. This produces distinct spot patterns for one or few single crystals, or ring patterns for polycrystalline objects (or particulate objects with random orientation).

In this work the TEM investigations are performed with a conventional JEM 1010 transmission electron microscope operating at 100 kV accelerating voltage. The high resolution measurements are done with JEM 4000EX and JEM 4010 electron microscopes operating at 400 kV.

3.1.2   Sample preparation and image analysis

All used samples are in the form of powders which require another preparation method as for bulk or thin film samples [Wil96]. Agglomerated powders are first subject to milling in a mortar. Then the powder is dispersed in isopropanol (2-propanol) under vigorous shaking or using a ultrasound bath and a small quantity of the liquid is applied on a copper grid using a dropper. The copper grid (PLANO) is covered by a very thin perforated carbon film. This preparation method allows imaging of the specimen area above such holes without influencing the image contrast by the carbon layer.

The electron micrographs are digitized using a CCD-camera of TIETZ which gives an additional magnification of about $8\times$. From these digitized images usually more then 250 particles of a specific sample were measured to determine particle size and distribution. Two approaches were used to calculate the size distribution. The first one is taking the automatic measuring routines of the software being very useful in regions where the contrast of the substrate is not too high or where a background can be subtracted. The second way is by measuring each particle manually. From these data the mean sizes of the particles $\bar{d}$ and geometrical standard deviations σ_d are calculated using the statistical formula

$$\bar{d} = \frac{1}{n}\sum_{i=1}^{n} n_i d_i \qquad \text{and} \qquad \sigma_d = \left\{ \frac{1}{n-1}\sum_{i=1}^{n}(d_i - \bar{d})^2 \right\}^{1/2} \tag{3.2}$$

Alternatively, the particle statistics may be estimated from a fitting function of the histogram, e.g., a LogNormal function as described first by Granqvist [Gra76]. Metal particles with mean sizes below 20 nm can be fitted preferentially by LogNormal functions of the type

$$f_{LN} = \frac{1}{(2\pi)_{1/2}\ln\sigma}\exp\left\{-\frac{(\ln d - \ln \bar{d})}{2\ln^2\sigma}\right\}$$ (3.3)

where d is the particle diameter and $\ln\sigma$ is the logarithm of the standard deviation which is also a measurement of the width of the histogram [Gra76]. The coverage of the oxide surface by metal nanoparticles was estimated by considering the particle size distribution and the mean area density of metal nanoparticles.

For measuring the spacing of lattice plane fringes in HREM images either intensity plots across the fringe direction are used (real space evaluation) or the distance of reflexes in diffractograms obtained by Fourier Transformation (reciprocal space image evaluation). Prerequisite of both methods is the correct scaling of magnification applied to the digitized image.

3.2   Optical spectroscopy

The optical properties of the nanoparticulate composite materials were investigated by using optical spectroscopy in the visible region. To this aim a measuring system for thin film optical analysis of THEISS as schematically represented in fig. 3.2 was used. The system consists of a 50W stabi-
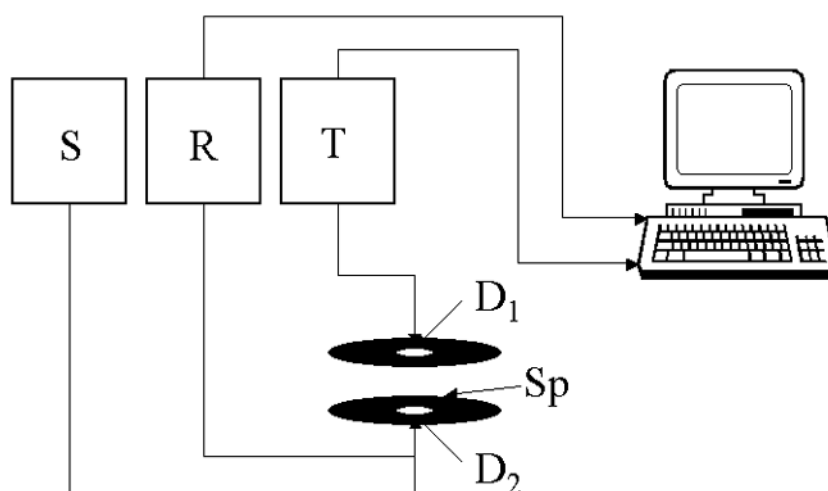
Fig. 3.2: Schematic representation of the optical spectrometer.

lized halogen ligth source (S), two ETA-CSB50 grating spectrometers with 512 pixel diode array for simultaneous measurement of transmittance (T) and reflectance (R) in the spectral range 380 to 1050 nm. The connection from the source to the sample stage is guided by quartz optical fibers. The spectrometer is connected and controlled via two serial ports to a computer where the spectra

are recorded using appropriate software. To reduce background signals and noise all measurements were done in the dark and averaged over multiple measurements (about 150).

Since the materials investigated were always obtained in powder form and the spectrometer is mainly suited for thin film measurements, appropriate sample preparation methods are needed. The first one used employs the dispersion of metal coated oxide nanospheres as powder in alcohol (e.g., isopropanol) or deionized water followed by dropwise or spinning deposition on microscope glass slides. The second preparation method uses a single component liquid adhesive of NORLAND for embedding the powder in a transparent thin film. The sample is homogenized and then dropped on microscope slides. For solidification the samples are exposed to UV-light (365 nm) for less than 5 minutes. The adhesive has a transmission higher than 95% in the spectral range 400 to 2000 nm, that was measured separately and has therefore no influence on the recorded spectra.

The optical properties of metal particles are deduced from the measurement of the *transmittance* defined as the ratio between the transmitted and incident ligth intensity $T = I/I_0$. The extinction coefficient is given by the Lambert-Beer law

$$\sigma_{ext} = -\ln T \tag{3.4}$$

To illustrate the connection of color and spectrum two examples are given of metal particles interspersed in between silica nanospheres. These samples have been prepared from a colloid-disperse solution of silica nanospheres of high weight percentage (40%). They have more or less regular arrangement of cavities in between the spheres wich may be utilized as template for metal nanoparticle formation by controlled reduction of metal complexes added to the solution and subsequent evaporation of the solvent. Fig. 3.3 shows a sample with silver prepared at room temperature (top) and gold (bottom) nanoparticles prepared at $60°$C on LUDOX SiO_2. The silica nanospheres used in these experiments have a mean size of 29 ± 4 nm being much smaller than as those used for nanoparticle coating experiments. By electron microscopy it could be shown that the metal particles have the tendency to precipitate in the cavities between the silica spheres. This finding is similar to that obtained for nanolithography with latex spheres, that produces two dimensional arrays of metal particles [Bur98, Bur99, Bur00].

The calculation of extinction spectra using the Mie theory for nanoparticles embedded in a dielectric matrix and the extension of this theory for core-shell structures is based on a programm described by Kreibig [Kre95] for dipolar approximation and one by Bohren [Boh98] for multipolar approximation. The programm for multipolar approximation solves the Bessel-Ricatti functions using backward recurrence. To achieve a better performance the limitations for the order of the calculated Bessel-Ricatti functions are changed using the size parameters proposed by Wiscombe [Wis79]. All calcualtions are performed by applying the size dependence of the dielectric function as given in equation (2.25).
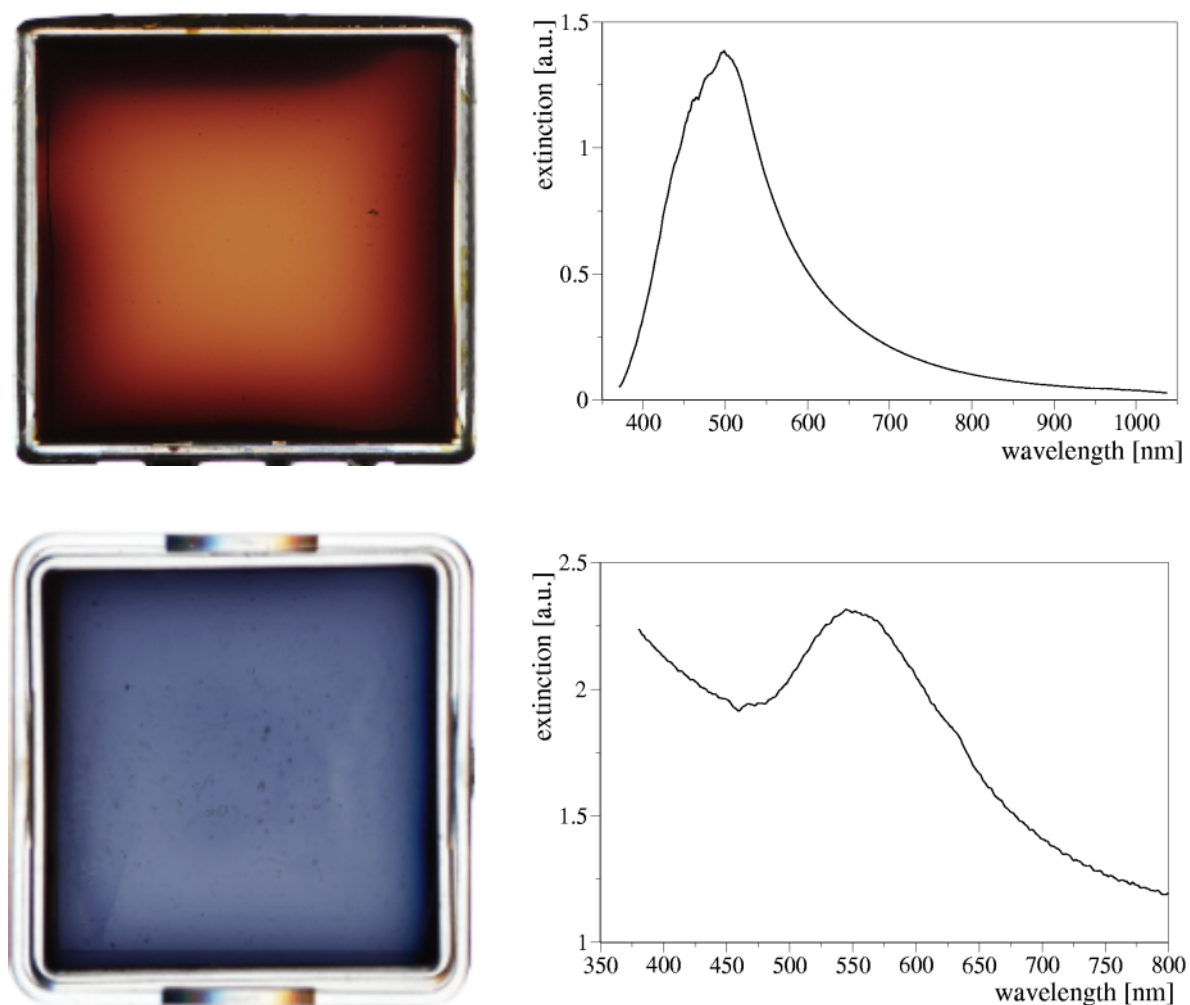
Fig. 3.3: *Silver (top) and gold (bottom) nanoparticles in colloid-disperse solution of silica nanospheres; left: photograph in transmission of the solution in a transparent box; right: extinction spectrum after drying.*

3.3   Electron paramagnetic resonance

The physico-chemical interpretation of paramagnetic resonance spectra requires to take into account the quantum mechanical description of atoms with several electrons. Since the quantum theory of electron magnetic resonance is well known from the literature (e.g. [Pak62, Mor80]) here only the techniques used for measuring and interpretation of magnetic absorbtion spectra are described.

The most important parameters which can be determined from electron magnetic resonance are the splitting factor (g-factor) characterizing the localization of unpaired electrons responsible for the absorption phenomena, as well as shape and width of the absorption line depending on type and strength of the interaction in the sample, and finally the line intensity depending on the number of unpaired electrons in the sample. In order to evaluate these parameters the measured spectra must be compared with calculated ones according to models which are already described in Chapters 2.2 and 2.3. The g-factor defines the Zeeman energy $h\nu_0 = g\mu_B H_0$ with μ_B being the Bohr magneton and ν_0 the resonance frequency. The electron paramagnetic resonance method is

used to investigate the interaction between particles, between particles and oxide support, and also oxide surface modifications due to metal precursor decomposition.
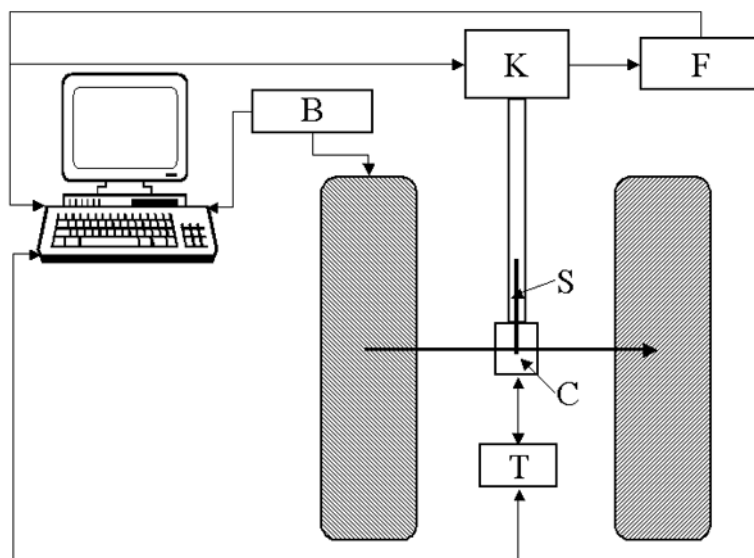
Fig. 3.4: *Schematic representation of the magnetic spectrometer.*

The electron magnetic resonance measurements are performed using a X-band spectrometer (ESR 220, ZWG Berlin-Adlershof), working at 9.3 GHz equipped with a frequency divider (K) and frequency counter 5215A (HEWLETT PACKARD) (F) and a nuclear magnetometer type MJ 110-R (RADIOPAN) (B) for measuring frequency and magnetic field. The schematic representation of the magnetic spectrometer given in fig. 3.4 present also the sample (S) and the microwave cavity (C). The measurements are made at various temperatures in the range of -150 to +150°C using controlled flow of liquid nitrogen for the low temperature range (T).

In order to measure the evolution of signals with time the as-prepared samples are sealed in quartz-tubes under vacuum during the first measurements. The quartz-tubes are exposed to the ambience only for subsequent electron microscopy and optical spectroscopy measurements, or for repeated measurements to keep track of sample stability under normal conditions.

The simulated magnetic resonance spectra are generated by means of appropriate programs translated to Borland Delphi 5. For ferromagnetic resonance the program considers the model proposed by Schlömann [Sch58] for both weak and large anisotropy and also the model proposed by Suran [Sur73] without taking into consideration the demagnetization energy. The program used to simulated the paramagnetic spectra is based on the theory proposed by Withe [Whi76] which takes into account only the spin Hamiltonian in the second order perturbation. There is a good agreement between the experimental and simulated spectra. Both Lorenzian and Gaussian line shapes are considered for all simulations in order to achieve better results.

From the temperature dependence of the relative intensity of the absorption signal the mean size of the particles can be calculated as described by Mörke [Mör90] using the relation

$$\frac{I(T_1)}{I(T_2)} = \frac{\coth\left(\frac{HvM_{s,T_1}}{T_1 k_B}\right) - \frac{T_1 k_B}{HvM_{s,T_1}}}{\coth\left(\frac{HvM_{s,T_2}}{T_2 k_B}\right) - \frac{T_2 k_B}{HvM_{s,T_2}}} \cdot \frac{M_{s,T_1}}{M_{s,T_2}} \tag{3.5}$$

or using the more general Griscom formalism [Gri81]

$$\frac{I_{T_1}}{I_{T_2}} = \frac{M_{S,T_1}}{M_{S,T_2}} \left[\frac{1-e^{-x}}{1-e^{-(2x-y)}} + \frac{e^{-y}}{1-e^{-y}} \left[\frac{1}{x}(x-y)(1-e^{-2x}) - (1-e^{-2(x-y)})e^{-y} \right] \right] \tag{3.6}$$

where $x = M_{S,T_1} vH/(k_B T_1)$ and $y = g\mu_B H/(k_B T_1)$, M_{S,T_1} represent the saturation magnetization at temperature T_1, v is the volume of the particles, H the intensity of the magnetic field, and k_B is Boltzmann's constant. $I(T_1)$ and $I(T_2)$ represent the derivative of the signal intensity taken at temperatures T_1 and T_2, respectively.

4 Exploration of appropriate oxide materials

The oxide materials used in this work must meet several requirements. Serving as support of the metal nanoparticle coating they should exhibit a dielectric function that causes not too much redshift and broadening of the surface plasmon resonances [Kre97a] since this will affect the optical properties of core-shell structures. As building blocks for the nanostructured material they should be available in form of non-coherent powder grains of nearly spherical shape and equal size with nanometer dimensions. The metal deposition applied to form core-shell-like structures should lead to a stable adhesion of metal nanoparticles on the oxide surface. To obtain a controlled metal particle coating we studied various types of oxide material and explored how they are suited for this purpose. The appropriate conditions include also knowledge on terminating surface groups. Information on the number of such groups is obtained by *ThermoGravimetric Analysis* (**TGA**) as described below.
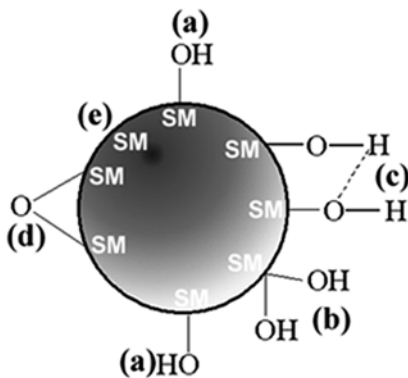
Fig. 4.1: *Termination groups on the oxide surfaces: (a) to (c): isolated, geminal, vicinal hydroxyl groups, (d) oxygen bridges, (e) free atoms.*

Under ambient conditions the surface of the considered oxide is generally characterized by four types of termination groups: three different configurations of OH-groups (isolated, vicinal and geminal) and SM-O-SM bridges (SM = Si, Ti, Al, Fe), schematically presented in fig. 4.1. Studies of these termination groups show that their concentration is strongly dependent on a thermal pretreatment. The desorption of water by drying the oxide surface at different temperatures in vacuum or in inert gas atmosphere follows the reaction
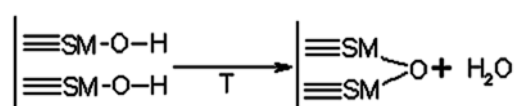
The temperature dependence of various termination groups at the surface of amorphous silica as derived from Zhuravlev's model [Zhu00] is presented in fig. 4.2. In this model the number of
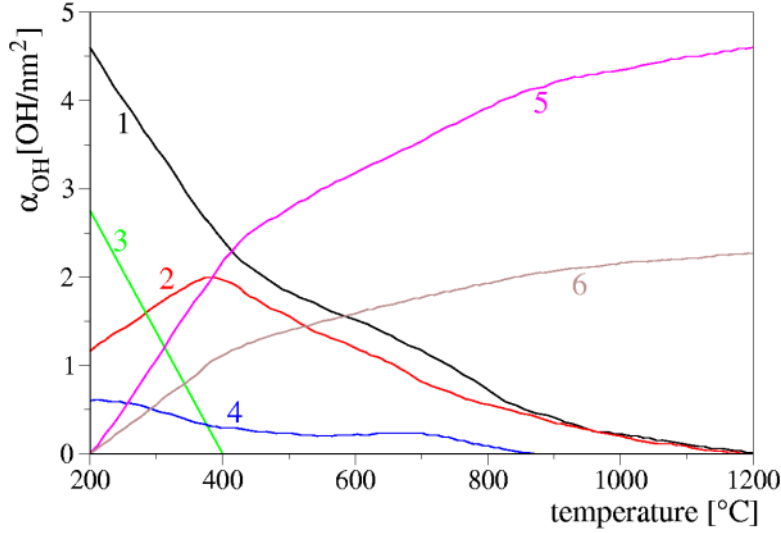
Fig. 4.2: *Temperature dependence of the concentration of different OH-groups: total (1), isolated (2), vicinal (3), geminal (4), Si-O-Si bridges (5), and Si atoms (6) [Zhu00].*

OH-groups on the surface is considered as a constant (Kiselev-Zhuravlev constant α_{OH} = 4.6 OH-groups/nm^2) for temperatures lower than 200°C. Upon increasing the temperature up to 400°C the total water content on the surface is considered to be desorbed. This model can be also applied to other oxides.

However, using infrared spectroscopy Peri [Per60] could show that on γ-Al$_2$O$_3$ water traces are present even after drying the sample at 1000°C. He concluded that at about 400°C all water molecules are removed and only hydroxyl groups remain on the surface. Using the same method Knözinger [Knö78] found that at 100°C the surface contains 13.5 OH-groups/nm^2, decreasing to 9.5 at 200°C and to 5 at 400°C. Gunter [Gun97] observed that the number of OH-groups decreases to half of the fully hydroxilated value at about 650°C. Studies about the OH-groups on TiO$_2$ in the anatase phase [Vee89] also indicate a nonhomogenous population of the surface due to two types of OH-groups with basic and acid character. The dehydroxilation of TiO$_2$ takes place at 500°C.

To get an estimate of the number of OH-groups per weight unit of the oxide materials *Thermo-Gravimetric Analysis* (**TGA**) together with *Differential Thermal Analysis* (**DTA**) using an DTA-TGA apparatus was performed. This technique compares the temperature of the sample with a standard reference during a programmed change of temperature [Wes98a]. If the specific surface area (SSA) is known then the corresponding amount per surface area can be calculated. For example, the number of OH-groups on the surface of silicon dioxide can be estimated from the Zhuravlev model [Zhu00] by the relation

$$n_{OH} = \alpha_{OH} \cdot SSA \cdot m_{ox} \times 10^{18} \tag{4.1}$$

where m_{ox} is the weight of the used oxide in g, and SSA is given in m^2/g.

Our DTA-TGA measurements used Al$_2$O$_3$ as standard reference. The temperature, measured by Pt thermocuples, was varied from 40 to 1000°C at a rate of 10K/min. The measurements were

recorded in flowing air with a flow rate of about 12 l/h. The number of OH-groups per gram of oxide were determined from the TGA measurements by:

$$n^g_{OH} = \frac{2 \cdot \Delta m \cdot M_{ox} \cdot N_A}{(100 - \Delta m)^2 \cdot M_{H_2O}}$$

(4.2)

where Δm is the relative weight loss, M_{ox} and M_{H_2O} are the molar mass of the oxide and water respectively, and $N_A = 6.022 \times 10^{23}$ mol^{-1} is the Avogadro number.

4.1 Mesoporous oxide materials

Mesoporous oxide materials were examinated because they exhibit a high specific surface area, and accordingly, a high number of OH-groups on the surface available for chemical interaction with metal complexes or atoms. SiO_2 and γ-Al_2O_3 produced by MERCK were chosen for testing a number of transition metals from various precursor complexes in deposition experiments. The specific surface area is 250 m^2/g for silica and 190 m^2/g for alumina. In fig. 4.3 electron microscopy images of these oxides are shown. The silica consists of very small grains of non-
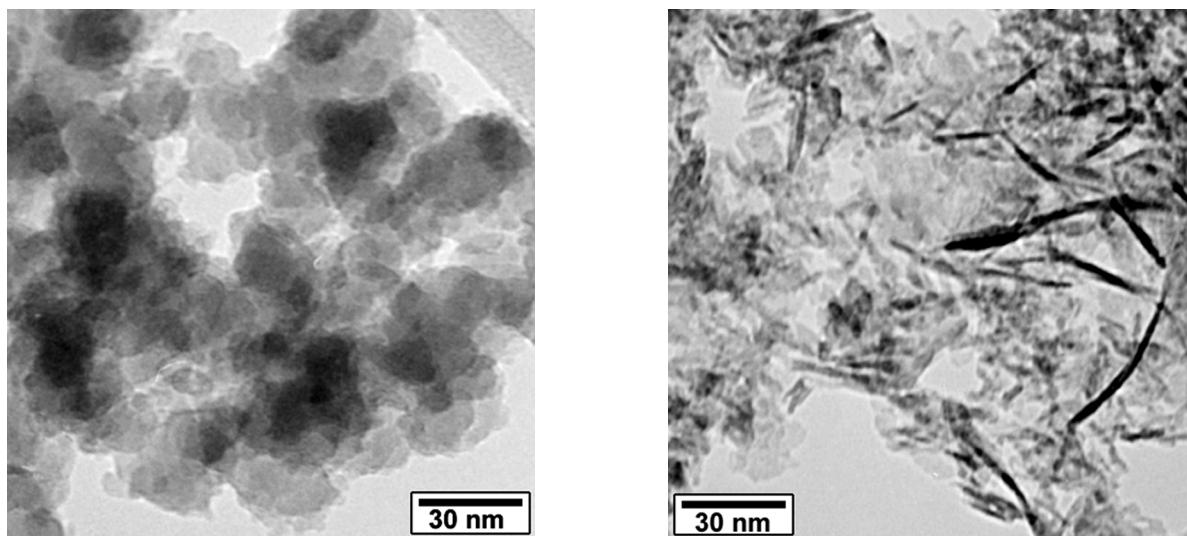
Fig. 4.3: TEM images of mesoporous SiO$_2$ (left) and γ-Al$_2$O$_3$ (right).

regular but roughly spherical shape, having a rather coarse surface. The alumina consists of even more irregular, namely needle-like grains that also exhibit a certain crystallinity while the silica is completely amorphous. The thermogravimetric measurement of this SiO_2 is presented in fig. 4.4. Using equation (4.2) we estimated that at 70°C the sample contains 22.7 OH-groups/nm^2 while at 200°C it contains only 7.8 OH-groups/nm^2.

The mesoporous oxide materials were pretreated by LiAlH$_4$ to modify their surfaces [Dre98, Mör96] and to replace terminating OH-groups by alumium-hydrogen surface complexes [Rud81]. The termination groups of the mesoporous silica, hydride-modified this way, are schematically shown below.
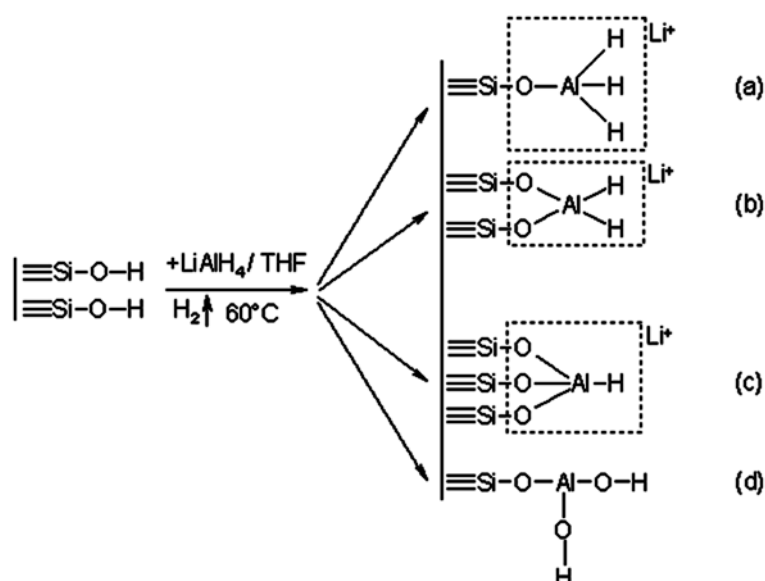
The preparation procedure of hydride modification was as follows: the mesoporous silica was treated in vacuum at 200°C for 2 hours and than dispersed in THF. A solution of saturated $LiAlH_4$ in THF was added and soaked until the hydrogen formation was finished. The modified sample was washed with THF and dried at various temperatures. Not all OH-groups are eliminated (see complex (d) in the scheme above) by this pretreatment. As the DTA-TGA measurements show, on the silica modified at 200°C only 3.3 OH-groups/nm^2 remain. Comparing this value with the value of untreated silica we can conclude that the modified silica has about 40% less OH-groups on the surface. Despite of the non-regular shape and the rough surface of the mesoporous oxides, which complicates imaging of very small particles, they are well suited for studying particle formation because of their high content of surface groups, which may serve as active sites in the formation and adhesion of metal particles.
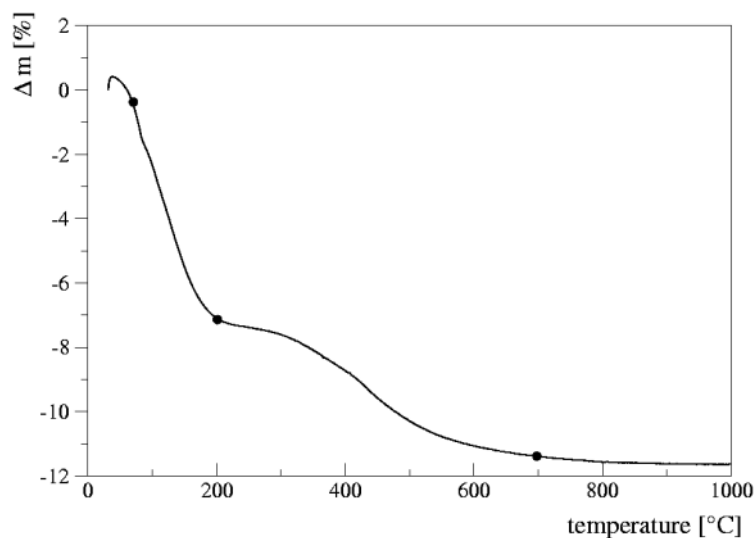
Fig. 4.4: Temperature dependence of the weight loss of mesoporous SiO_2.

4.2 Polydisperse oxide particles of spherical shape

In a second approach we explored polydisperse particles of various oxides having nearly spherical shape. Such oxide nanospheres are commercially available in the form of powders. We studied powders with parameters summarized in Table 4.1. Due to the mostly applied pyrolysis route of synthesis of these oxides they exhibit distinctly smaller specific surface area parameters than the mesoporous ones. From electron microscopy imaging (see fig. 4.5) one may recognize that the oxide nanospheres exhibit a rather smooth surface.

Table 4.1: *Characteristics of polydisperse oxide spheres from different providers*

Oxide	Provider	Specific Surface Area [m^2/g]	Density [g/cm^3]	Mean size [nm]
SiO_2	NANOTEK	70	2.6	33
γ-Al_2O_3	ALPHA AESAR	44	3.96	34
γ-Al_2O_3	NANOTEK	44	3.6	38
α-Fe_2O_3	NANOTEK	43	5.2	27
TiO_2	ALPHA AESAR	45	4.26	31
TiO_2	CERAC	45	4.2	32

TEM analysis of these materials results in mean values partially differing from the product specification. In addition, a broadened size distribution was noticed for most of them. The measured mean size and standard deviation are summarized in Table 4.2.

Table 4.2: *Mean size and standard deviation measured from TEM images*

Oxide	Provider	Mean size [nm]	St. dev. [nm]
SiO_2	NANOTEK	40.2	33.7
γ-Al_2O_3	ALPHA AESAR	23.1	19.4
γ-Al_2O_3	NANOTEK	27.1	18.8
α-Fe_2O_3	NANOTEK	22.4	18.1
TiO_2	ALPHA AESAR	24	12
TiO_2	CERAC	44.4	24.5

To give some examples, fig. 4.5 show characteristic TEM images and the size distributions of NANOTEK SiO_2 (upper) and Fe_2O_3 (lower) nanospheres.

From fig. 4.5 the difference between amorphous oxide nanospheres like silica and crystalline ones like iron oxide may be recognized. While the image contrast of the silica nanospheres is determined by the sphere radius and superposition of several spheres, additional contrast features of iron oxide nanospheres result from various orientations of the crystal lattice with respect to the electron beam, and from the presence of crystal lattice defects. The crystalline materials have been examined also by electron diffraction in order to determine the lattice type. As an example, the TiO_2 nanospheres of CERAC exhibit two phases of titania: anatase and rutile. The intensity of the measured diffraction rings and the tabulated [Edi91] ring positions with the crystallographic
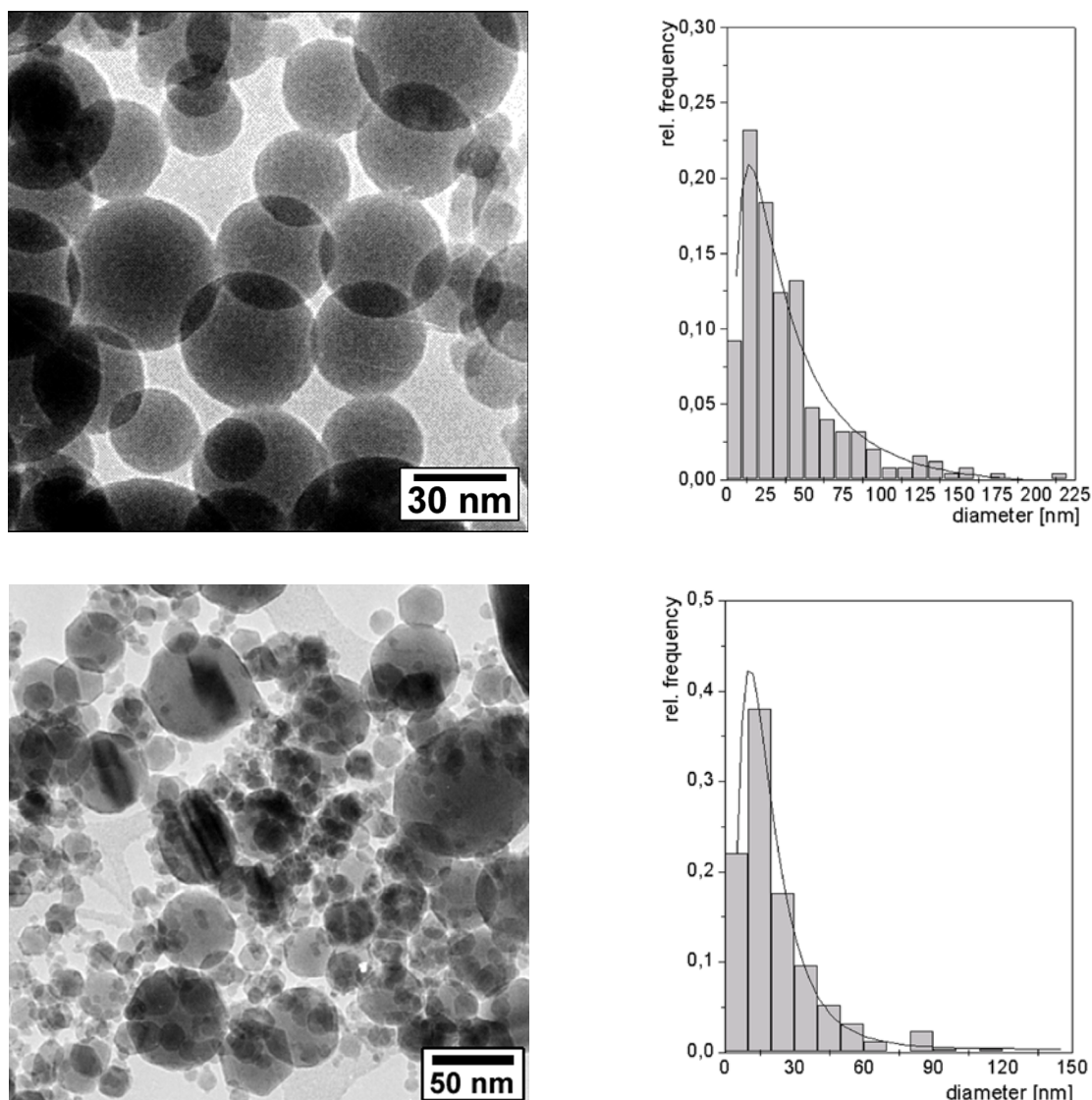
Fig. 4.5: *TEM image and size distribution of silicon dioxide (upper) and iron oxide (lower) produced by* NANOTEK.

indices indicated are shown in fig. 4.6. From this analysis we may state that both phases of titania are present in the material.

The α-Fe$_2$O$_3$, γ-Al$_2$O$_3$, and other TiO$_2$ materials listed in Table 4.1 were also studied by electron microscopy. These crystalline oxide nanospheres exhibit various types of planar lattice defects like twin boundaries which may cause line defects like grooves where they emerge to the surface. To a certain extent also deviations from the spherical shape by the presence of crystalline facets are observed. Such surface defects may play a role in the accommodation of metal particles formed by deposition from appropriate precursors. The pyrolysis technique used in the fabrication of the most commercial oxide nanospheres, is performed at very high temperatures (above 1000°C) and this is also reflected in the results of the DTA-TGA measurements. At such high temperatures no OH-groups can remain on the surface. Our measurements show a very low number of OH-groups (less then 0.5 OH-group/nm^2) for these materials. This result is due to the fact that the samples have been stored under normal atmosphere conditions.
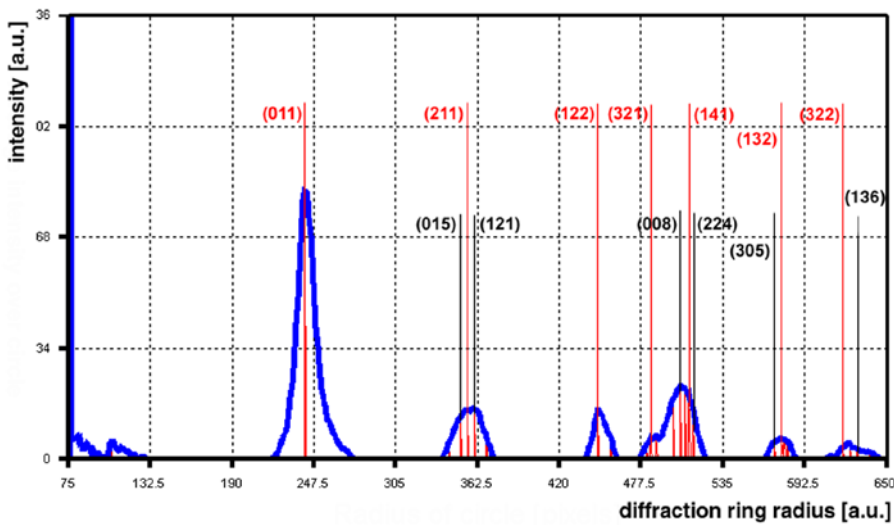
Fig. 4.6: *Intensity of the diffraction rings and tabulated ring position for anatase (black lines) and rutile (red lines) with crystallographic indices indicated.*

The use of purchasable, polydisperse oxide nanospheres in studies of metal nanoparticle coating has the advantage that different oxides of various origins, mostly available in polydisperse form only, may be compared. However, the very small size fraction of these materials tends to form agglomerates and occasionally they decorate the larger spheres in such a way that the smaller oxide particles may be confused with metal particles. Moreover is the optical analysis more difficult due to the polydispersity of these oxides.

4.3 Monodisperse silica nanospheres

A more thorough study of new materials with potential application as sensors or optical devices governed by novel physical properties requires monodisperse nanospheres. Only this configuration allows to combine in a defined manner the properties of both, the oxide nanospheres and the metal nanoparticle coating. We explored the characteristics of two different classes of such oxide materials. The first one concerns silica nanospheres in the form of powder. A few have been commercially available like Monospher^{TM} 100 with a mean size $\bar{d} = 94.5 \pm 11.4$ nm and Monospher^{TM} 250 with $\bar{d} = 215 \pm 30.5$ nm produced by MERCK KgaA. A TEM image and the size distribution of the 250 nm sample are shown in the upper part of fig. 4.7. This sample contains also a small amount of nanospheres with a mean size of 95.5 ± 7.8 nm (one may be seen in the figure).

Table 4.3: *Monodisperse silica nanospheres in liquid solution*

Name	Producer	Mean size [nm]	St. dev. [nm]
Levasil 100	BAYER	33.5	3.7
Levasil200	BAYER	22.7	8.9
Ludox TM 40	DU PONT	28.6	4.0
MA-ST-M	NISSAN	29.5	6.8
Snowtex 50	NISSAN	33.0	5.3

For more flexibility with respect to the size we used monodisperse silica nanospheres synthesized by the Stöber route [Stö68, Gie00b, Gie94a, Gie94b]. This preparation method and control
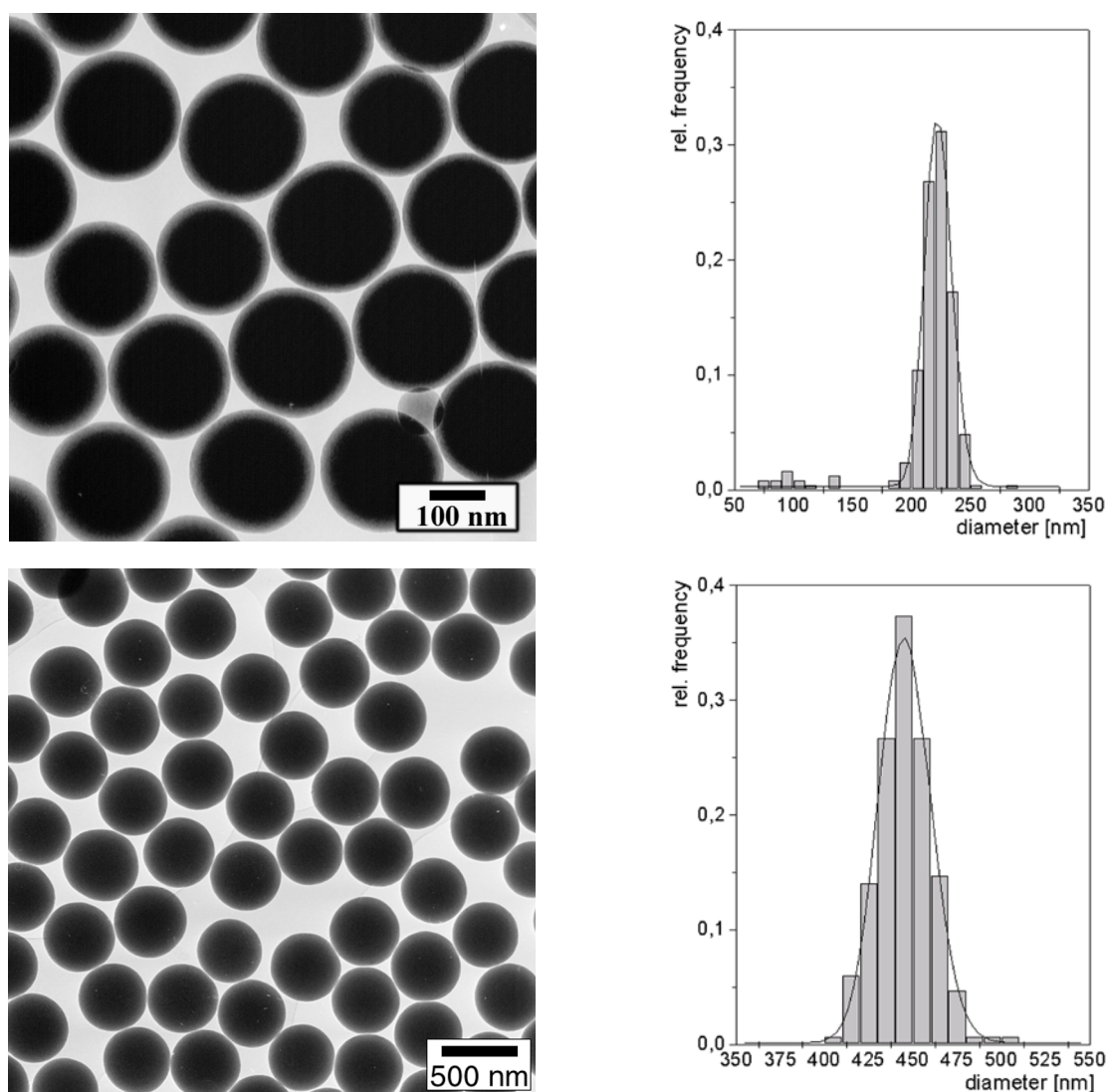
Fig. 4.7: *TEM image (left) and size distribution (right) of Monospher^{TM} 250 (top) and Stöber silica (bottom).*

of the nanosphere size will be described below. As an example, the lower part of fig. 4.7 shows TEM image and size distribution of a 450 nm sample. From both images one may recognize that these nanospheres exhibit a rather smooth surface.

A second class of monodisperse nanospheres are colloid-disperse solutions of oxides like silica or alumina. We studied some commercial silica materials which are sumarized in Table 4.3. These oxide nanospheres usually exhibit a rather small size and their surface is not as smooth as that of the ones in powder form. With the exception of MA-ST-M which is a suspension in methanol, all other materials used are in aqueous solution.

4.3.1 Preparation of monodisperse silica nanospheres using the Stöber method

More flexibility than with commercial materials is achieved with laboratory-made nanospheres which were received in the frame of a joint project from Dr. W. Mörke (Merseburg).

The preparation of Stöber monodisperse silica [Stö68] uses tetraethoxysilane, (TEOS = $Si(OC_2H_5)_4$) as starting material and ethanol as solvent. The reaction takes place in the presence of water and ammonia is used as catalysts to initiate hydrolysis and condensation.

The size of the silica nanospheres can be very well controlled by the molar concentration of TEOS, water and ammonia and the mean size can be calculated using the Bogush [Bog99] relation:

$$d = A[H_2O]^2 exp(-B[H_2O]^{1/2}) \tag{4.3}$$

where the square parentheses represent the molar concentration in mol/dm^3 and the constants A and B are defined as:

$$A = [TEOS]^{1/2}(82 - 151[NH_3] + 1200[NH_3]^2 - 366[NH_3]^3)$$

$$B = 1.05 - 0.523[NH_3] - 0.128[NH_3]^2$$

Fig. 4.8 gives a three-dimensional representation of the dependence of the mean size of the silica nanospheres as a function of the water content and NH$_3$ concentration used for the preparation.
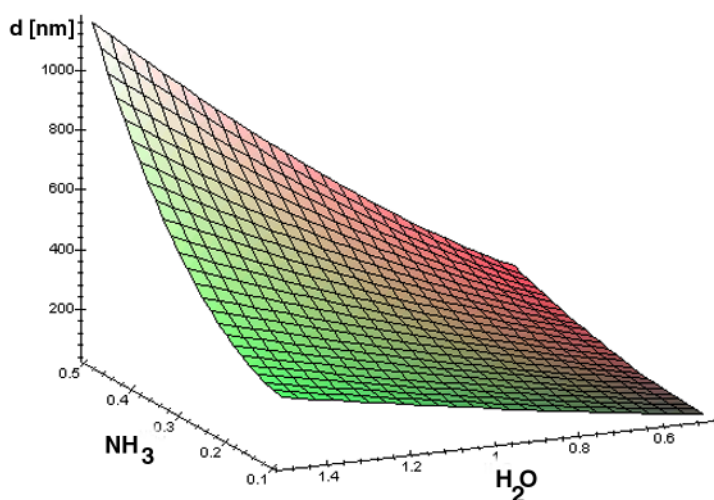
Fig. 4.8: *Calculated mean size of silica nanospheres as a function of the water and ammonia molar concentration in mol/dm^3.*

A typical preparation is carried out as follows: 13.5 ml NH$_3$ (32%) was mixed with absolute ethanol in a 100 ml flask. A second 100 ml flask was filled with 8.32 g TEOS and absolute ethanol. The first solution was stirred at 1000 min^{-1} in a 500 ml flask adding the second solution. The mixture was stirred for 15 seconds, and after two hours waiting the solution was centrifuged. The sample was dried then at 100°C for three hours. TEM analysis of this material gives a mean size of about $\bar{d} = 163 \pm 40$ nm. Further drying of the sample for three hours at 50°C decreases the mean size to $\bar{d} = 133 \pm 12$ nm. Overnight drying of the sample at 100°C further reduces the size to $\bar{d} = 105 \pm 26$ nm and simultaneously broadens the size distribution. Addition of water to the mixture increases the mean size, in particular for high NH$_3$ content. An example of laboratory-made Stöber silica is given in fig. 4.7 together with corresponding size distribution. As may be
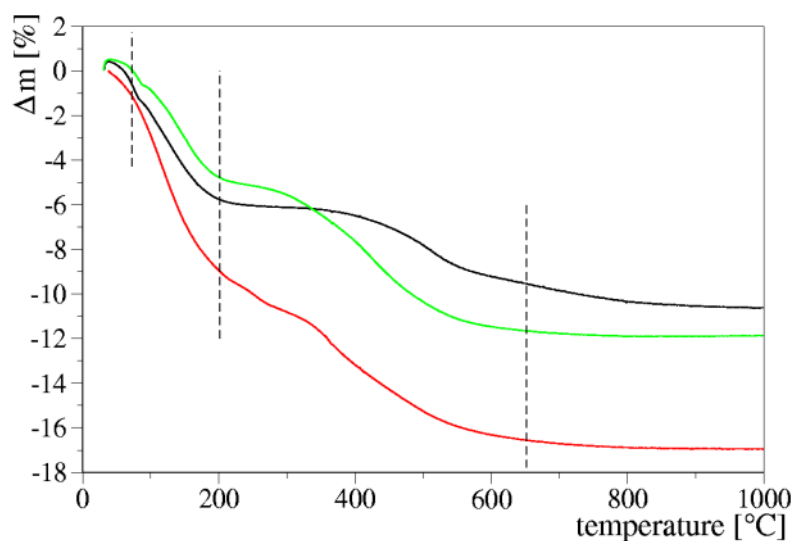
Fig. 4.9: *Temperature dependence of the weight loss of silica nanospheres of* MERCK *(black), and after Stöber (red). The green curve is measured at the Stöber sample upon further drying at 50°C for 3 hours.*

seen from fig. 4.8, this method allows to vary the nanosphere size in a rather broad range. Below about 30 nm diameter, however, certain deviations from the spherical shape occur.

Various silica nanospheres were prepared according to the Stöber method with a mean size ranging from 133 to 300 nm depending on the amount of water and the concentration of ammonia.

To characterize the content of surface groups like OH we performed TDA-TGA measurements of the Monospher^{TM} 250 (black line) and the Stöber material (red line) as presented in fig. 4.9. In the same figure also the measurement of the Stöber sample upon further drying at 50°C is shown (green curve). From this it may be seen that the number of OH-groups on the Stöber nanospheres is higher than on the analog commercial materials. Drying for longer times reduces also the water content of the sample.

With respect to the intended application of oxide nanospheres with metal nanoparticle coating, the commercial monodisperse silica materials are well suited because of their narrow size distribution. From the viewpoint of effectivity of the coating procedure, however, the Stöber materials are more promising because of their very high content of surface OH-groups (17 to 20 OH-groups/nm^2).

5 Metal nanoparticles on non-planar oxide surfaces

5.1 Routes to metal nanoparticle coating of non-planar oxide surfaces

While on planar substrates a number of vacuum-based deposition methods may be utilized, including physical and chemical vapour deposition, laser ablation and cluster beam deposition, and also spin-coating techniques are employed, the situation is different with non-planar substrates because of their peculiar geometry. This requires access of the deposit species not only from one, but from all directions which may be achieved in a gas stream or in solution. For practical reasons solution methods are mostly preferred. Then one may choose between methods utilizing the deposition of nanoparticles from a colloidal route of synthesis or methods of particle formation directly on the surface by appropriate processes. The first path includes electrostatic deposition of colloidal particles by means of adhesives like polyelectrolytes covering the oxide surface [Gie97, Rog00] and ligand-mediated immobilisation of metal colloids on functionalized oxide surfaces [Old98, Wes98b]. The second path includes controlled chemical reduction, photochemical or radiation-chemical, photocatalytic and sonochemical reduction [Yon91, Kou82, Oki96]. The controlled reduction of precursor molecules on the oxide surface [Mör94, Dre98, Dok99, Gom00, Zou93] has two main advantages: *(i)* avoid uncontrolled surface chemical interaction of the metal particles with functionalizing agents which may seriously influence the surface plasmon resonances [Tem00, Hod00]; *(ii)* enable control of the precursor decomposition kinetics and therefore the particle size at moderate temperature conditions [Mic00, May00]. By varying the coating conditions (pH, concentration, temperature and duration of exposure of the metal complex solution) the coverage of the oxide nanospheres and size of metal nanoparticles may be controlled [Dok99].

The aim of achieving metal particle coatings on oxide nanospheres was approached in several steps. First, deposition of a number of transition metals on hydride-modified non-planar oxide materials has been studied to advance understanding of the structural and functional characteristics of the oxide surface [Bra00, Fuj00, Kha00, Kos00, Rim00, Sch00, Wel00] in dependence of pretreatment, modification and metal loading. This is more or less the basis of the following steps and it will be presented in sections 5.2 and 5.3 of this chapter. Second, metal deposition from organometallic precursors of the type $[Li(THF)_2]_2 \cdot [MR_4]$ on oxide surfaces of well

defined hydroxyl concentration was applied to polydisperse oxide nanospheres. This study has been carried out for two reasons:*(i)* to control the decomposition under moderate conditions of the precursor molecules and therefore the size of the particles, *(ii)* to limit the surface contamination [Ver99, Vid99]. Since these were the first attempts to achieve core-shell structures they will be presented in Chapter 6.2. Third, deposition of silver and gold on monodisperse Stöber silica nanospheres by incipient wetness impregnation using water soluble metal complexes. These nanoparticle coating experiments yielded reasonably dense coverages resulting from one- and two-step prenucleation procedures. They will be presented in Chapters 6.3 and 6.4.

5.2   Formation of metal particles on hydride-modified oxide

In an extensive study aimed at improving the knowledge on particle formation under relatively low temperature conditions on non-planar oxide surfaces not only various types of metals, like superparamagnetic, group IB and group VIIIB metals, but also two generic types of metal precursors were explored. The synthesis were performed by Prof. H. Drevs and Mrs. K. Lehrack (Merseburg).

The first precursor of type $MX_n \cdot n$Lig contains metal complexes with anions "X" like Cl^- or Br^- and associated ligands "Lig" like *tetrahydrofuran* (THF) $\{C_4H_8O\}$ or *tetrahydrothiophen* (THT) $\{C_4H_8S\}$. The second precursor of type MX_n contains metal complexes with anions X like *acetylacetonate* (acac) $\{-[(CH_3)_2HC_3O_2]\}$, *mesityl* (mes) $\{-[(CH_3)_3C_6H_2]\}$ or *triphenylphosphine* (PPh$_3$) $\{-[(C_6H_5)_3P]\}$. The metal complexes obtained from MERCK and CHEMPUR are used without further purification. The oxide materials, silica and alumina from MERCK, were subjected to a dehydroxylation treatment as described in Chapter 4.1 resulting in about 0.8 hydride ions per aluminium atom, as estimated by reaction with hydrochloric acid. The relation between hydride ions and the metal content after metal loading and decomposition of the metal precursors was about 5:1.
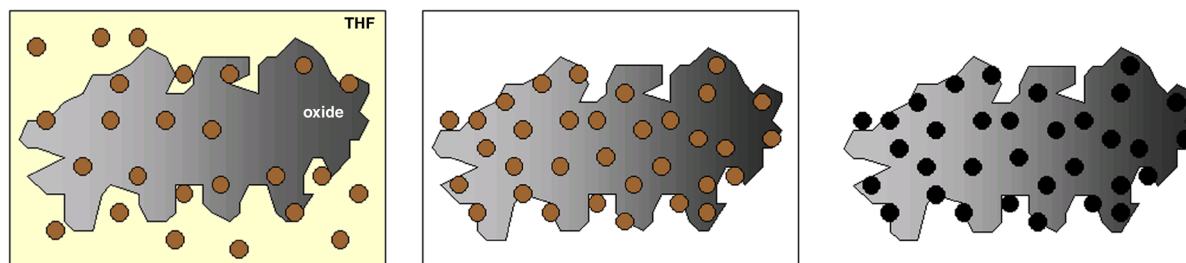
Fig. 5.1: *Schematic representation of the metal deposition procedure: (left) suspension of hydride-modified oxide in THF with the metal complex added; (center) fixation of the metal complex indicated by discoloration of the solution; (right) formation of metal particles upon drying at elevated temperatures.*

The metal deposition procedure involves several steps as presented schematically in fig. 5.1. At first, a suspension of the hydride-modified oxide (typically 5 g) in THF is prepared with the

metal precursor added in required quantity, see fig. 5.1(left). Then the solution is shaken until it becomes colorless, which indicates that the metal complex is fixed at the oxide surface, see fig. 5.1(center). After being filtered, the sample is washed in THF and dried in vacuum at elevated temperatures.

As a result the metal precursors are reduced to metal atoms which may aggregate to form nanoparticles. This step, including nucleation and growth processes, is schematically presented in fig. 5.1(right).

The formation of metal atoms by precursor decomposition follows the reaction:

$$n\left[\equiv Al - H\right] + MX_n \cdot nLig \longrightarrow n\left[\equiv Al - X\right] + M^0 + nLig + \frac{n}{2}H_2\uparrow$$
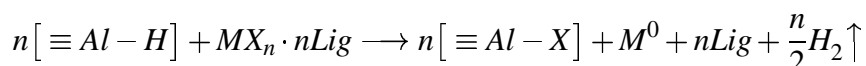
The dried samples are sealed off in quartz tubes under vacuum (about 10 mbar) for further investigations. For most of the metal complexes heating to 100 or 300°C for 1 h was sufficient to induce metal particle formation. An exception was the Ir complex that required heating to 400°C since at lower temperatures no unambiguous metal particle formation was obtained.

5.3 Characterization of metal particles on hydride-modified oxide

5.3.1 Particles of ferromagnetic metals

Nanoparticles of superparamagnetic metals are expected to exhibit unusual properties when they are arranged in a regular manner like in ferrofluids. Even though there is already some literature available about studies on planar arrays of such particles [Joh99, Gie00a], nothing is known on their properties when they adopt arrangements of spherical geometry or even core-shell structures. Although it is beyond the scope of this work to follow this issue in detail, we performed some experiments with Ni, Co and Fe to study in a first attempt structural characteristics and magnetic resonance of such materials.

The mean size and standard deviation of superparamagnetic metal particles prepared from various precursors upon drying at 100 and 300°C are compiled in Table 5.1. Fig. 5.2 shows a characteristic image of Ni particles on hydride-modified silica upon drying at 300°C together with the corresponding size distribution from which the mean particle size is determined.

Table 5.1: Mean size of superparamagnetic metal particles by TEM

Precursor	100°C		300°C	
	Mean size [nm]	*Stand. dev.* [nm]	*Mean size* [nm]	*Stand. dev.* [nm]
Ni(acac)$_2$	2.2	0.4	2.5	0.2
CoBr$_2$·2THT	2.3	0.6	2.4	0.7
Co(acac)$_2$	2.4	0.4	2.6	0.5
FeBr$_2$·2THT	3.3	0.7	2.3	0.5

The shape of the size distribution is fitted (black curve) by a Log-Normal function [Kis99]. As one may recognize from Table 5.1, Ni nanoparticles do not show a distinct size increase if the drying temperature is enhanced from 100 to 300°C. The coverage of the silica surface, roughly estimated by assuming a thin film of a thickness equal to the mean oxide grain size, slightly increases from 15 to 19%. If, however, the metal loading is increased from 1 to 3% by enhancing the amount of
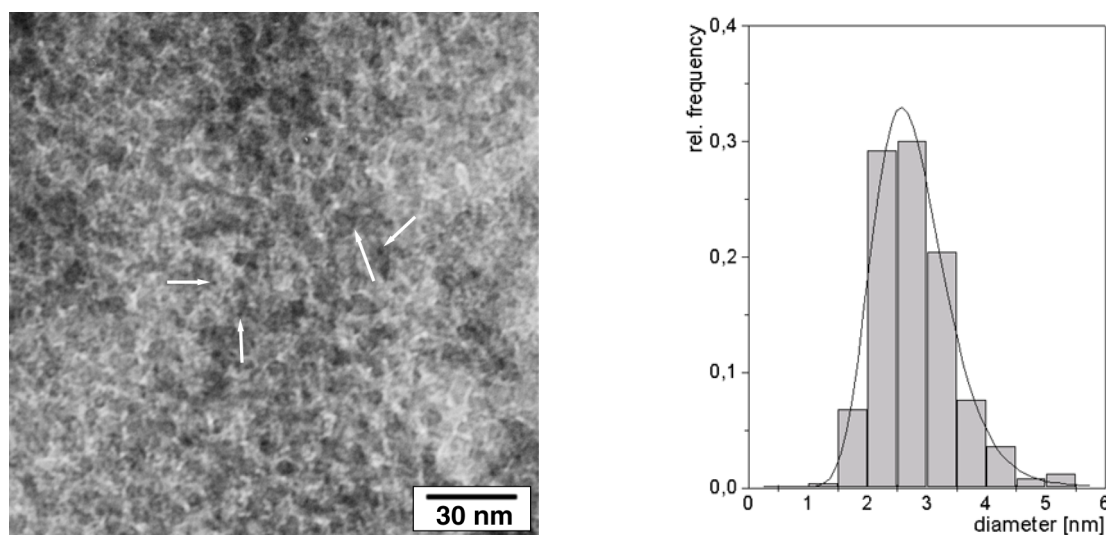
Fig. 5.2: *TEM image and size distribution of Ni nanoparticles on SiO$_2$ dried at 300°C.*

metal precursor added to the silica suspension, we obtain particles of 3.0 ± 0.5 nm and 3.2 ± 0.5 nm mean size as well as 18 and 22% coverage for drying at 100 and 300°C, respectively. It may be noticed that in all cases a uniform coverage of the silica surface by metal particles was achieved.

The collective magnetic properties of superparamagnetic nanoparticles are characterized by their FMR spectra as well as by the temperature dependence of the corresponding parameters like the relative experimental intensity. The room temperature ferromagnetic resonance of Ni particles

Fig. 5.3: *Magnetic resonance spectra of Ni nanoparticles on silica dried at 300°C: experimental (black) and calculated curve (red).*

prepared at 300°C is shown in fig. 5.3 (black curve) together with a calculated spectrum (red curve). The experimental spectrum exhibits a main resonance at H= 315 mT (g = 2.18). For the

calculation, according to the model of Suran [Sur73] described in Chapter 2.2, a Lorentz line shape was used fitted with $\Delta H_{pp} = 19.2$mT and the anisotropy coefficients $K_a = -0.0095$; $K_1 = 0.0494$; $K_2 = -0.0381$. Differences between calculated and measured spectra mainly result from the finite width of the size distribution of the Ni particles present, whereas the calculation considers only one fixed particle size. To allow to determine the particle size from the ferromagnetic resonance, the spectra were measured at various temperatures in the range of -150 to $150°C$. A broadening of the linewidth as well as an increase of the intensity with decreasing temperature is observed which demonstrates the Curie-like behaviour of these particles. Simultaneously, a shift of the resonance position (g-factor) ranging from 0.01 to 0.2 occurs. For the size determination a model developed by Mörke [Mör90] was used and from the spectra recorded at -125 and $100°C$ according to equation (3.5) a particle size of 2 nm was obtained. This agrees fairly well with the mean particle size derived from TEM measurements. There is a small signal in the measured spectrum at H $\simeq 335$ mT (g = 1.99) that may result from Ni^+ ions remaining from metal complexes not reduced by aluminium hydride surface groups.
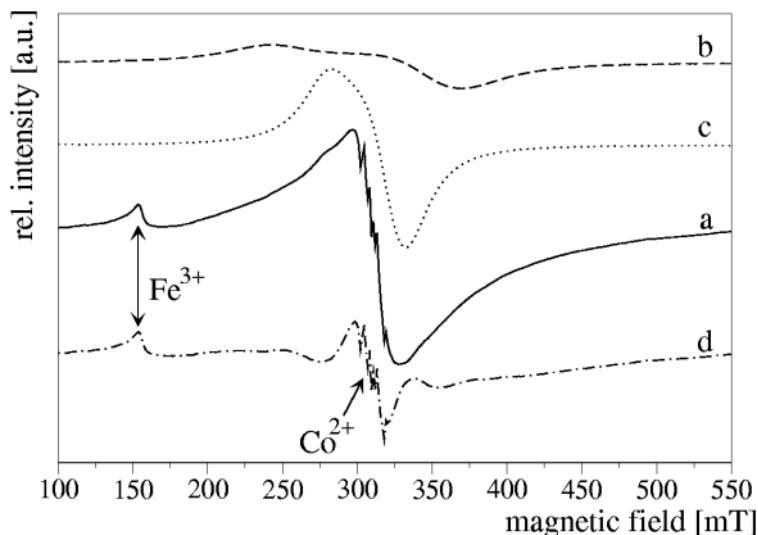
Fig. 5.4: *Magnetic resonance spectra of Co nanoparticles on silica dried at 100°C: (a) experimental, (b) and (c) calculated curves using the Suran model; (d) difference spectrum: a-(b+c).*

The more complicated spectrum of Co nanoparticles, shown by curve (a) in fig. 5.4 for the 100°C sample prepared from Co(acac)$_2$, may be explained by assuming of several contributions. Model calculations are utilised to disclose their hidden nature. Curves (b) and (c) in fig. 5.4 correspond to the spectra calculated for Co nanoparticles of different size having face centered cubic (fcc) crystal lattice and collective magnetic behaviour. Curve (b) represents a signal with large crystalline anisotropy corresponding to a relatively large particle size [Bia78] and curve (c), characterized by weak anisotropy, corresponds to rather small particles. As shown in fig. 5.5, the relative intensity of both, the measured and the calculated spectra (dashed line and filled squares), exhibit a more rapid decrease with increasing temperature than the one corresponding to Curie-like behaviour (solid line). This is characteristic for very small superparamagnetic particles [Châ85, Köh98]. From the calculated thermomagnetic data of curve (c) a particle size of 1 nm was derived which is beyond the limit of the electron microscopy visualization capability of this type of specimens. A particle size of 1.9 nm, however, was derived from temperature dependence

(dashed line in fig. 5.5) using equation (2.7) which is nearer to the 2.4 nm measured by TEM. Numerical subtraction of curve (b) plus curve (c) from the experimental spectrum (a) in fig. 5.4 yields curve (d). This difference spectrum reveals, besides a signal at $H \simeq 153$ mT ($g = 4.3$) due to ferrous impurities, a small isotropic signal at $H \simeq 315$ mT ($g = 2.18$) due to very small Co clusters [Lov71], superimposed by a low spin signal of Co^{2+}, recognizable from the hyperfine structure. Analogous to the case of Ni, the latter signal may result from cobalt ions remaining from metal complexes not reduced by aluminium hydride surface groups.
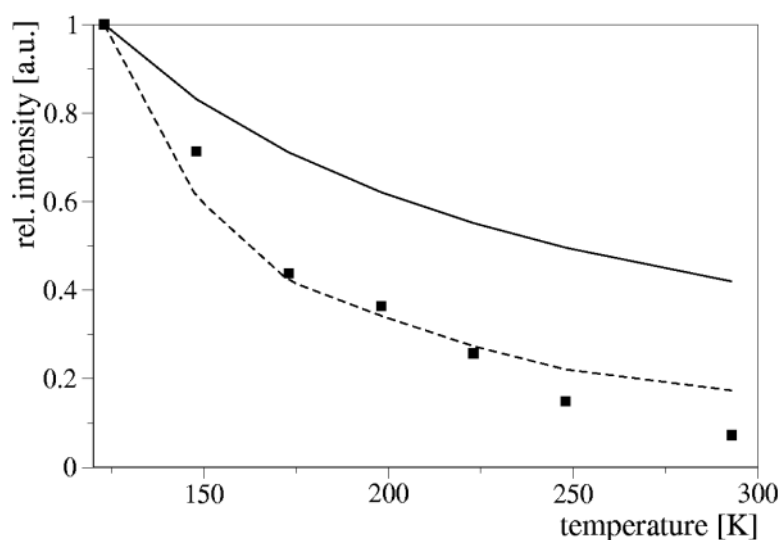
Fig. 5.5: *Temperature dependence of the relative intensity of the Co sample prepared at 100°C : measured (filled square) and calculated values (dashed line). Curie-like behaviour is shown by the solid line.*

TEM analysis of the samples prepared from $Co(acac)_2$ shows only a slight increase of particle size and coverage (14 to 15%) upon increasing the drying temperature from 100 to 300°C. A quite similar behaviour is found for Co particles originating from $CoBr_2 \cdot 2THT$ precursors, but these samples show smaller mean particle size, broader size distribution and lower coverage. With both types of Co nanoparticle samples an uniform coverage of the silica surface was achieved at both drying temperatures.

The structural characterization of Fe nanoparticles prepared by decomposition of $FeBr_2 \cdot 2THT$ on hydride-modified silica bears some complications because of the great tendency of this metal to oxidise. Even at room temperature, iron particles may react with atmospheric oxygen and water to form iron oxide layers on the particle surface. The oxide shell mainly consists of Fe_3O_4 and of some α-Fe_2O_3 [Zha96, Hof01]. Extent and composition of the iron oxide layer sensitively depends on the ambient conditions. Careful passivation procedures may protect such particles from a further oxidation [Hof01]. When measuring and comparing particle sizes one must consider that Fe oxidation proceeds by consumption of iron metal in the core which diffuses outwards to form surface oxide [Set94]. Because of the lower density of the oxide, the particle size increases distinctly upon this process. To explain the electron microscopy result of 3.3 nm mean particle size of the 100°C Fe sample in comparison to 2.3 nm of the 300°C sample, without any change in coverage (about 12%) of the substrate surface, we must assume different resistance to oxidation. Most probably, drying in vacuum is more effective for passivation at 300°C than at 100°C. There-

fore, the 100°C Fe sample is subjected to more oxidation-induced particle size increase than the 300°C sample.

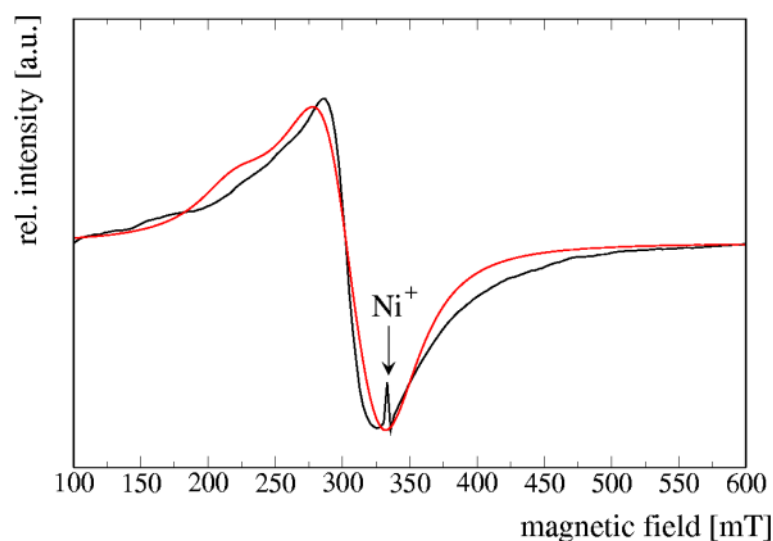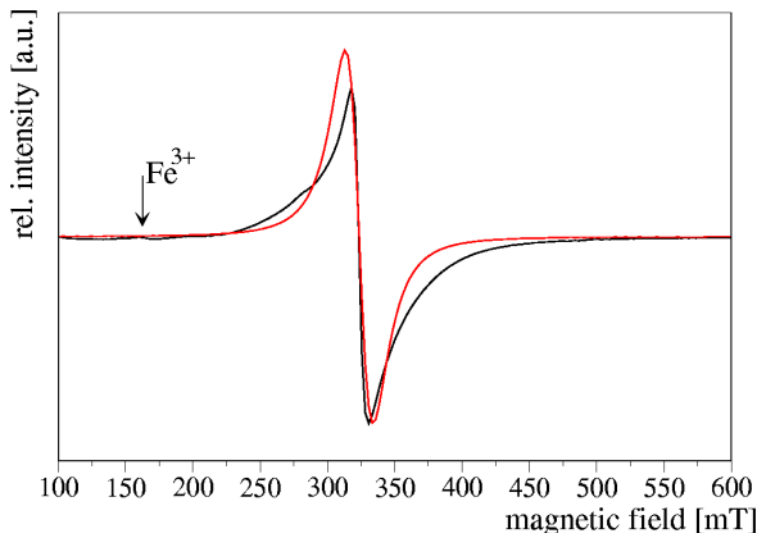***Fig. 5.6:*** *Magnetic resonance of Fe nanoparticles on silica dried at 300°C: experimental (black) and calculated curve (red).*

Both samples exhibit a signal at H $\simeq$ 161 mT ($g = 4.14$) attributed to Fe^{3+} paramagnetic species in the magnetic resonance spectra which indicates the presence of iron oxide. Fig. 5.6 shows the spectrum of the 300°C sample together with a spectrum calculated according to the Schlömann model for weak anisotropy where the best fit was obtained for $K_a = -0.0016$ and a Lorentzian line shape with $\Delta H_{pp} = 10.5$ mT. From the temperature dependence of the relative intensity, a size of 1.9 nm was derived which gives a measure of the metal core only.

5.3.2   Metal particles of the VIII B group

In addition to the superparamagnetic metal particles we also studied a number of group VIII B metal nanoparticles without collective magnetic behaviour which are expected to exhibit quantum size effects below a certain size, which is very interesting from a catalytic point of view.

Table 5.2: *Structural characteristics of group VIII B metal particles by TEM upon aging at 100°C*

Precursor	Concen. [%]	Mean size [nm]	Stand. dev. [nm]	Dispersion	Coverage [%]
$IrCl_3 \cdot 3THT$	1	1.3	0.3	0.764	15
$Ir(acac)_3$	1	1.7	0.4	0.626	16
$PdCl_2 \cdot 2THT$	2	2.7	0.9	0.449	22
$Pd(acac)_2$	1	2.1	0.4	0.520	12
$PtCl_2 \cdot 2THT$	2	2.3	0.7	0.512	14
$Pt(acac)_2$	1	1.4	0.3	0.686	11
$RhCl_3 \cdot 3THT$	2	2.3	0.5	0.516	32
$Rh(acac)_3$	1	2.5	0.5	0.473	15
$RuCl_3 \cdot 3THT$	1	2.7	0.6	0.345	11
$Ru(acac)_3$	1	1.9	0.6	0.451	14

This should give rise to conduction electron spin resonance (CESR) that may be probed by magnetic resonance measurements. From the various metals of this group, Ru, Rh, Pd, Ir and Pt were explored by utilizing both types of precursors, but here only results of the three metals formed from M(acac)$_n$ precursors are presented. They are included in Table 5.2 comprising the structural characteristics of the obtained nanoparticles.
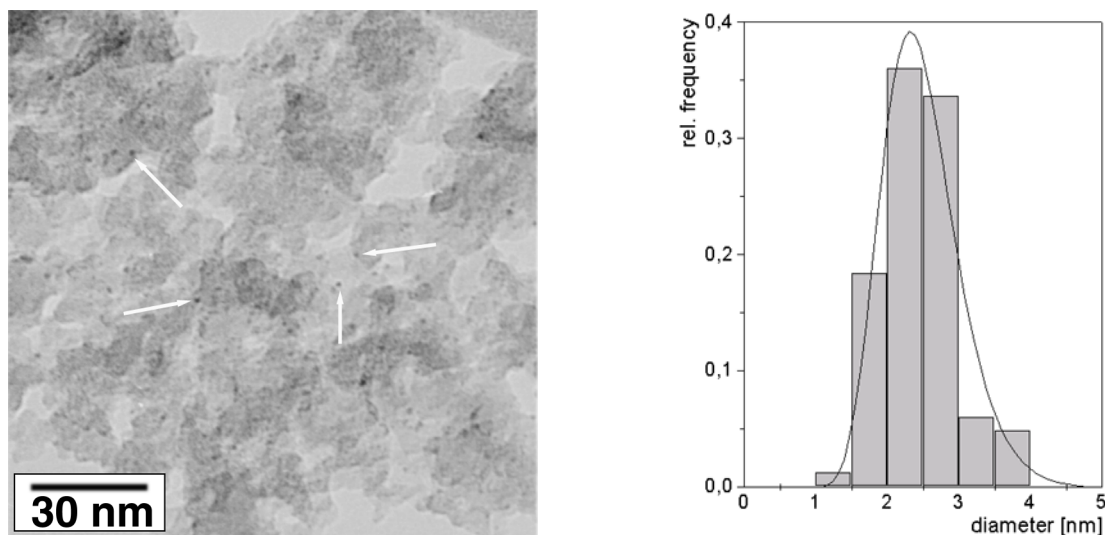
Fig. 5.7: TEM image and size distribution of Rh nanoparticles on silica dried at 100°C.

Fig. 5.7 shows a characteristic image of Rh particles on hydride-modified silica upon drying at 100°C together with the rather narrow size distribution accompanied by a Log-Normal fitting curve. In general, the particles are uniformly arranged on the oxide surface and have nearly spherical shape. From Table 5.2, one may recognize that the Rh particle size does not distinctly increase if the drying temperature is enhanced from 100 to 300°C, and also the coverage of the silica surface is only slightly raised. However, by increasing the metal loading applied during synthesis, usually a considerable enhancement of the coverage is achieved. In this context it must be noticed that in the course of electron microscopy examination occasionally metal particles are found not situated on the oxide surface, but on the supporting carbon film. This points to a certain loss of particles which, most probably, are removed from the oxide substrate because of ultrasonic agitation in solution usually applied for TEM preparation.

Magnetic resonance spectra of Rh nanoparticles on silica are subject to considerable changes with the time elapsed after preparation. This behaviour points to the presence of diffusive or even reactive species. Immediately after preparation the spectrum of the Rh sample dried at 100°C, shown in fig. 5.8 as black curve, exhibits a main signal at H$\simeq$ 295 mT, ($g = 2.28$) marked S1. This may be attributed to Rh^0 in peculiar coordination, namely a [Rh^0(acac)$_3^{3-}$] complex, since at 100°C, i.e. below its decomposition temperature, Rh(acac)$_3$ is very stable against ligand exchange [Dwy53]. Thus, there is a high probability to reduce Rh^{3+} without disturbing the coordination sphere of the complex. The transfer of the required three electrons per rhodium atom results in [Rh^0(acac)$_3^{3-}$]. However, these species are not stable, but after one month aging (see red curve in fig. 5.8) the corresponding signal has been largely replaced by two separate signals. Both
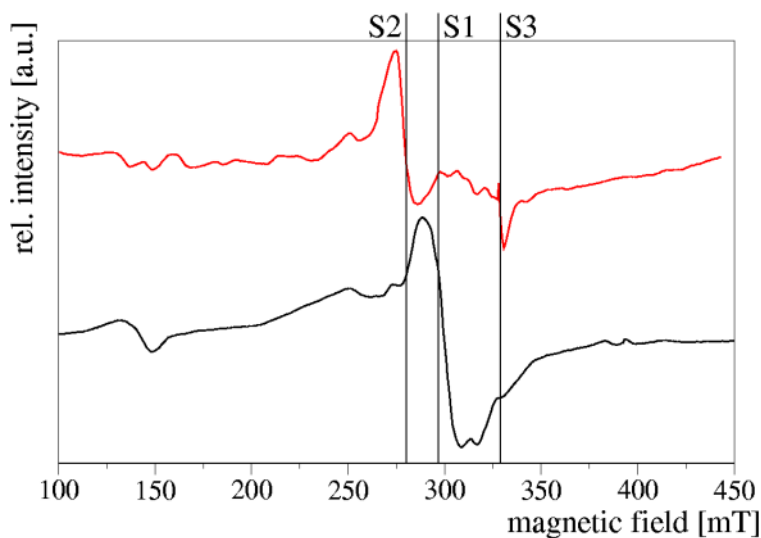
Fig. 5.8: Magnetic resonance of Rh nanoparticles on silica dried at 100° C: immediately after preparation (black), and after 1 month aging (red).

are assumed to be CESR signals of Rh particles of different size. The one, marked S2, is found at H$\simeq$ 280 mT ($g = 2.42$) and the other, marked S3, at H$\simeq$ 328 mT ($g = 2.0$). According to the second Kawabata condition (2.17), as described in Chapter 2, the maximum size of Rh particles enabling observable quantum size effect amounts to 5 nm when taking the g-shift as 0.24, i.e. the value of Pd, because the Rh value is not available in the literature. Comparing this size to the electron microscopy results, one may estimate roughly that about two third of the particles observed by TEM should contribute to CESR signals. Size calculations using equation (2.19) depending on the signal linewidth result in 0.65 nm for the S3 species and 0.8 nm for the S2 species. The first value definitely is beyond the limits of electron microscopy applied to such specimens. The deviation of the second calculated value from TEM results is mainly caused by the size distribution of Rh particles present in the sample, whereas the calculation considers only one fixed particle size. The electron microscopy investigation of these samples have been performed at least several weeks after preparation. Therefore no evolution of the particle size was recorded by this method.
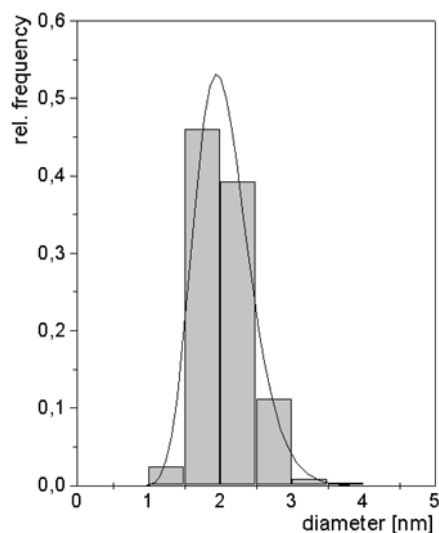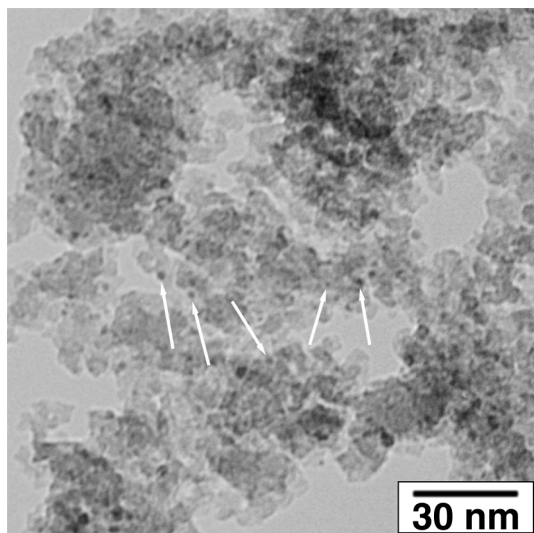
Fig. 5.9: TEM image and size distribution of Pd nanoparticles on silica dried at 300° C.

Metal deposition on hydride-modified silica by application of a Pd(acac)$_2$ precursor also yields a considerable coverage of nanoparticles of rather narrow size distribution and very uniform arrangement. A characteristic image of the Pd 300°C sample (1% metal loading) together with the corresponding size distribution is shown in fig. 5.9. There was no change of the particle size observed when increasing the drying temperature from 100 to 300°C. With 2% metal loading, however, there is not only a nearly twice as high coverage achieved, but also a distinct increase in particle size upon enhancing the drying temperature. The upper size limit of Pd nanoparticles that may exhibit quantum size effect is, according to the second Kawabata condition (2.17), calculated to be 8.5 nm. The calculated spin relaxation time and CESR signal linewidth of particles about 2 nm in size give 1.2×10^{-14} sec and 19.2 mT, respectively.

Fig. 5.10 shows a characteristic image of Pt particles resulting from Pt(acac)$_2$ precursors on hydride-modified silica upon drying at 300°C together with the narrow size distribution peaking at the mean size of 2.3 nm. This extremely small particle size does not change if instead of 100°C a drying temperature of 300°C is applied. Nevertheless, the coverage of the silica surface by Pt nanoparticles increases considerably thereupon. From these results one may conclude that, under the conditions applied, metal particle formation proceeds at high nucleation rate, but limited growth rate. This is a prerequisite for a stable particle dispersion.
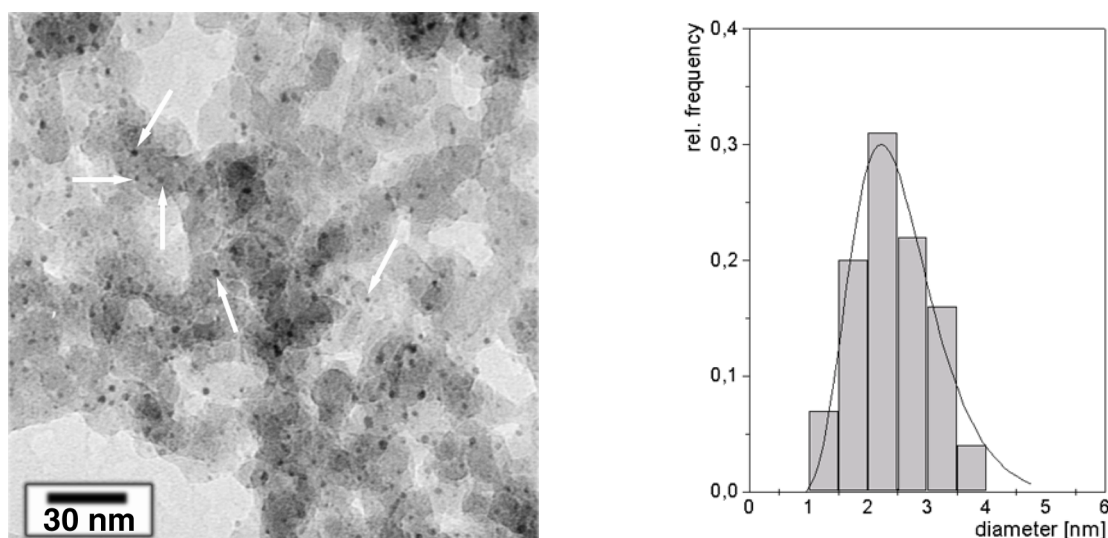
Fig. 5.10: *TEM image and size distribution of Pt nanoparticles on silica dried at 300°C.*

Using the second Kawabata condition (2.17) to calculate the upper size limit of Pt nanoparticles that exhibit quantum size effect yields 6.7 nm. Here, the CESR signal linewidth of particles of about 2 nm size is calculated to be 30 mT. With the experimental setup used for magnetic resonance measurements it is difficult to obtain reasonable spectra of such samples if the *g*-shift is too large. Thus we resort to the measurements at low temperatures. The spectrum of the 300°C Pt sample recorded at -125°C is shown in fig. 5.11 (black line) together with calculated spectra which may demonstrate how the experimental spectrum is composed of several constituents. The first one is an intense CESR signal at H $\simeq$ 292 mT, i.e. $g = 2.28$, (red curve) with $\Delta H_{pp} = 30$mT calculated for Pt particles of about 2 nm size. The second one is a CESR signal at H$\simeq$ 306 mT

Fig. 5.11: *Magnetic resonance of Pt nanoparticles on silica dried at 100°C: measured (black), calculated for 2 nm particles (red); 3 nm particles (green); E' centres (blue), and sum of calculations (magenta).*

($g = 2.2$), (green curve) with $\Delta H_{pp} = 70$ mT calculated for Pt particles of about 3 nm size. The third signal at H$\simeq$ 330 mT ($g = 2.0$) (blue curve) is calculated as paramagnetic resonance of E' centres (•Si≡) [Gri84] due to redox processes at the silica surface. Superposition of these three curve results in the sum spectrum drawn in magenta color which, besides the noise, agrees fairly well with the experimental spectrum. CESR signals also have been reported by Gordon [Gor77] for Pt/SiO$_2$ particles of 2.2 nm mean size with $g = 2.002$ and $\Delta H_{pp} = 20$mT, and by Katzer [Kat79] for Pt particles on silica with $g = 2.222$ and $\Delta H_{pp} = 70$mT. Although the results may not readily be compared to each other because of differences in measuring temperature and frequency, they nonetheless support the presented interpretation.

5.3.3 Particles of group I B metals

The deposition of group I B metal nanoparticles on oxide surfaces is of particular interest in the frame of this work because of their strong surface plasmon resonance effect in the range of visible light. Even nanoparticles of simply spherical shape of these metals are readily accessible to optical applications, e.g., by embedding in glass or other transparent media. In the current work deposition of these metals on hydride-modified silica and alumina was studied. For the sake of comparability we restrict here on the results obtained with silica which are compiled in Table 5.3.

Table 5.3: *Structural characteristics of group I B metal particles by TEM upon aging at 100°C*

Precursor	Concen. [%]	Mean size [nm]	Stand. dev. [nm]	Dispersion	Coverage [%]
Cu(acac)$_2$	1	1.3	0.3	0.764	15
AgMes$_4$	1	2.4	0.3	0.449	14
AuCl[PPh$_3$]	1	2.3	0.7	0.430	25

Fig. 5.12 shows a characteristic image of Cu particles on hydride-modified silica upon drying at 300°C together with the corresponding size distribution from which the mean particle size

is determined. Coverage and uniform arrangement of metal particles on the oxide substrate are comparable to results with the previously introduced metals.
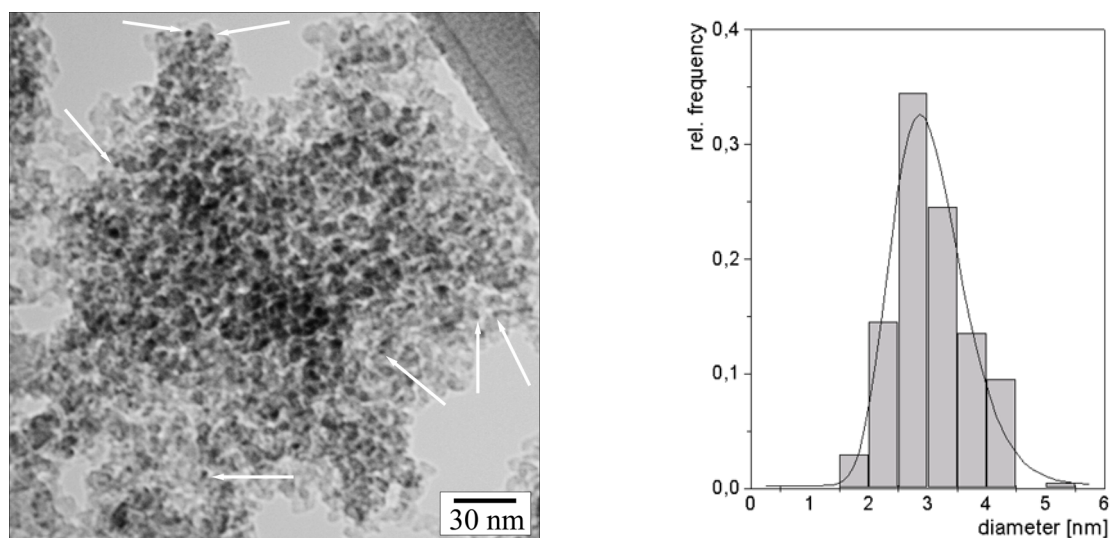
Fig. 5.12: *TEM image and size distribution of Cu nanoparticles on silica dried at 300°C.*

By applying the second Kawabata condition (2.17) a relatively large value of 14.6 nm may be calculated for the upper limit of quantum size effect in Cu particles when taking the g-shift as 0.031 [Hal86]. The spin relaxation time and CESR signal linewidth of particles about 2 nm in size may be calculated then to be 1.32×10^{-12} sec and 6.24 mT, respectively.
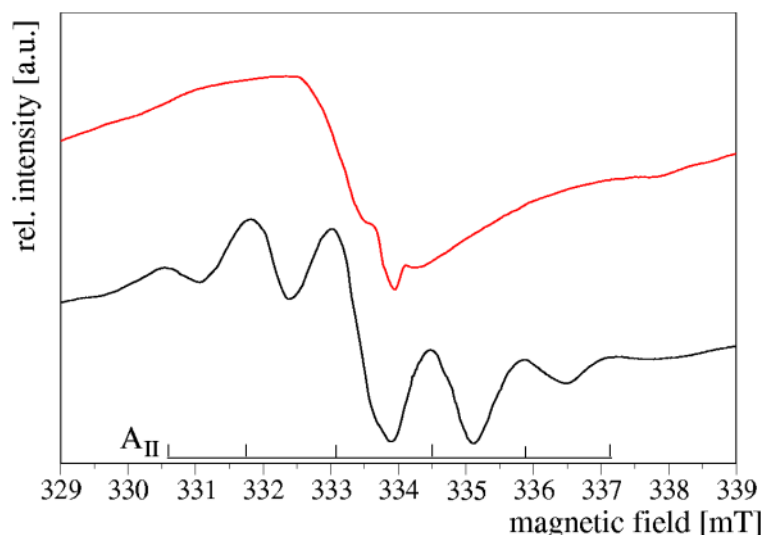
Fig. 5.13: *Magnetic resonance of Cu nanoparticles on silica dried at 100°C (black) and 300°C (red): the signals of paramagnetic Cu^{2+} species marked $A_\parallel$.*

Although the spin relaxation for Cu is two orders of magnitude lower than the above mentioned for Pd, the interpretation of the magnetic resonance spectrum is not as easy as expected because of the presence of Cu^{2+} species, the paramagnetic signal of which interferes with the CESR signal of Cu metal nanoparticles. The Cu^{2+} signal exhibits a hyperfine structure due to the interaction of unpaired electrons with the nuclear momentum of Cu nuclei (spin I=1/3) [Gon99] as may be recognized from the spectrum of the sample prepared at 100°C shown in fig. 5.13 (black line). Here the Cu^{2+} signals occur at $g_\perp = 2.002$, i.e., H = 333 mT and $g_\parallel = 2.382$ with $A_\parallel = 6.5$ mT.

If the drying temperature is increase to 300°C, fig. 5.13 (red line), the signals corresponding to Cu^{2+} decrease and the CESR signal of Cu nanoparticles is visible at H $\simeq$ 333 mT and $g = 2.0035$. Another signal, situated at H$\simeq$ 334 mT ($g = 2.003$) with $\Delta H_{pp} = 0.3$mT is assumed to be due to E' centres. Because of the very intense Cu^{2+} signals in the case of the 100°C sample and the large asymmetry of the sample prepared at 300°C assumed to be caused by some residual Cu^{2+} remaining on the substrate surface, no size of the Cu nanoparticles from corresponding CESR signals may be deduced.
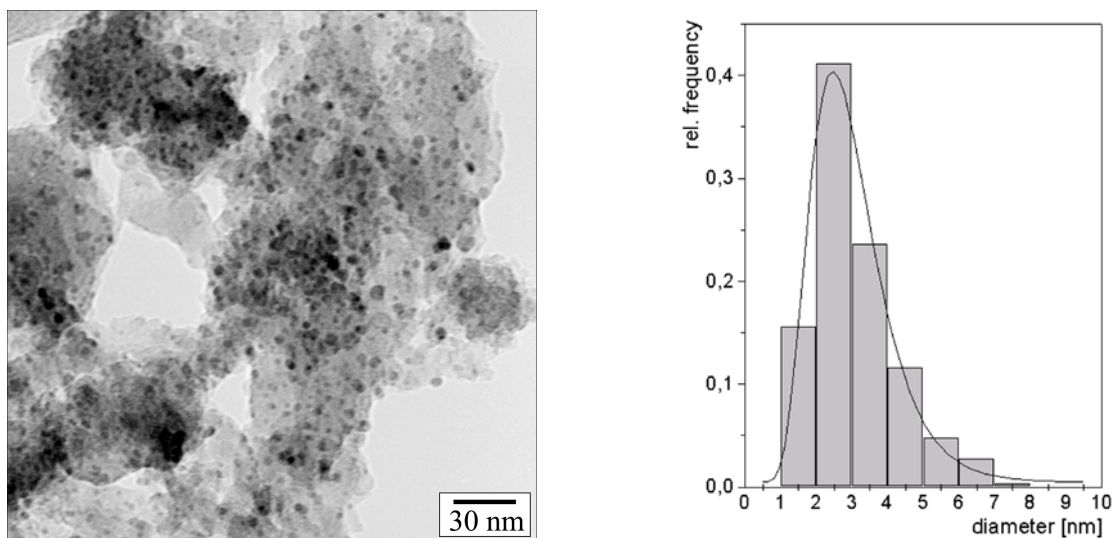
Fig. 5.14: *TEM image and size distribution of Ag nanoparticles on silica dried at 100°C.*

A characteristic image of Ag particles on hydride-modified silica upon drying at 100°C is shown in fig. 5.14 together with the corresponding size distribution fitted by a Log-Normal function. Uniform arrangement of the Ag nanoparticles and coverage of the oxide substrate are comparable to the results obtained with group VIIIB metal particles (including the superparamagnetic ones), but concerning the particle size one may recognize, that with Ag and also with Cu (see fig. 5.12), and even more with Au (see fig. 5.16 below), mean size values near 3 nm, and even above, are obtained. This raises the question of nucleation sites at which metal particle formation may occur and of the conditions determining the adhesion strength. The hydroxyl groups play an important role in this process. For a closer inspection, we studied the formation of Ag particles on hydride-modified silica which previously have been subjected to heat treatment at various temperatures between 200 and 600°C. The surface hydroxyl concentration, as measured by TGA (see Chapter 4), decreases monotonously from about 8 OH-groups/nm^2 upon 200°C heat treatment to about 1 OH-groups/nm^2 upon 600°C heat treatment. Simultaneously, the concentration of particles formed on the hydroxyl-modified and metal complex loaded oxide surface is reduced distinctly, regardless of the drying temperature applied. This loss in particle number density is accompanied by a considerable enlargement of particle size, such that nearly no change in coverage occurs. Besides studies on the optical properties of Ag nanoparticles there is also some literature about magnetic resonances observed in such materials. Mitrikas [Mit98, Mit01] studied Ag nanoparticles in sol-gel silica and found a linear relation between CESR signal linewidth and
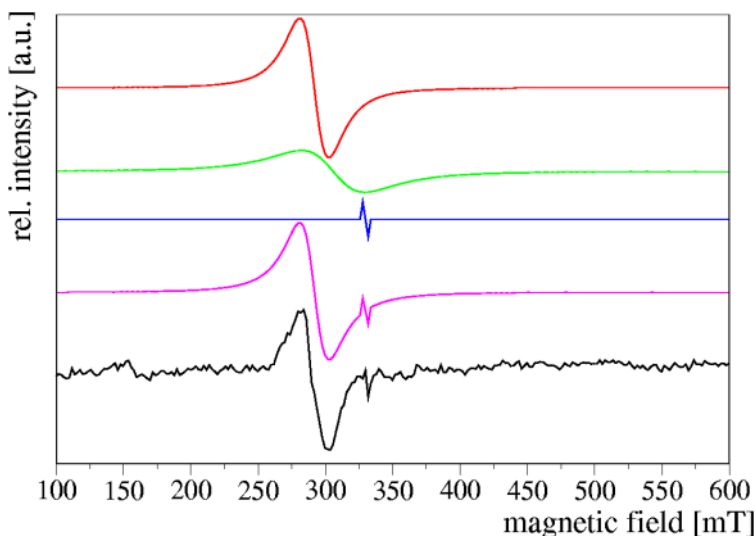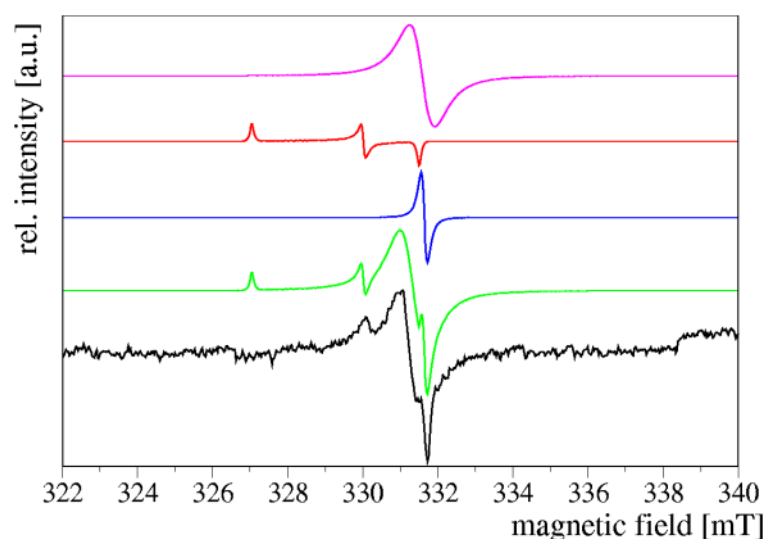
Fig. 5.15: Magnetic resonance of Ag nanoparticles on silica dried at 300°C: measured (black), calculated for 1.2 nm particles (magenta); HC_1 centres (red); E' centres (blue), and sum of calculations (green).

the square of the particle diameter (see equation (2.19)). CESR signals have been measured for colloidal Ag particles with sizes between 3 and 30 nm by Jain [Jai75] who found narrow signals of 1 to 1.14 mT linewidth at $g = 2.034$ (measuring temperature: $-180°C$). A similar line position was reported by Li [Li95] for well-dispersed Ag particles of comparable size on SiO_2, but with even narrower linewidth of 0.15 to 0.6 mT. Our measurements, performed at room temperature yielded complicated spectra composed of an Ag CESR signal plus additional constituents as may be seen in fig. 5.15 for the 300°C sample (black curve). A CESR signal at H = 331.6 mT (g = 2.031) with $\Delta H_{pp} = 0.7$mT (magenta curve) is calculated for Ag particles of 1.2 nm size taking into accout a g-shift of -0.019 [Hal86, Mit98], quite comparable to the results described in the literature. To account for the presence of defects on the silica surface, an asymmetric signal was calculated for HC_1 centres ($\equiv$Si-O•) [Gri84] (red curve) and another one for E' centres [Gri84] (blue curve). Superposition of these constituents gives the sum spectrum (green curve) that agrees fairly well with the main characteristics of the measured spectrum.
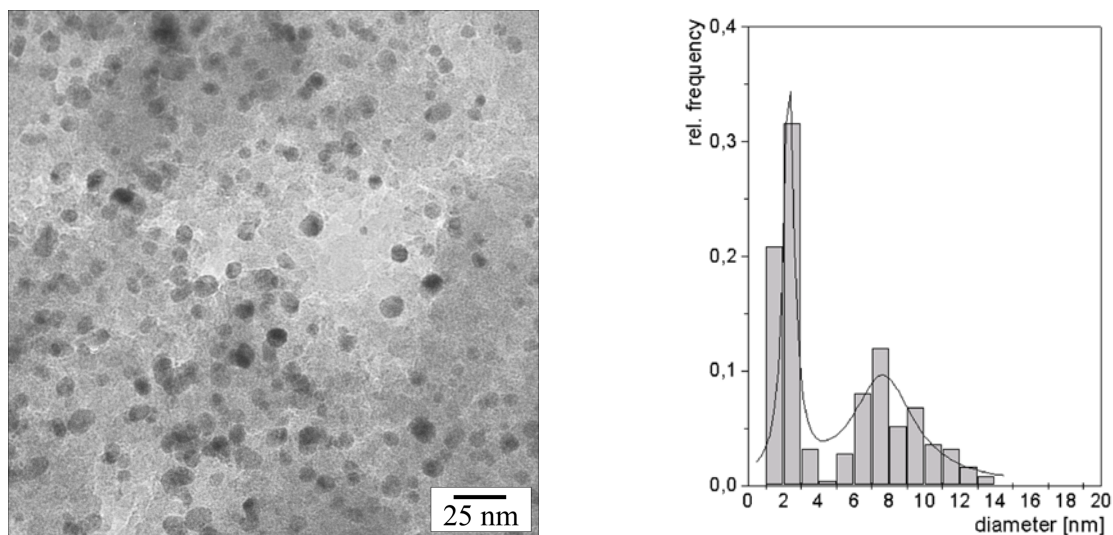
Fig. 5.16: TEM image and size distribution of Au nanoparticles on silica dried at 100°C.

Finally the results obtained with deposition of gold, the third group I B metal, on hydride-modified silica shall be presented. As it is demonstrated in fig. 5.16, showing a characteristic TEM image and the corresponding size distribution for the $100°C$ sample, the oxide surface is uniformly covered by metal particles which exhibit a bimodal size distribution. The shape of these size distributions could most correctly be fitted by using a function of Log-Normal type for the first peak and a Gaussian for the second peak. This bimodality is also found when applying 200 and 300 instead of $100°C$ drying temperature. The first maximum of the distribution increases
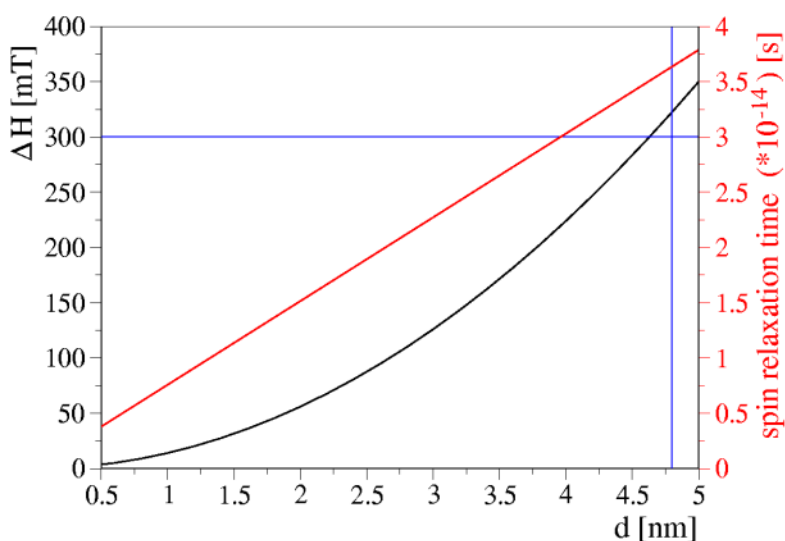
Fig. 5.17: Calculated linewidth (black) and spin relaxation time (red) of Au nanoparticles. The particle size limit according to (2.17) Kawabata condition is indicated by a vertical, and the limitation of the spetrometer by a horizontal blue line.

only slightly from 2.3 to 2.5 nm upon temperature enhancement, whereas the second maximum increases distinctly from 7.6 to 9.0 nm which is accompanied by a certain broadening. Nevertheless, the coverage of the oxide surfaces by gold nanoparticles remains nearly constant at the high value of about 23%. However, because of an increased tendency to form agglomerates of particles at higher drying temperature the uniform arrangement of particles is affected this way.

The linewidth of CESR signals for Au particles (black curve) and the corresponding spin relaxation time (red curve) were calculated in the frame of the Kawabata theory as function of their size and are drawn in fig. 5.17. The vertical blue line in this graph indicates the particle size limit of 4.8 nm for quantum size effect of Au according to the second Kawabata condition (2.17), and the horizontal line in blue color indicates the experimental limitation due to the spectrometer. From this representation one may conclude that the particles corresponding to the second peak of the particle size distribution do not contribute to a CESR signal. In the literature there was given some evidence by Monot [Mon71] and Claus [Cla00] of a CESR signal at $g = 2.0053$ resulting from Au particles. These spectra, however, have been measured at low temperatures, while in our room temperature measurement no such signal was observed.

Short review of results

As summary of the experimental exploration of coating characteristics for transition metal nanoparticles on non-planar oxide substrates, here the main results are compiled in brief. By heat-assisted

reduction of a variety of metal complexes, applied by impregnation from solution, on hydride-modified oxides generally very small particles are formed. Mean sizes around 2 nm are mostly achieved at appropriate precursor concentration and drying temperature. Samples coated with Ni, Co, or Fe nanoparticles showed ferromagnetic rersonance as signature of collective magnetic modes of small spherical particles. These results may be of interest when studying variations of such modes upon particle arrangement in core-shell-geometry. Within a number of paramagnetic group VIIIB metal particles which are of interest also because of potential catalytic utilization, Pt and Rh nanoparticles showed CESR signals in their magnetic resonance spectra, characteristic of quantum size effect. Besides the signals resulting from metal particles, in these spectra frequently indications of paramagnetic species like metal ions and oxide structure defects are observed. These findings point to aging-dependent incomplete reduction or re-oxidation processes which largely disappear upon drying at a little higher temperature. In connection with the observation of increasing mean particle sizes for group IB nanoparticles of Cu, Ag, and Au it may be concluded that the ratio of growth rate to nucleation rate increases with increasing particle size and decreasing reactivity of the metal. Residual surface hydroxyl groups are found to play an important role in the immobilisation of particles.

6 Core-shell-like structures by metal nanoparticles coatings on oxide nanospheres

6.1 Metal deposition from organometallic precursors

As it was demonstrated in Chapter 5, deposition of a number of transition metals on hydride - modified non-planar oxide materials yields reasonable results with respect to uniform particle arrangement, small particle size and initial coverage of the oxide surface. However, there was a limitation in achieving better control of the decomposition under moderate temperature conditions of the precursor molecules, and there was, due to the applied hydride modification of the oxide surface, a contamination by ill-defined alumino-silicate groups. Alternatively, a synthesis of metal nanoparticles utilizing the decomposition of low valent organometallic precursors by low temperature thermolysis of appropriate thermally unstable compounds is recommended [deC95]. The moderate conditions of synthesis are aimed at providing better control of metal deposition on oxide nanospheres.

We explored organometallic complexes of the type $[Li(THF)_2]_2 \cdot [MR_4]$ with "M" being Pt or Pd and "R" being methyl $\{[CH_3]\}$ or phenyl $\{[C_6H_5]\}$ ligands, respectively. The precursors have been synthesized under air-sealed conditions according to Wyrwa and Drevs [Wyr99, Dre02]. Prior to employment of the metal precursors the oxide materials used were subjected to a heat treatment in vacuum at 200°C to achieve controlled hydroxyl content on the surface. All organometallic metal depositions were carried out by Prof. H. Drevs (Merseburg). After cooling down to room temperature a suspension of the oxide was prepared under argon atmosphere in a solution of THF containing the required quantity of the organometallic complex. The metal deposition proceeded according to:

$$2 \equiv Si - OH + [Li(THF)_2]_2 \cdot [MR_4] \longrightarrow (\equiv Si - OLi)_2 M^0 + 2HR + R_2$$
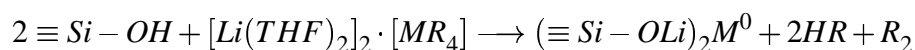
whereupon heating to 100 or 300°C for 1 h was applied to induce metal particle formation and to remove organic residuals. Even when not exceeding room temperature, the formation of metal

particles on the surface of silica nanospheres was observed. This behaviour is assumed to result from the formation of organometallic surface complexes of the type

$$[\equiv Si - O - MR_2 - O - Si \equiv] \cdot 2Li^+$$
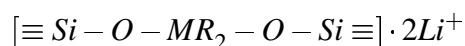
as intermediates in the process of metal precursor decomposition induced by reaction with surface hydroxyl groups. For comparison with the route of metal deposition utilizing hydride-modified oxide surfaces (see Chapter 5) the organometallic Pt phenyl complex was first applied to non-planar oxide materials.

Deposition of Pt nanoparticles from the Pt phenyl complex lithiumtetraphenylplatinate(II) was tried on silica and alumina surfaces. As in Chapter 5.3.3, here we restrict ourselves to the results obtained with silica samples. They are presented in Table 6.1 comprising the structural characteristics of the Pt nanoparticles obtained. Fig. 6.1 shows a characteristic image of Pt particles on silica upon drying at 300°C together with the narrow size distribution fitted by a Log-Normal function (see black curve). The particles are uniformly arranged on the oxide surface and have nearly spherical shape, as it was observed also on hydride-modified oxide surfaces. Remarkably, there is nearly no change in mean particle size and coverage of the silica surface when increasing the drying temperature from 100 to 300°C. For comparable metal concentrations applied the organometallic route yields similar particles sizes with that obtained from Pt(acac)$_2$ presursor deposited on hydride-modified silica (see Chapter 5.3.2).

Table 6.1: *Characteristics of Pt nanoparticles (organometallic route) on silica by TEM*

Concen. [%]	Temp. [°C]	Mean size [nm]	Stand. dev. [nm]	Coverage [%]
2	100	2.1	0.5	32
2	300	2.0	0.4	34
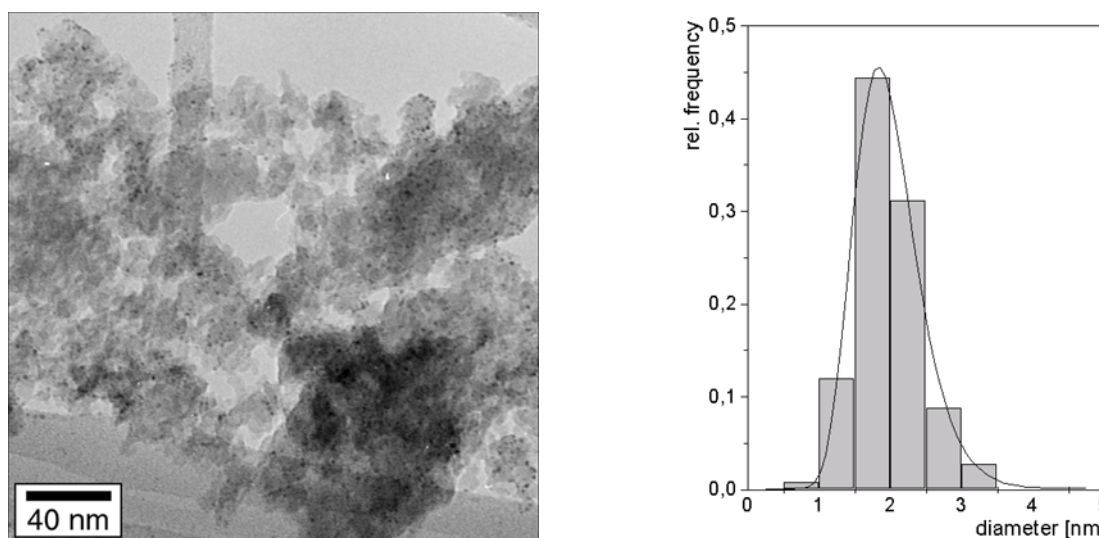
Fig. 6.1: *TEM image and size distribution of Pt nanoparticles (organometallic route) on silica dried at 300°C.*

The magnetic resonance spectra of Pt nanoparticles on silica prepared via the organometallic route undergo certain changes with time after preparation. Fig. 6.2 shows the spectrum of the 300°C sample measured 6 months after preparation (black curve) together with two calculated spectra and their superposition (red curve) set to model the experimental spectrum. The first is an intense signal (blue curve) at H $\simeq$ 293 mT, corresponding to g = 2.28, with ΔH_{pp} = 13 mT, which is belived to result from Pt^+ ions as it was observed also by Claus [Cla97] for Pt deposition on titania. The other is a very broad CESR signal (green curve) at H $\simeq$ 152 mT with g = 4.36 and ΔH_{pp} = 130 mT that is attributed to Pt particles of about 4.2 nm size according to the Kawabata theory. CESR signals for Pt particles of such sizes have not been reported in the literature up to now. However, the unusual large g-shift of 2.2, as compared to the bulk value, occuring for this signal needs further explanation. The distinct signal indicating the presence of Pt^+ ions raises the question of their origin. A possible explanation is the re-oxidation of atomically dispersed Pt^0 at remaining surface hydroxyl groups [Dre98]. Such ions may attract metal atoms and serve this way as preferred sites for the formation of nanoparticles. As may be concluded from the aging behaviour of the magnetic resonance spectra, the concentration of Pt^+ ions as well as the size of Pt particles are subject to changes in the course of these long-time processes.
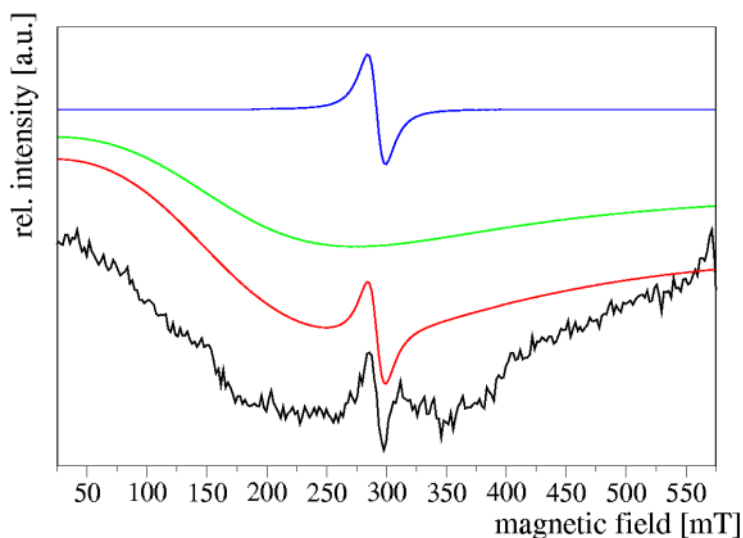
Fig. 6.2: *Magnetic resonance spectra of Pt nanoparticles (organometallic route) on silica dried at 300 °C: experimental (black), calculated for Pt^+ ions (blue); for 4.2 nm particles (green); and sum of calculated spectra (red).*

6.2 Characterisation of metal particles on polydisperse oxide nanospheres

The first attempts to achieve core-shell structures with oxide nanospheres coated by metal nanoparticles have been carried out with polydisperse nanospheres of silica and titania which are commercially available. Although such materials usually exhibit a rather broad size distribution, they do have a number of decisive advantages:

Table 6.2: *Characteristics of Pt and Pd nanoparticles on* NANOTEK *silica by TEM*

Precursor	Concen. [%]	Temp [°C]	Mean size [nm]	Stand. dev. [nm]	Coverage [%]
$Li_2[Pt(Ph)_4]\cdot4THF$	0.5	100	2.2	0.5	12
$Li_2[Pt(Ph)_4]\cdot4THF$	0.5	300	2.5	0.6	16
$Li_2[Pt(CH_3)_4]\cdot4THF$	2.6	20	2.9	0.6	36
$Li_2[Pd(Ph)_4]\cdot4THF$	2	20	2.6	0.6	30

(i) the spherical shape is just the geometry required, *(ii)* the smooth surface is a prerequisite for uniform coverage, *(iii)* there is a sufficient high number of oxide spheres in a size range appropriate for structural characterization.

On silica nanospheres of NANOTEK (for details see Chapter 4.2) we employed organometallic complexes of Pt and Pd in a variety of preparation conditions which are comprised together with results of the structural characterisation by TEM in Table 6.2. From the experiment with a very low concentration of the Pt phenyl complex, fig. 6.3 shows the sample dried at 300°C that exhibits a slight increase in mean particle size and coverage as compared to the 100°C sample. No agglomeration of particles to form larger aggregates is observed. As may be recognized from
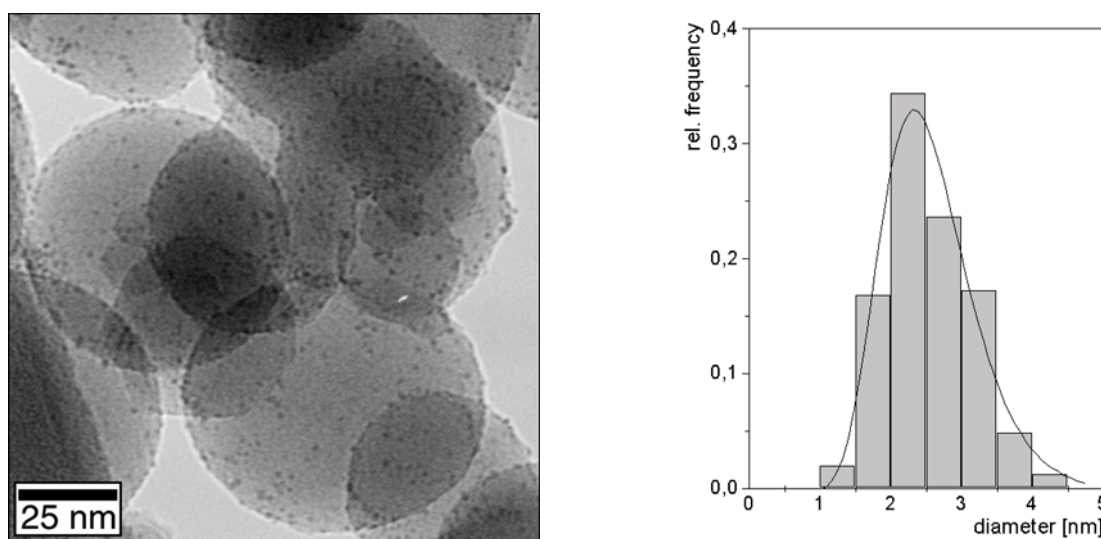
Fig. 6.3: *TEM image and size distribution of Pt (0.5%) nanoparticles on* NANOTEK *silica upon drying at 300°C.*

the above figure, regardless of size the silica nanospheres carry an uniform arrangement of metal particles, the narrow size distribution of which is expected to favour further metal deposition by complementary processes.

The magnetic resonance spectra of these samples are presented in fig. 6.4 where the red curve corresponds to the 100°C and the black curve to the 300°C sample, respectively. Both spectra exhibit CESR signals as a signature of large particles. The 100°C spectrum contains a broad signal at H = 320.1 mT, corresponding to g = 2.158, with $\Delta H_{pp} = 75.75$ mT which is superimposed by a signal at H = 325 mT, i.e. g = 2.02 resulting from Pt^+ ions [Bon88, Cla97]. From the CESR signal a Pt particle size of 3.2 nm may be derived using the Kawabata theory. In the spectrum of the 300°C sample the Pt^+ signal is missing and only a CESR signal at H = 275 mT, corresponding
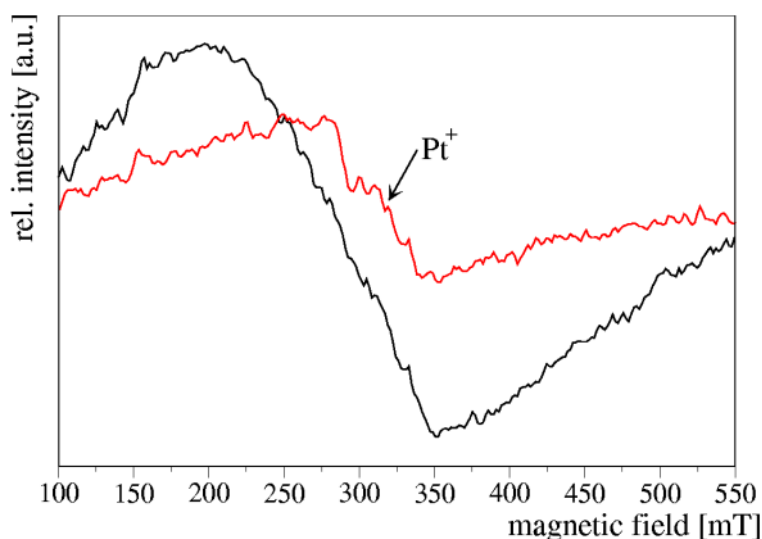
Fig. 6.4: *Magnetic resonance spectra of Pt (0.5%) nanoparticles on NANOTEK silica: dried at 100°C (red); at 300°C (black).*

to g = 2.342, with $\Delta H_{pp} = 150$ mT is present, from which a Pt particle size of 4.5 nm, close to the result of TEM examination, is calculated. Since these spectra have been recorded at room temperature, they are the first that give evidence of quantum size effect of Pt particles under such conditions.

In addition to the low concentration experiments we explored the efficiency of employing organometallic complexes in high concentration, but without applying elevated temperatures during vacuum drying for several hours. As an example of the experiment with 2.6% of the Pt methyl complex, fig. 6.5 shows a characteristic HREM image and the corresponding size distribution. It should be pointed out here that decomposition of the precursor complex and formation of Pt
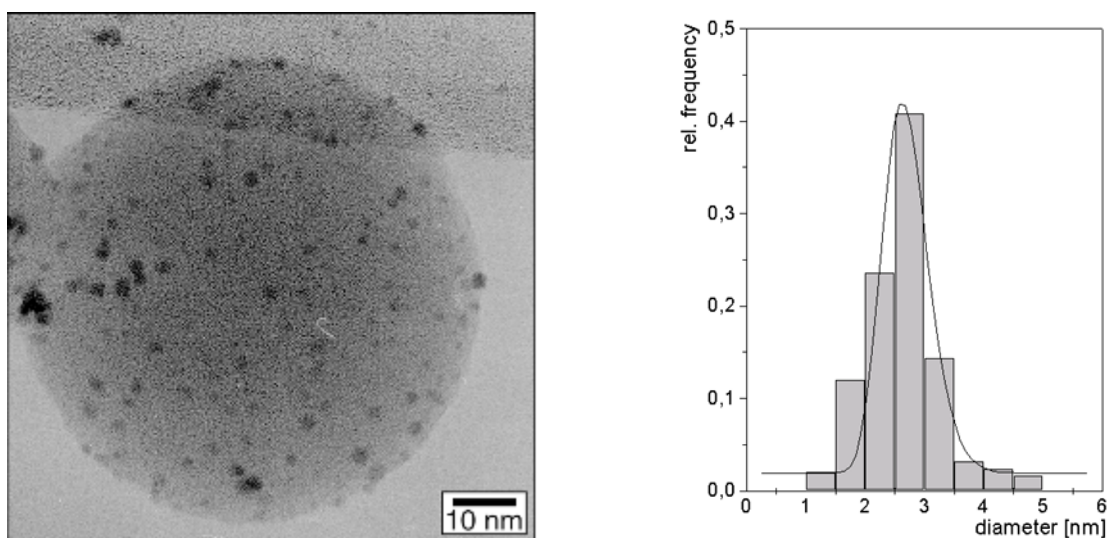
Fig. 6.5: *HREM image and size distribution of Pt nanoparticles on NANOTEK silica prepared from the Pt methyl complex without heating.*

nanoparticles of 2.9 nm mean size were achieved without reducing agents in the solution or reducing gases like H_2 or CO in the ambient. Because of the relative high precursor loading a high coverage of the silica surface by Pt particles results which occasionally form aggregates. This points to the fact that without heat treatment or ligand-mediated anchoring the adhesion strength of

metal particles on the oxide surface is rather low. A similar behaviour is found for the low temperature experiment with the Pd phenyl complex. As can be seen from fig. 6.6, where a characteristic TEM image and the corresponding size distribution is shown, there are Pd particles situated not only on the silica nanospheres, but also on the supporting carbon film. This kind of particle loss is supposed to happen during preparation for TEM when the coated silica nanospheres are dispersed and agitated in organic solvent. Metal particles removed from the silica may stick on the carbon upon solvent evaporation. Again, it should be emphasized that also with Pd and with the phenyl complex of this metal the low temperature route to nanoparticles is tested quite succesfully.
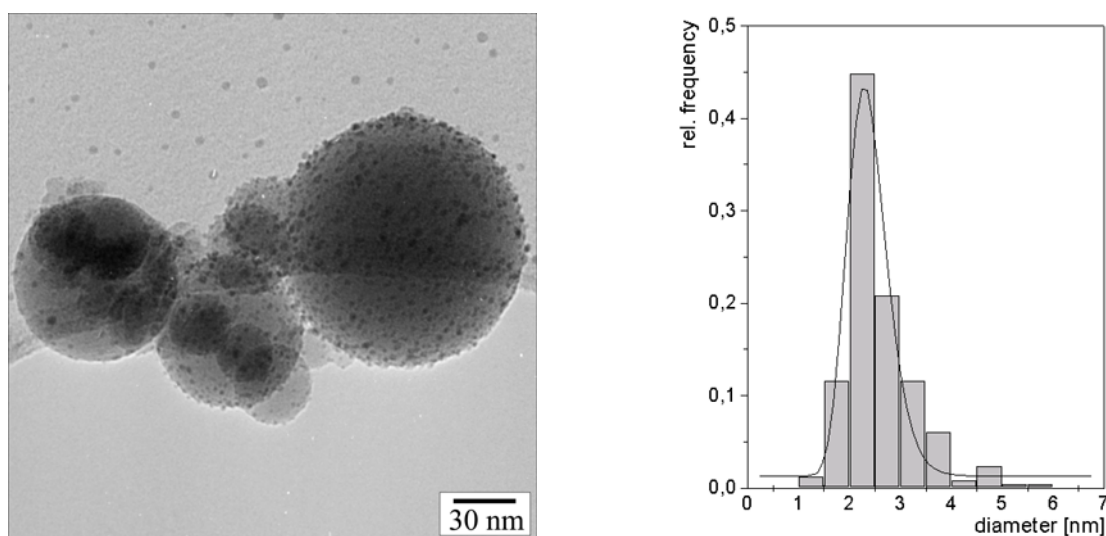
Fig. 6.6: *TEM image and size distribution of Pd nanoparticles on NANOTEK silica prepared from the Pd phenyl complex without heating.*

Metal nanoparticle coating via the organometallic precursor route was also explored on titania nanospheres. With this oxide, the reactivity of hydroxyl groups as well as the strength of interaction between metal deposit and oxide substrate is expected to change compared with silica. Another difference comes from the atomic structure of the oxides: while silica has amorphous structure without long-range order, titania has a crystalline structure and may be present in two different modifications (anatase and rutile).

Table 6.3: *Characteristics of Pt and Pd nanoparticles on CERAC titania by TEM*

Precursor	Concen. [%]	Temp [°C]	Mean size [nm]	Stand. dev. [nm]	Coverage [%]
$Li_2[Pt(Ph)_4]\cdot 4THF$	2	100	2.4	0.6	28
$Li_2[Pt(Ph)_4]\cdot 4THF$	2	300	2.8	0.8	32
$Li_2[Pt(CH_3)_4]\cdot 4THF$	2	100	2.5	0.7	30
$Li_2[Pt(CH_3)_4]\cdot 4THF$	2	300	2.7	0.7	34
$Li_2[Pd(Ph)_4]\cdot 4THF$	1	100	1.9	0.4	28
$Li_2[Pd(Ph)_4]\cdot 4THF$	1	300	2.3	0.6	30

On titania nanospheres of CERAC (for details see Chapter 4.2) we employed organometallic complexes of Pt and Pd in a variety of preparation conditions which are comprised together with results of the structural characterisation by TEM in Table 6.3.

Not included in this table are experiments carried out at room temperature and 60°C since they failed to produce to some extent uniformly arranged metal particles. Obviously it needs elevated temperatures to achieve a reasonable adhesion of metal particle on titania. Magnetic resonance measurements at these samples did not reveal some signature of metal nanoparticles because of the strong signals of Ti^{3+} ions dominating the spectra.

With the 100°C and 300°C samples of the Pt phenyl complex on titania there is not much difference compared to silica, except for the larger coverage being due to the higher concentration applied on titania. From the experiment with the Pt methyl complex on titania, fig. 6.7 shows a characteristic TEM image and the corresponding size distribution of the sample dried at 300°C. Different from the narrow size distribution observed with this precursor on silica, here Pt nanopar-
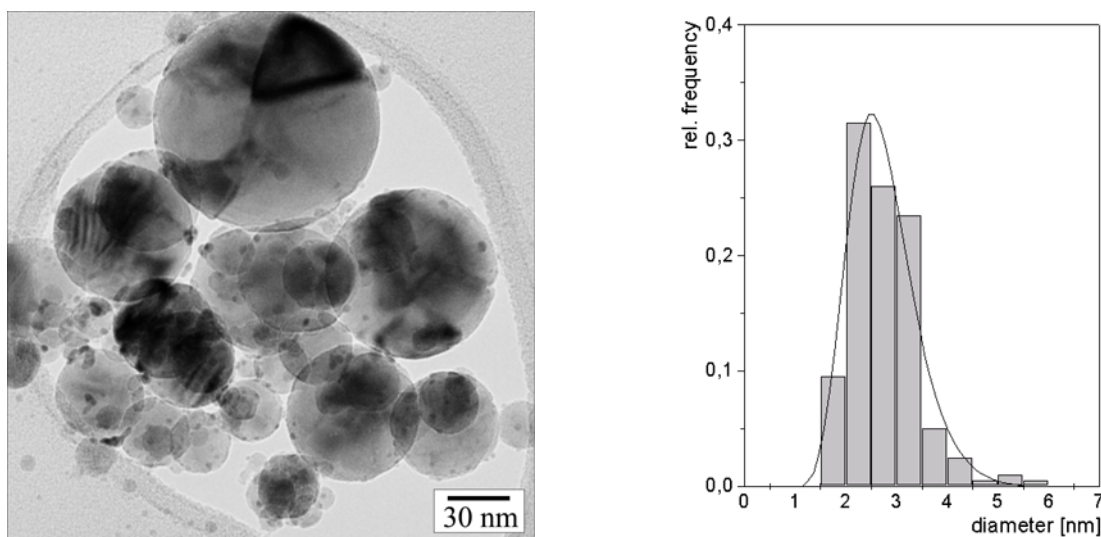
Fig. 6.7: *TEM image and size distribution of Pt nanoparticles on* CERAC *titania prepared from the Pt methyl complex upon drying at 300°C.*

ticles are found in a broader range of sizes. From this TEM image and also from the one shown in fig. 6.8 of Pd nanoparticles on titania prepared from the Pd phenyl complex (300°C sample) it may be recognized how much the visualization of metal particles is deteriorated because of the crystalline nature of the titania nanospheres. Lattice defects, present in high number density, cause image contrast features owing to diffraction effects which readily may hide the image contrast of metal particles. The crystalline nature of titania is also responsible for surface inhomogeneities which lead to a less uniform coverage by metal particles as on silica. Although the CERAC titania nanospheres exhibit rather good spherical appearance, surface inhomogeneities like steps and facets of various type cannot be entirely avoided with crystalline material.

From the results presented above it may be concluded that the route of synthesis via decomposition of organometallic complexes is well suited as prenucleation step at which subsequent steps of metal deposition by complementary processes may follow to achieve regular arrangement and dense coverage of metal nanoparticles on oxide nanospheres for creating core-shell structures which have novel optical properties. In this respect it is advantageous to employ the organometallic precursors at not too high concentration. Even if the explored procedures obviously work better
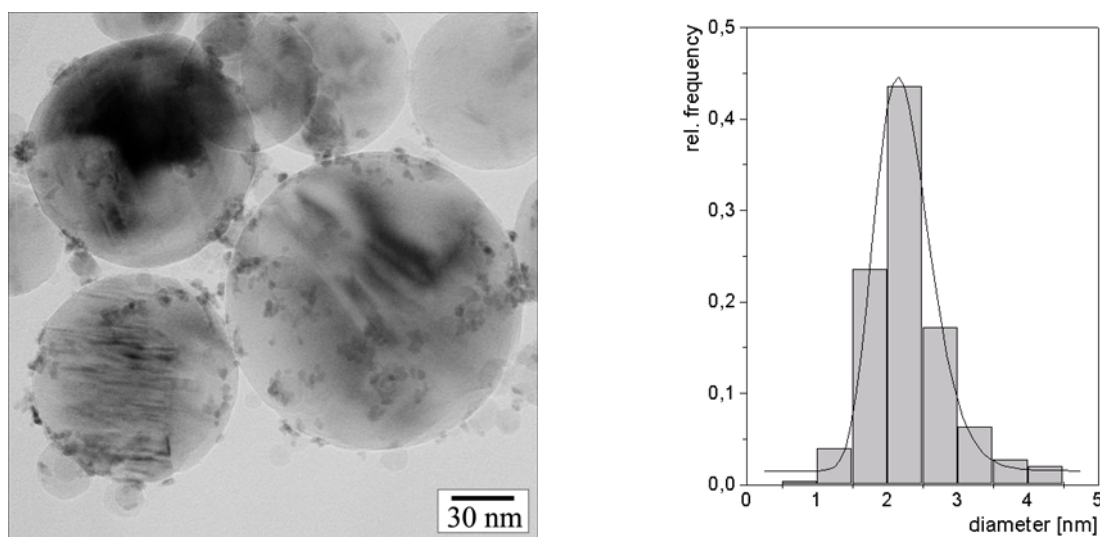
Fig. 6.8: *TEM image and size distribution of Pd nanoparticles on* CERAC *titania prepared from the Pd phenyl complex upon drying at 300° C.*

with silica than with titania, the latter oxide remains an interesting candidate for studying optical effects since it exhibits considerably strong interface effects (peak shift, resonance damping), e.g. with Ag nanoparticles [Kre97b]. On the other hand, the imaginary component of the titania dielectric function may cause some complications with the manipulation and design of optical properties.

6.3   Metal deposition by incipient wetness impregnation

A decisive step on the way to fabricate core-shell structures of oxide nanospheres coated by metal nanoparticles was the employment of monodisperse silica spheres prepared by the Stöber method [Stö68]. With the availability of these starting materials a better defined exploration of appropriate coating conditions was possible. Accordingly, the investigations have been directed to the metals which exhibit strong surface plasmon resonance effects like Ag and Au. For these metals, however, no organometallic complexe that may be used in the above (Chapters 6.1 and 6.2) described route was readily available. Therefore, another route of synthesis was needed that could meet the already described requirements, namely the production of spectroscopically clear (no adhesives!) and photochemically stable (no ligands!) metal nanoparticle deposits. To this aim, the incipient wetness impregnation method, requiring only modest chemical laboratory technique and commercially available chemicals, was successfully applied.

This method, widely used for the preparation of heterogeneous catalysts, consists of wetting a non-planar (powder) substrate by a metal salt solution of certain concentration so as to cover its surface in a defined manner. In catalyst preparation, after drying the impregnated carrier powder, usually a calcination treatment, e.g., in flowing air, is performed resulting in a transformation of the deposited metal salt into an oxide or hydroxide of the metal, that may be reduced, e.g., in flowing hydrogen, in a subsequent reduction step. Since calcination and reduction are usually carried out in

a temperature range of about 300 to 800°C, these procedures are not useful for the purpose of metal particle formation under moderate conditions. Instead, we tested if the formation of metal particles could be achieved by simply drying the impregnated silica nanospheres at temperatures below 100°C or even at room temperature, similar to what has been obtained with the organometallic precursors (see Chapter 6.2). This treatment proved to be successful. The whole procedure is schematically represented in fig. 6.9 where the left part illustrates the impregnation step, the center shows the situation after solvent removal, and the right that upon metal particle formation. The latter step is considered to be sensitively depending on the configuration of terminating groups on the silica surface, since such surface groups obviously provide the reducing radicals required for the reduction of metal ions. Terminating OH- groups usually formed on the oxide surface by dissociative adsorption of water molecules can acquire such properties, depending on their coordination symmetry [Sab00, Zak01]. Accordingly, metal ion reduction could proceed via the reaction

$$\equiv Si - OH + M^0 \longleftrightarrow \equiv Si - O \bullet + H^+ + M^0$$
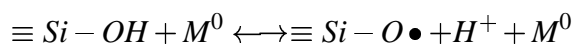
while with $\equiv Si - O^-$ groups formed by dissociation of hydrogen from the surface hydroxyl the following reaction is possible

$$2 \equiv Si - O^- + 2M^+ \longleftrightarrow \equiv Si - O - Si \equiv + 2M^0 + \frac{1}{2}O_2 \uparrow$$
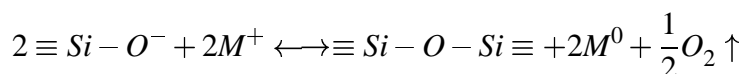
The efficiency of these surface-mediated reduction processes is observed to vary with aging of the silica nanospheres.
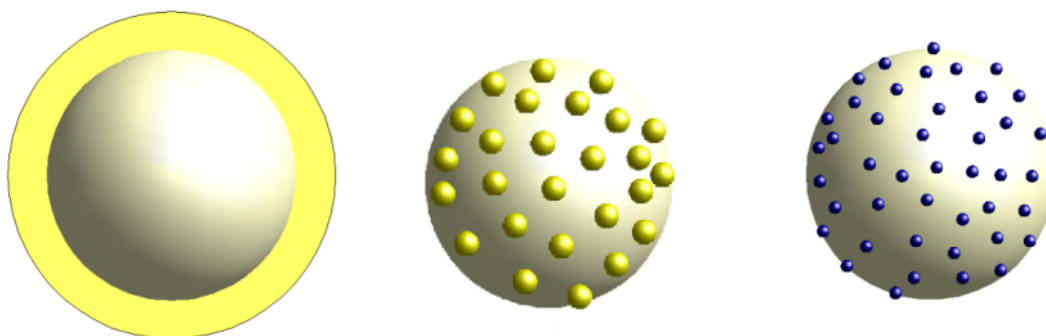
Fig. 6.9: Metal nanoparticle formation on silica nanospheres by incipient wetness impregnation (left) and (center), followed by metal precursor decomposition upon drying at moderate temperatures (right).

Besides temperature and initial concentration of the precursor complex, there is not much scope for controlling nucleation and growth processes in the practical execution of this route of synthesis. The aim of producing core-shell-like structures requires to achieve a high nucleation rate, but low growth rate, so as to obtain a high number density of metal nanoparticles without formation of aggregates. Therefore, we followed the concept of first forming a seeding layer of metal particles on the silica nanosphere surface by applying low precursor concentrations in a one- or two-step prenucleation procedure. Further nanoparticle coating from complementary processes is needed

then to form continuous metal nanoshells. Such multi-step processing includes some prospects of fabricating bimetallic structures by varying the precursor complex employed. This is represented schematically in fig. 6.10 where the left part illustrates the second impregnation step, the center shows metal nanoparticles and metal salt specks covering the silica nanosphere simultaneously, and the right part indicates particle formation of several metals. For the sake of clarity, different metals are shown separately in this figure and marked by different colors, implying no interaction of the involved metals. However, there is some indication given in the literature that the metal particles formed in a prenucleation step may serve as seeds which catalyze metal deposition via complementary processes without nucleation of new particles [Bro00, Jan01, Sau01].
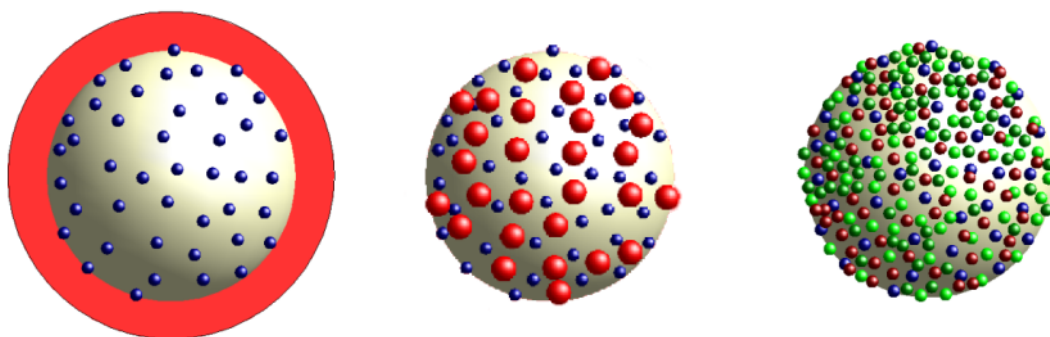
Fig. 6.10: *Multi-step metal nanoparticle formation on silica with applying another metal in the second impregnation step (left) and (center), followed by formation of the second type of metal particles (right).*

The above described metal deposition processes have been applied to monodisperse silica nanospheres, received from MERCK (Monospher^{TM}) with 100 and 250 nm nominal size or laboratory-made by the Stöber method (see Chapter 4.3), with sizes in the range of 100 to 300 nm. As metal precursors the water-soluble complexes hydrogentetrachloroaurate $HAuCl_4$ and silvernitrate $AgNO_3$ obtained from ALFA as well as silver acetate $AgOOCCH_3$ from FLUKA have been employed. Silica nanospheres and metal complexes were used without further pretreatment. For a certain, precisely measured mass of the oxide, typically 2 g, the mass of metal salt is calculated that is required to achieve a certain metal concentration. This quantity of the metal complex is dissolved in a defined volume of distilled water required to meet the condition of incipient wetness. The solution is added then to the oxide powder and stirred until a uniform color of the sample was observed. Before any further treatment they were stored at room temperature in air for 2 hours. For thermal decomposition of the metal complexes the samples were filled in quartz boats and placed in a quartz tube of 20 mm diameter inside a temperature controlled cylindrical oven. This quartz tube could be evacuated by a membrane pump to a vacuum of about 20 mbar. Since the metal precursors applied are sensitive even to visible light, the above procedure was carried out under dark-room conditions. However, some samples have been subjected to illumination with UV light of a two-range UV lamp (254 and 366 nm) for 15 min in addition to the drying treatment. In the case of the multi-step preparation the above described procedures were applied for each step.

6.4   Characterisation of metal nanoparticles on monodisperse silica nanospheres

The coating of oxide nanospheres by metal nanoparticles aimed at forming core-shell-like structures can be characterized by two parameters, the mean particle size and the coverage, i.e. the portion of the nanosphere surface covered by metal particles. These parameters may vary with changing deposition conditions like origin, age and size of the oxide nanospheres, type and concentration of the precursor complexes as well as the drying temperature after impregnation, respectively. Additional UV light illumination and repetition of the deposition (multi-step procedure) cause further changes. All together they may affect the shape of the particle size distribution and the uniformity of the particle arrangement. For the success of efforts to fabricate core-shell structures it is required to adjust the conditions of synthesis so as to avoid bimodal size distributions and particle aggregates which indicate the presence of obstructing inhomogeneities.

6.4.1   Ag nanoparticle coating of silica nanospheres

General structural characteristics
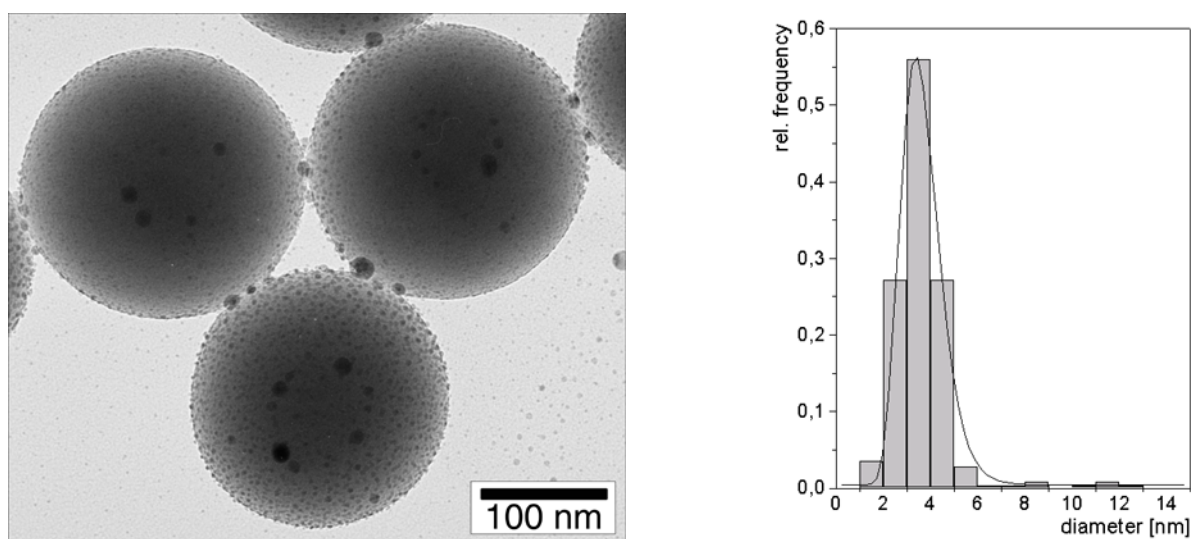
Fig. 6.11: TEM image and size distribution of Ag nanoparticles (2% silver acetate) on Monospher^{TM} silica upon 2h at 70°C.

Fig. 6.11 shows a characteristic TEM image of Monospher^{TM} silica nanospheres coated by Ag nanoparticles from a 2% silver acetate impregnation upon 2 h drying at 70°C, together with the corresponding size distribution. Both representations prove that the deposition method applied results in coverage of the oxide spheres by uniformly arranged very small metal particles of rather narrow size variation. In addition, more or less as by-product, there are some larger particles present which indicate that besides particle formation by nucleation and growth also coalescence and mobility of larger particles must be considered. A closer view on the achieved Ag nanoparticle coating is given by the HREM images of fig. 6.12. Three higher magnified selections (b), (c) and
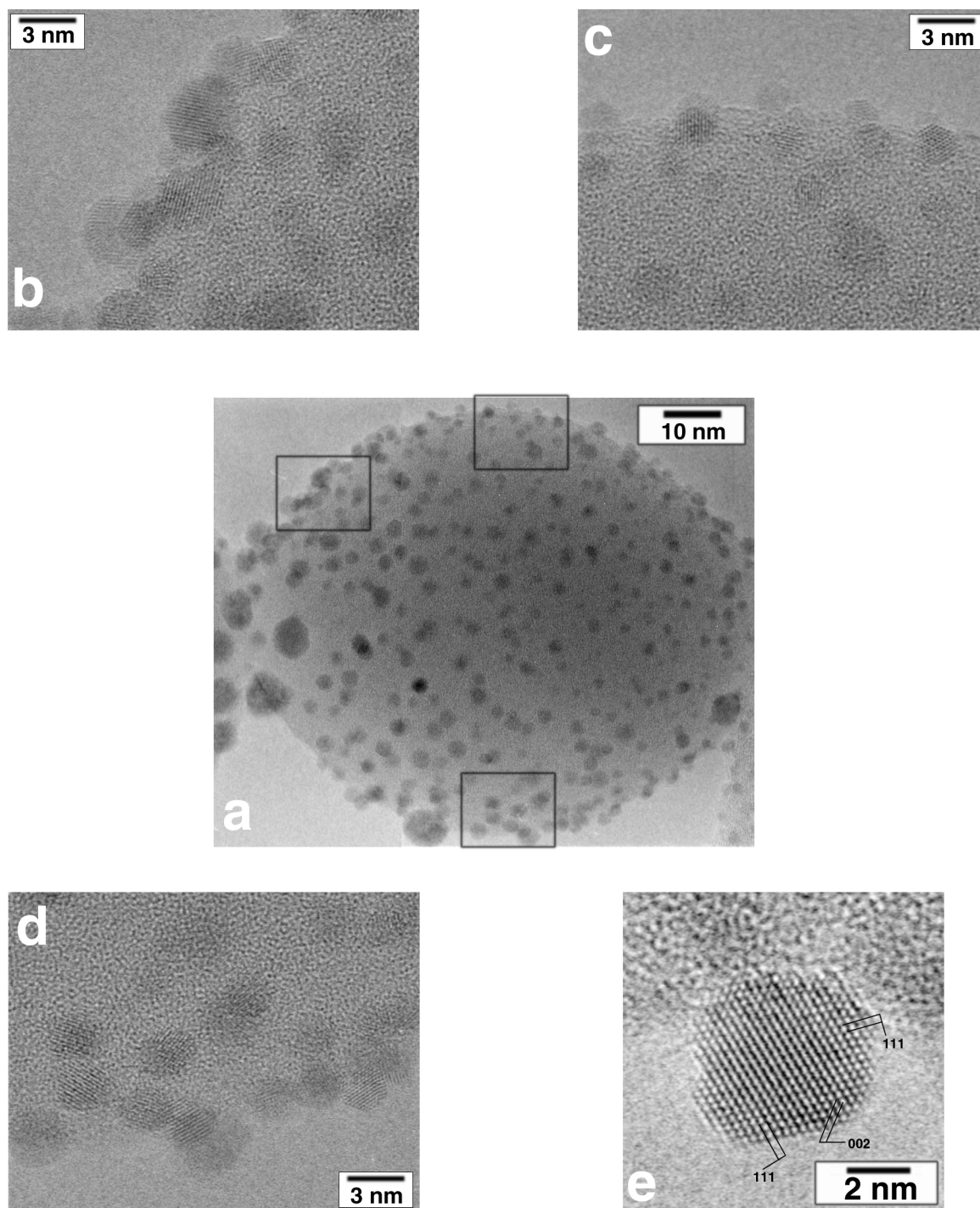
Fig. 6.12: *HREM image of Ag nanoparticles (2% silver acetate) on Monospher^{TM} silica upon 2h at 70°C (a). The areas marked by boxes are shown at higher magnification in (b), (c) and (d). Lattice plane fringes of {111} and {200} type are imaged at the particle shown in (e).*

(d), marked by boxes in (a), enable to recognize the nearly spherical shape of the particles and, by imaging of lattice plane fringes, their crystalline nature and random orientation with respect to each other. The even higher magnified image of a typical particle in (e) illustrates, in addition, that *(i)* the Ag particles are mostly single crystalline in this early stage of growth, *(ii)* they are facetted by crystallographic low index planes, and *(iii)* they do not exhibit any truncation owing to substrate-deposit interaction.
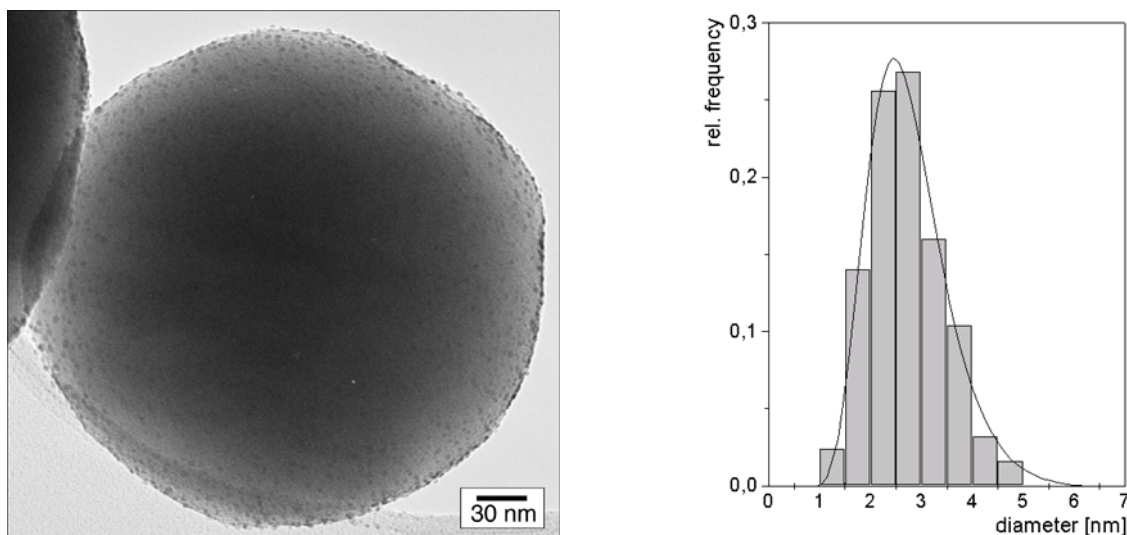
Fig. 6.13: *TEM image and size distribution of Ag nanoparticles (2% silver acetate) on Stöber silica (220 nm) upon 2h at 60°C.*

Fringe spacings and angular relationships of the lattice planes measured in the real space image as well as in the diffractogram (Fourier transformation) agree fairly well with those of the fcc lattice of bulk silver. The TEM image shown in fig. 6.13 together with the corresponding size distribution stand for the deposition experiment utilizing 2% silver acetate impregnation on laboratory-made Stöber silica (220 nm) upon 2h drying at only 60°C. Here the mean particle size (2.45 nm) is nearly the same as for the Monospher^{TM} coating (2.5 nm), but the size distribution is not bimodal since larger particles are missing. A quite similar result is obtained for applying another precursor, namely silver nitrate, for incipient wetness impregnation of Monospher^{TM} silica, even with a rather low concentration of 0.5%. This can be seen from fig. 6.14, where the TEM image and corresponding size distribution are combined with a HREM image to make visible the very small Ag particles. Accordingly, the first maximum of the size distribution occurs at 2.2 nm.

These very small Ag particles are expected to give rise to a CESR signal, but with all metal coated monodisperse silica there was no magnetic resonance measurement feasible for technical reasons.

Optical characteristics

At low metal loading, as for instance that one shown in fig. 6.13, there is no visual indication of Ag nanoparticle surface plasmon resonance to be recognized. The sample does not change its white
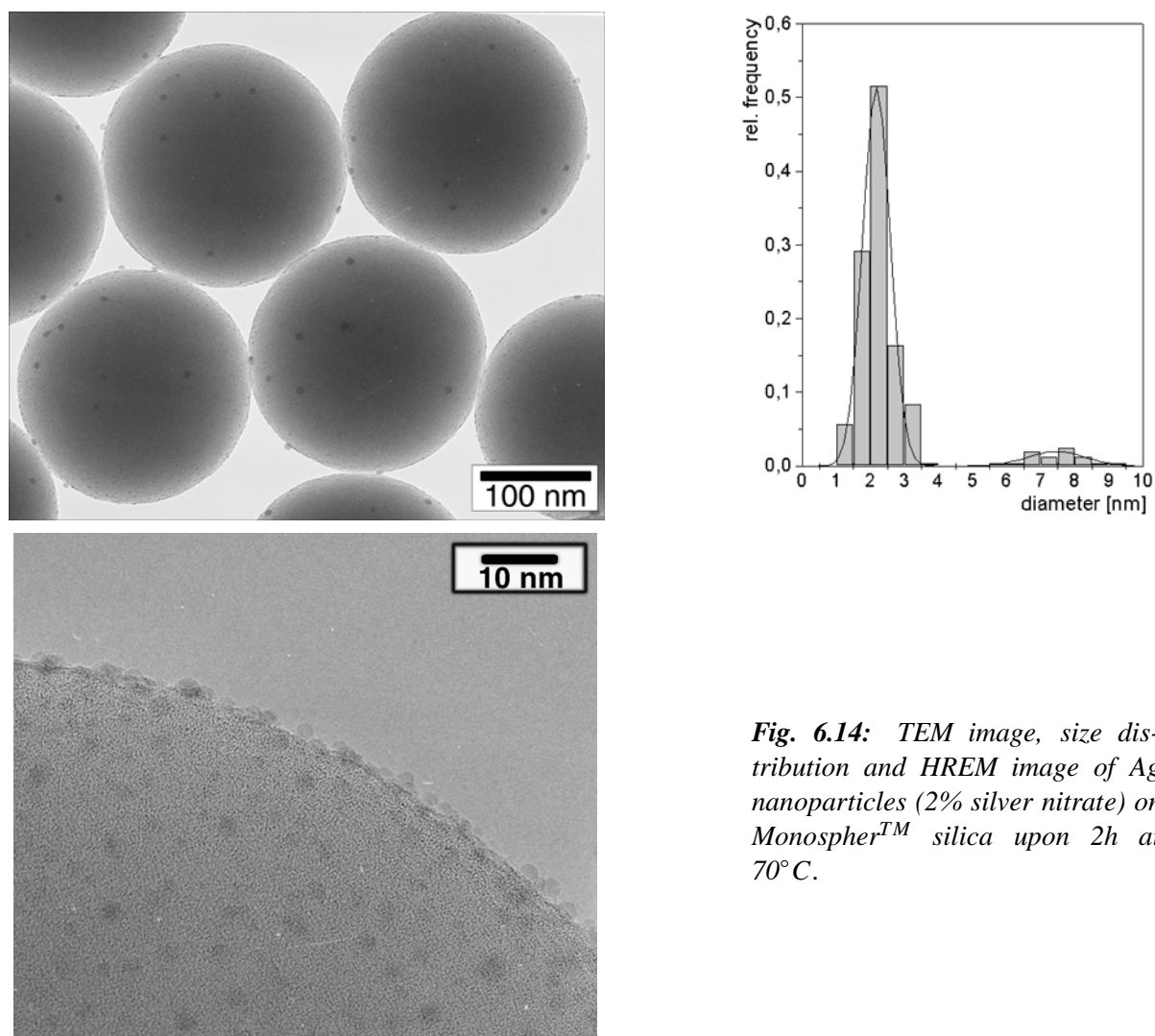
Fig. 6.14: *TEM image, size distribution and HREM image of Ag nanoparticles (2% silver nitrate) on Monospher^{TM} silica upon 2h at 70°C.*

appearance as compared to the non-impregnated silica nanospheres. The extinction spectrum of this sample shown in fig. 6.15 (red curve) does not exhibit a signature of metal particle resonances, but a rather broad extinction in the corresponding region. For comparison, a spectrum calculated for Ag particles in a silica matrix using the Mie theory is shown in the figure (black curve). The calculation is based on the dipolar approximation for particles of 2 to 2.5 nm size taking into account the quantum size effect expected for this size range. The mean value of the Drude plasma frequency $\omega_p = 1.4 \times 10^{16}$ s^{-1} is taken from the literature [Bor86, Höv93] and the Fermi velocity $v_F = 1.45 \times 10^6$ m/s as well [Ash76, Kit96]. For the real dielectric function of silica a constant value of 2.25 is used and a filling factor of 0.2 is chosen for the Ag component. This results in a reasonable intensity of the resonance peak with maximum at 425 nm in agreement with the findings of Kreibig [Kre97a]. However, the filling factor exceeds by far that one corresponding to the silica nanospheres coated by an incomplete layer of Ag nanoparticles. Here, from 215 nm mean diameter of silica spheres and 2.5 nm mean diameter of Ag particles a nominal loading factor (comparable to a filling factor) of 0.0065 is estimated taking into account 19% coverage of the silica surface. Consequently, the spectra of such samples are necessarily dominated by the contributions of silica nanospheres. As may be recognized from fig. 6.16 the extinction spectra of Monospher^{TM} (250
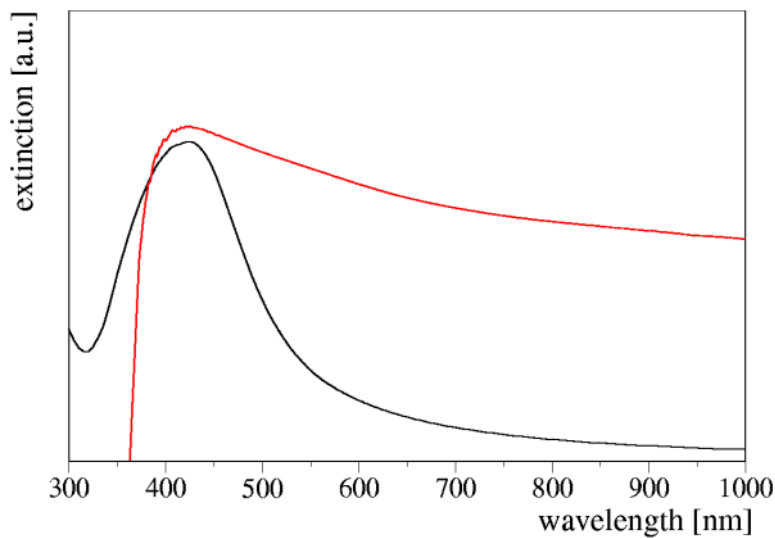
Fig. 6.15: Extinction spectrum of the Ag nanoparticle coating on Stöber silica (220 nm) shown in fig. 6.13 (red) compared to a calculated spectrum of Ag particles in silica matrix using dipolar approximation.

nm) silica (black curve) and Stöber (220 nm) silica (blue curve) exhibit only broad and featureless peaks due to light scattering [Ji01] with maxima at about 423 and 430 nm, respectively. The Stöber silica spectrum compares very well to the one of the Ag nanoparticle coated sample shown in fig. 6.15. The above interpretation is confirmed by the calculated spectrum (red curve) of fig. 6.16
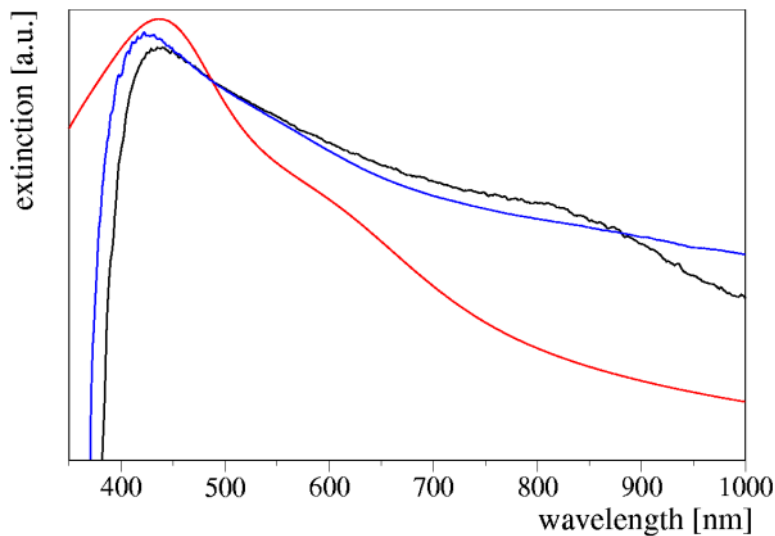
Fig. 6.16: Extinction spectrum of Monospher^{TM} (250 nm) silica (black curve) and Stöber (220 nm) silica (blue) compared to a calculated spectrum of silica spheres (220 nm) using dipolar approximation (red).

obtained from Mie theory dipolar approximation for 220 nm silica nanospheres with taking into consideration the already mentioned real dielectric function of silica and $\varepsilon = 1$ for air as matrix. Only when more metal is deposited and/or larger particles are formed on the silica by increasing the precursor concentration, enhancing the drying temperature, or applying a multi-step procedure, as will be shown below, the characteristic brownish yellow color of small Ag particles becomes visible.

Coating characteristics

In the frame of efforts to control size and size evolution of the metal nanoparticles deposited by incipient wetness impregnation on silica nanospheres, the influence of precursor concentration,

drying temperature and repetition of deposition steps was investigated in a certain range. The influence of UV light illumination was tested for various deposition conditions, but no systematic and reproducible effect could be established. A possible explanation of this behavior may be that the essential reactions of metal precursor decomposition and reduction to atomic metal are effective already at room temperature, before any further treatment by light or heat. Drying at slightly enhanced temperatures then should only affect the formation of metal particles.
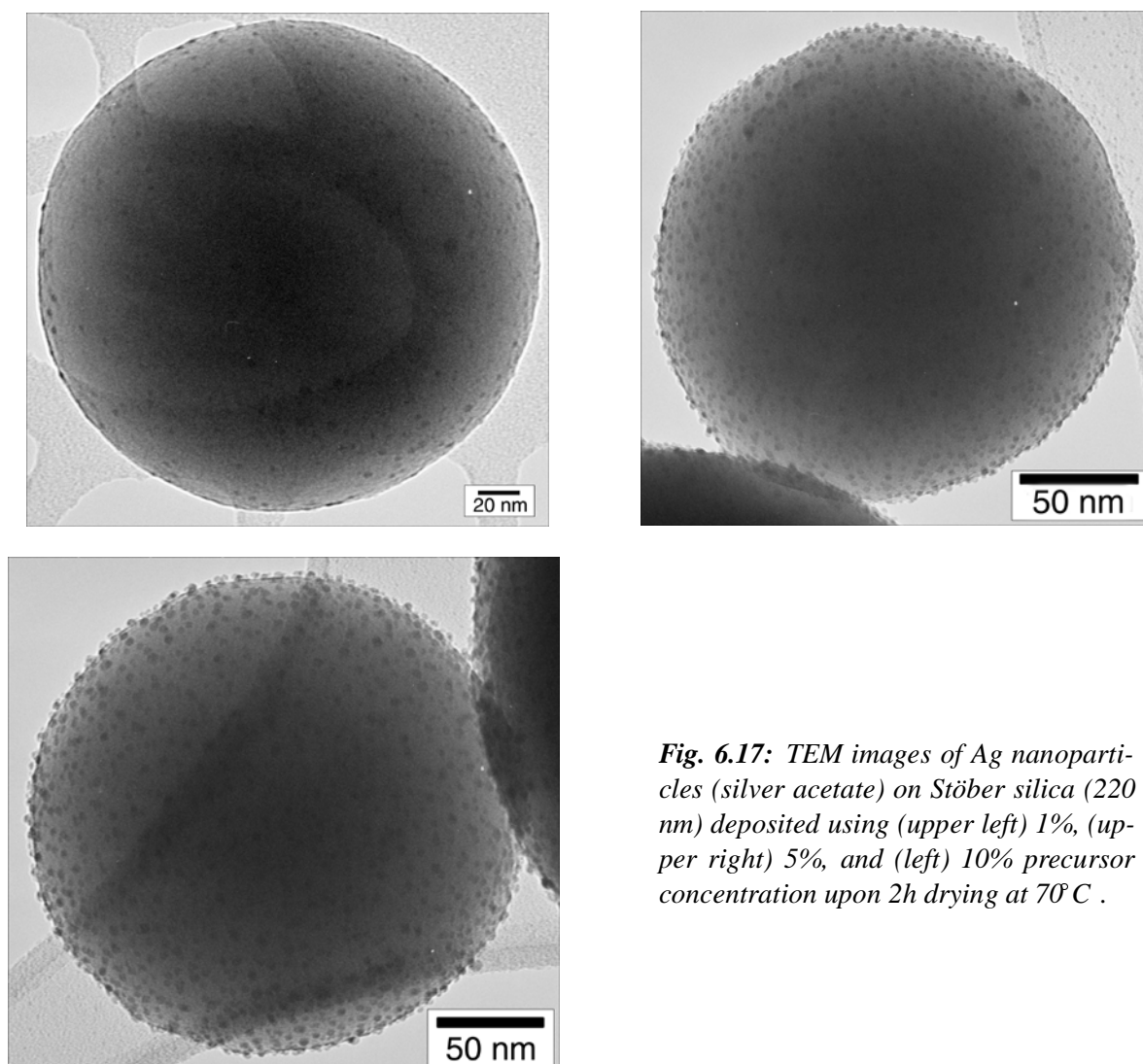
Fig. 6.17: TEM images of Ag nanoparticles (silver acetate) on Stöber silica (220 nm) deposited using (upper left) 1%, (upper right) 5%, and (left) 10% precursor concentration upon 2h drying at 70°C .

Stöber silica (220 nm) samples were employed in a series of incipient wetness impregnation experiments with silver acetate precursor concentrations ranging from 1 to 10%. Fig. 6.17 shows TEM images of the 1%, 5% and 10% samples upon 2 h drying in vacuum at 70°C and Table 6.4 comprises the coating characteristics of the whole series. The increase in coverage of the silica surface by Ag particles from 13 to 48% is achieved by both, particle growth and nucleation of new particles. Here a nominal metal loading factor can be estimated from the silica core diameter and the Ag mean particle diameter (used as shell thickness) with considering the incompleteness of the metal shell by the respective coverage.

Table 6.4: *Characteristics of Ag nanoparticles (silver acetate) on Stöber silica (220 nm) for various precursor concentrations upon 2h drying at 70°C.*

Concentration [%]	Mean size [nm]	Stand. dev. [nm]	Coverage [%]
1	2.2	0.2	13
2	2.2	0.2	14
4	2.7	0.3	30
5	2.8	0.2	32
10	3.6	0.2	48

This metal loading linearly increases from 0.0039 to 0.0233 in the concentration range studied. It is remarkably, that there was no change of the uniform arrangement of metal particles on the silica surface and no aggregates were formed [Hof02]. Also the size distribution remains narrow and monomodal, indicating rather uniform particle growth and the absence of coalescence and enhanced particle mobility. Even for 10% precursor concentration a dense population of Ag particles of only 3.6 nm mean size was obtained. These are very promising characteristics making the chosen conditions of synthesis well suited for fabrication of core-shell structures of extremely low shell thickness.
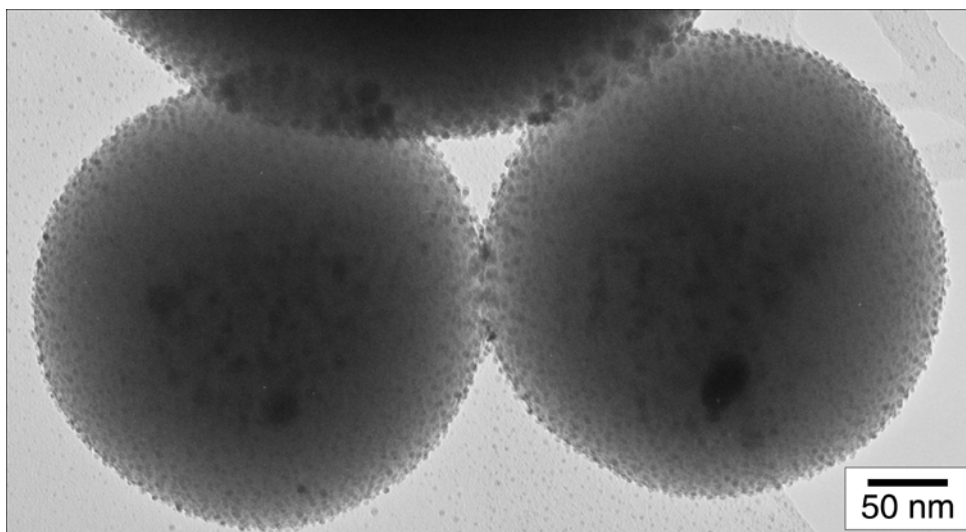
Fig. 6.18: *TEM image of Ag nanoparticles (10% silver nitrate) on Stöber silica (300 nm) upon 2 h drying at 70°C.*

An equivalent series was prepared with silver nitrate as metal precursor of concentrations ranging from 1 to 10% on Stöber silica (300 nm). Fig 6.18 shows a TEM image of the 10% sample upon 2 h drying at 70°C and Table 6.5 comprises the coating characteristics of all samples of this series. Besides the observation of a bimodal size distribution in the 1% sample, similar to that of the 0.5% sample shown in fig. 6.14, as well as a few irregularly shaped particles of extraordinary large size in the 10% sample, this series is, as a whole, comparable to that one with silver acetate precursor. A considerable increase in coverage of the silica surface by uniformly arranged Ag particles of slightly changing size is achieved with increasing silver nitrate concentration and the metal loading increases from 0.0022 to 0.0123. With this metal complex the nucleation rate,

compared with the growth rate, is raised upon enhancing the precursor concentration more than it was observed for silver acetate. Therefore, the metal loading achieved is smaller with silver nitrate than with silver acetate.

Table 6.5: *Characteristics of Ag nanoparticles (silver nitrate) on Stöber silica (300 nm) for various precursor concentrations upon 2h drying at 70°C.*

Concentration [%]	Mean size [nm]	Stand. dev. [nm]	Coverage [%]
1	2.2	0.2	10
	9.6	3.5	
2	2.4	0.3	10
4	2.4	0.2	25
5	2.6	0.2	28
10	2.6	0.3	48

Since for completing core-shell structures, at least from a certain point on, growth without nucleation of new particles would be favorable, the question arises, how the coating characteristics are influenced by variations of the drying temperature. This was studied by equivalent series with 4% of each metal precursor where the drying temperature was varied from 70°C to 300°C. The results of the silver acetate sample, obtained with Stöber silica (220 nm) are compiled in Table 6.6 and the results of the silver nitrate sample obtained with Stöber silica (300 nm) are compiled in Table 6.7.

Table 6.6: *Characteristics of Ag nanoparticles (4% silver acetate) on Stöber silica (220 nm) for various drying temperatures.*

Temperature [°C]	Mean size [nm]	Stand. dev. [nm]	Coverage [%]
70	2.7	0.3	30
100	2.6	0.3	29
	10.5	1.7	
200	2.7	0.3	25
	18.2	3.8	
300	2.9	0.3	18
	22	10.7	

Both series exhibit the same behavior. The more the drying temperature is enhanced, the more the particle size distribution broadens and becomes bimodal. Simultaneously, the coverage of the silica surface distinctly decreases, indicating that at higher drying temperatures the growth proceeds via consumption of a certain portion of particles. Hence, the uniformity of size and arrangement observed for lower temperatures will be disturbed. Since the shape of individual particles remains nearly spherical, this behavior is supposed to be caused by increased particle-particle interaction and coalescence processes. It does not allow to increase the metal loading essentially, but worsens the shell-like properties of the coating. Consequently, the enhancement of the drying temperature is not suited for our purpose.

Table 6.7: *Characteristics of Ag nanoparticles (4% silver nitrate) on Stöber silica (300 nm) for various drying temperatures.*

Temperature [°C]	Mean size [nm]	Stand. dev. [nm]	Coverage [%]
70	2.4	0.2	25
100	2.4	0.5	17
	6.5	1.2	
200	2.5	0.4	15
	20.1	3.8	
300	2.7	0.6	15
	20	10.7	

The third modification of the initial incipient wetness impregnation, the repetition of the deposition in a multi-step procedure, was tested with 2% of both Ag precursor complexes on Stöber silica (300 nm) using 2 h drying at 70°C. The second deposition resulted in a coverage increase
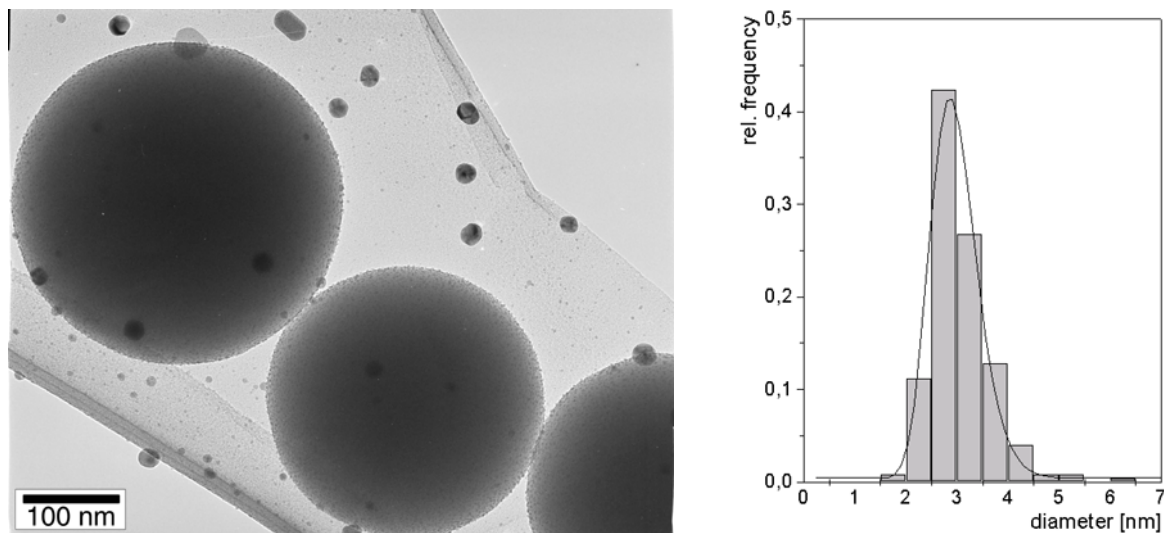
Fig. 6.19: *TEM image and size distribution of Ag nanoparticles (2% silver acetate) on Stöber silica (300 nm) upon step 3 of the multi-step procedure.*

to 16%, less than obtained in the one-step procedure employing an equivalent amount of silver acetate, accompanied by a second maximum around 12.5 nm in the size distribution. The third deposition step results in further increase of particle growth to 2.9 nm (first maximum of the size distribution) and 20 nm (second maximum) and coverage to 26%. However, the coverage is distinctly below the one-step procedure result and most of the large particles did not remain on the silica nanosphere surface, but were deposited on the carbon during preparation for electron microscopy. A characteristic TEM image of this situation is given in fig. 6.19 for the silver acetate sample together with the size distribution of the Ag particles remaining on the silica. The results are quite similar for the multi-step procedure applied to the silver nitrate sample.

The observed behavior indicates that this multi-step procedure cannot be understood in terms of a so-called "seeding" treatment, where an enlargement of metal particles is achieved by surface-catalyzed reduction of metal ions based on the presence of preformed particles. No new particle nucleation occurs, but a uniform growth of the seeds [Bro00, Jan01, Sau01]. The incipient wetness

impregnation, however, is mediated by terminating groups of the silica surface which are available also when the procedure is repeated. The accommodation of freshly formed metal atoms on preexisting particles occurs in competition to nucleation processes as long as there is enough free surface present, leaving behind a bimodal distribution of particle sizes. The larger the particles are grown the easier they are affected by capillary forces during preparation for TEM and disappear from the silica nanosphere surface.

6.4.2   Au nanoparticle coating of silica nanospheres

General structural characteristics

All samples with Au nanoparticles have been prepared by employing hydrogentetrachloroaurate as metal precursor either on Monospher^{TM} silica or on Stöber silica (300 nm) nanospheres. Fig. 6.20(a) shows a characteristic HREM image together with the corresponding size distribution of Monospher^{TM} silica coated by Au particles from a 1% precursor sample upon 2 h drying at $70°C$. Similar to the experiments with Ag, a dense coverage of uniformly arranged small gold particles of narrow size distribution given in fig. 6.20(b) is obtained. Accordingly, the crystalline nature and random orientation with respect to each other is ascertained. The tendency to form particles of nearly spherical shape without truncations at the interface is well established owing to the weak interaction between gold deposit and silica substrate which is assumed to be even smaller as in the case of silver. Actually, the particles exhibit cuboctahedral shape rather than that of ideal spheres.

Table 6.8: *Characteristics of Au nanoparticles (1% precursor) on Monospher^{TM} silica upon 2h drying at $120°C$ and 2 to 4 h additional drying at various temperatures.*

Temperature [°C]	Time [h]	Mean size [nm]	Stand. dev. [nm]	Coverage [%]
100	4	2.3	0.2	16
200	4	2.5	0.3	12
300	2	2.9	0.9	17
		18	10.7	
300	4	3	1.2	15
		19.5	5	

Simultaneously, a tendency to form larger particles is observed which generally causes broader and more frequently bimodal size distributions as compared to silver. The smaller particles, i.e. those below about 5 nm in size, mostly are single crystalline as can be seen in fig. 6.20(c). The larger particles frequently exhibit planar defects like twin boundaries; an example is shown in fig. 6.20(d). Imaging of lattice plane fringes allows to measure fringe spacings and angular relationships which are found to agree fairly well with those of the fcc lattice of bulk gold.

Experiments to study by additional drying at elevated temperatures the evolution of particle size and coverage were carried out with the 1% precursor sample upon 2 h drying at $120°C$. The results are compiled in Table 6.8. They represent an increasing loss of uniformity of particle size
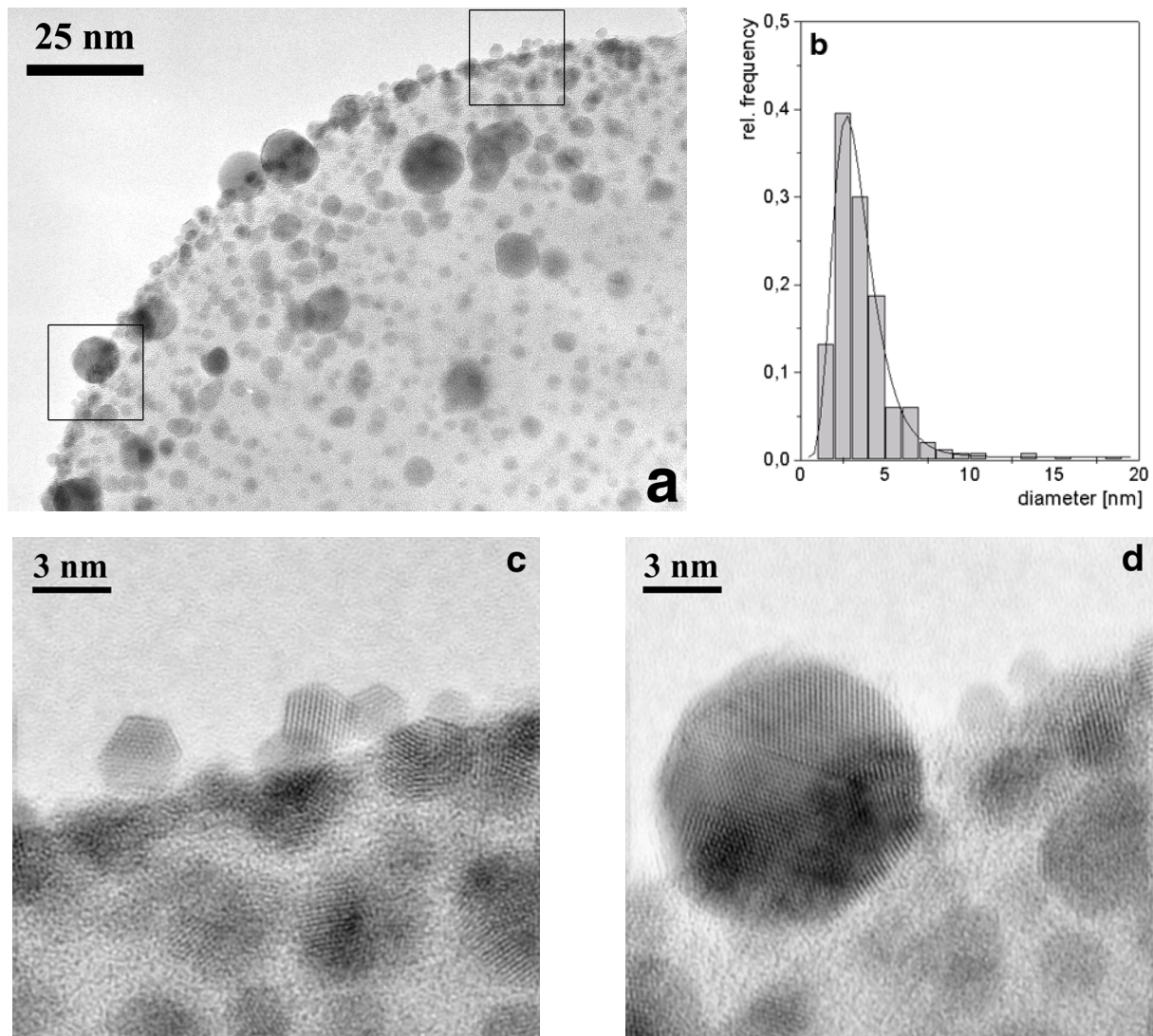
Fig. 6.20: *HREM image (a) and size distribution (b) of Au nanoparticles (1% precursor) on Monospher^{TM} silica upon 2h drying at 70°C. The areas marked in (a) by boxes are shown at higher magnification in (c) and (d).*

and arrangement due to the increased appearance of larger species. Although this behavior leads to a bimodal size distribution, there remains a considerable population of rather small particles around 3 nm size and less, having a relatively narrow size distribution. Consequently, the coverage of the silica surface does not essentially decrease.

Optical characteristics

Similar as in the case of silver, also with gold there is no indication of nanoparticle surface plasmon resonances at low metal loading and very small particle sizes. The spectrum of the 1% sample dried 2 h at 120°C (see Table 6.8 above) does only exhibit a rather broad extinction dominated by scattering contributions of silica nanospheres. In contrast to silver, the maximum of the surface plasmon resonance of small gold particles is situated around 550 nm such that it is not completely covered by the extinction of silica nanospheres. Hence, with the occurrence of a sufficient number
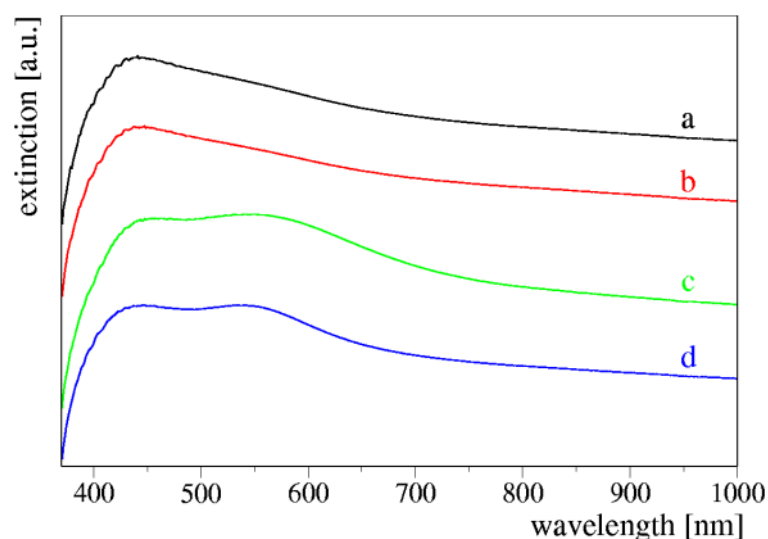
Fig. 6.21: *Extinction spectra of Au (1% precursor) on Monospher^{TM} silica upon 2h drying at 120°C (a) and additional drying: 4h at 100°C (b), 4 h at 200°C (c), and 2 h at 300°C (d).*

of particles larger than about 10 nm the resonance damping is less effective and the evolution of metal particle resonances is observed. This behavior may be demonstrated by the extinction spectra shown in fig. 6.21 of the samples subjected to additional drying at elevated temperatures (see Table 6.8). Simultaneously, the color appearance of the sample powder changes from a cloudy yellow to a speckled violet. The apparent blue-shift of the Au particles resonance position from about 565 to 540 nm, seen in the spectra of the additionally dried samples, is not indicative of certain size effects, but most probably due to superposition with the predominating extinction of silica nanospheres. The more the metal plasmon resonance evolves out of the background, the more the maximum
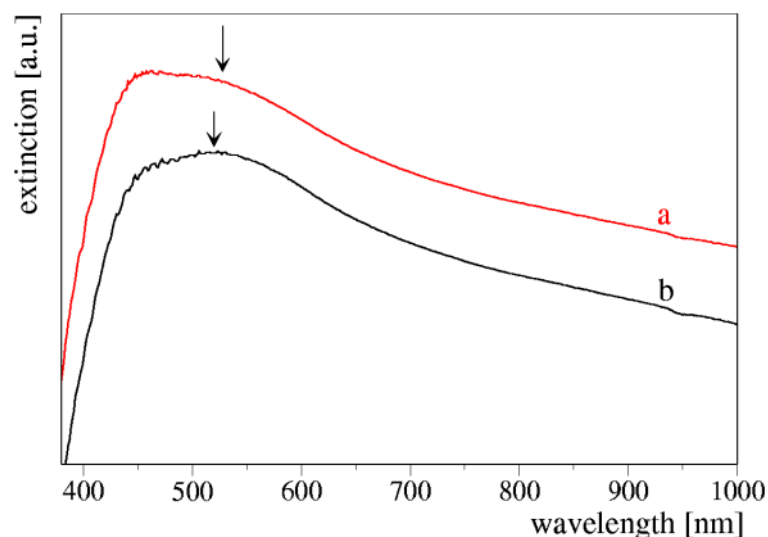
Fig. 6.22: *Extinction spectra of Au (1% precursor) on Stöber silica (300 nm) upon 2h drying at 70°C (a) and 6 h additional drying at 70°C (b).*

of the corresponding shoulder moves towards the true resonance position. Similar results were obtained with the sample prepared by employing 1% metal precursor on Stöber silica (300 nm) upon 2 h drying at 70°C that has been subjected to 6 h additional drying at this temperature. The corresponding extinction spectra are shown in fig. 6.22.

Coating characteristics

The coating experiments with silver making use of a variation of the metal precursor concentration proved to be the most successful approach to core-shell-like structures. For the gold precursor similar incipient wetness impregnation experiments were undertaken with concentrations ranging from 1 to 5% applied to Stöber silica (300 nm) nanospheres which always were dried 2 h at 70°C. Fig. 6.23 shows TEM images and size distributions of the 2%, 4% and 5% samples and Table 6.9 comprises the coating characteristics of the whole series. Most remarkably is the huge increase in coverage of the silica nanosphere surface by Au nanoparticles from 10% to 65%.

Table 6.9: *Characteristics of Au nanoparticles on Stöber silica (300 nm) for various precursor concentrations upon 2h drying at 70°C.*

Concentration [%]	Mean size [nm]	Stand. dev. [nm]	Coverage [%]
1	2.2	0.2	10
2	2.4	0.3	17
4	3.7	0.3	32
	8.1	2.3	
5	3.8	0.8	65
	6.6	1.3	

The increase of particle size and coverage, being larger than with comparable samples of the silver series, is mainly brought about by the rapid growth of a considerable portion of the particles. Nevertheless, there remains an even greater population of smaller particles having a narrow size distribution centered around 3 to 3.5 nm. This behavior requires an enhanced growth rate, favored by particle-particle interaction and coalescence, being active simultaneously with a high nucleation rate appropriate for compensation of particle consumption due to growth processes. The 5% sample exhibits core-shell-like structures where many Au nanoparticles already are interconnected in a network. These still incomplete Au nanoshells, however, cannot be improved by enhancing further the concentration of the metal precursors. With 10% hydrogentetrachloroaurate applied under the same conditions excessive particle growth leads to a loss of most of the particles from the silica nanospheres upon preparation for electron microscopy. The optical properties of the 5% sample are not as promising as fig. 6.23(c) looks like. The spectra of the concentration series do not show essential improvment as compared tho those of figs. 6.21 and 6.22. The main reason for this behaviour is that no shell signature is developed as long as the metal particle coating remains incomplete. Furthermore, the maximum of the corresponding resonance for this core size should be beyound the limits of the used spectrometer. Another reason is the inhomogeneity of the samples produced by incipient wetness impregnation. The high quality coating characteristics shown in fig. 6.23(c) are not observed at the same level throughout the whole sample. Repetition of the incipient wetness impregnation in a multi-step procedure was also utilized for the Au precursor complex with 1% on Stöber silica (300 nm) using 2 h drying at 70°C in vacuum. TEM images and the corresponding size distributions of the first and the repeated deposition are shown in fig. 6.24.
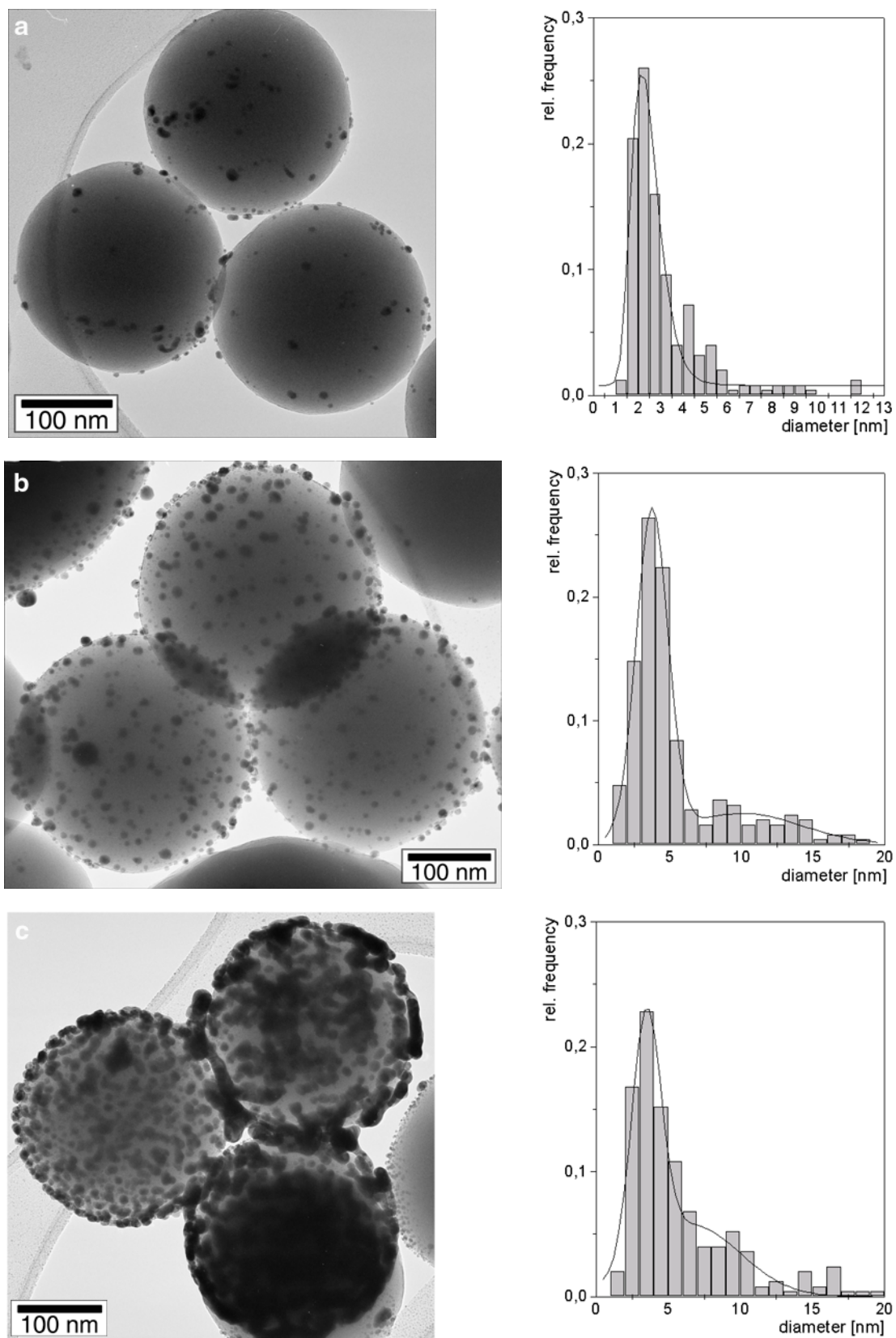
Fig. 6.23: *TEM image and corresponding size distribution of Au nanoparticles on Stöber silica (300 nm) deposited using (a) 2%, (b) 4%, and (c) 5% precursor concentration upon 2h drying at 70°C.*
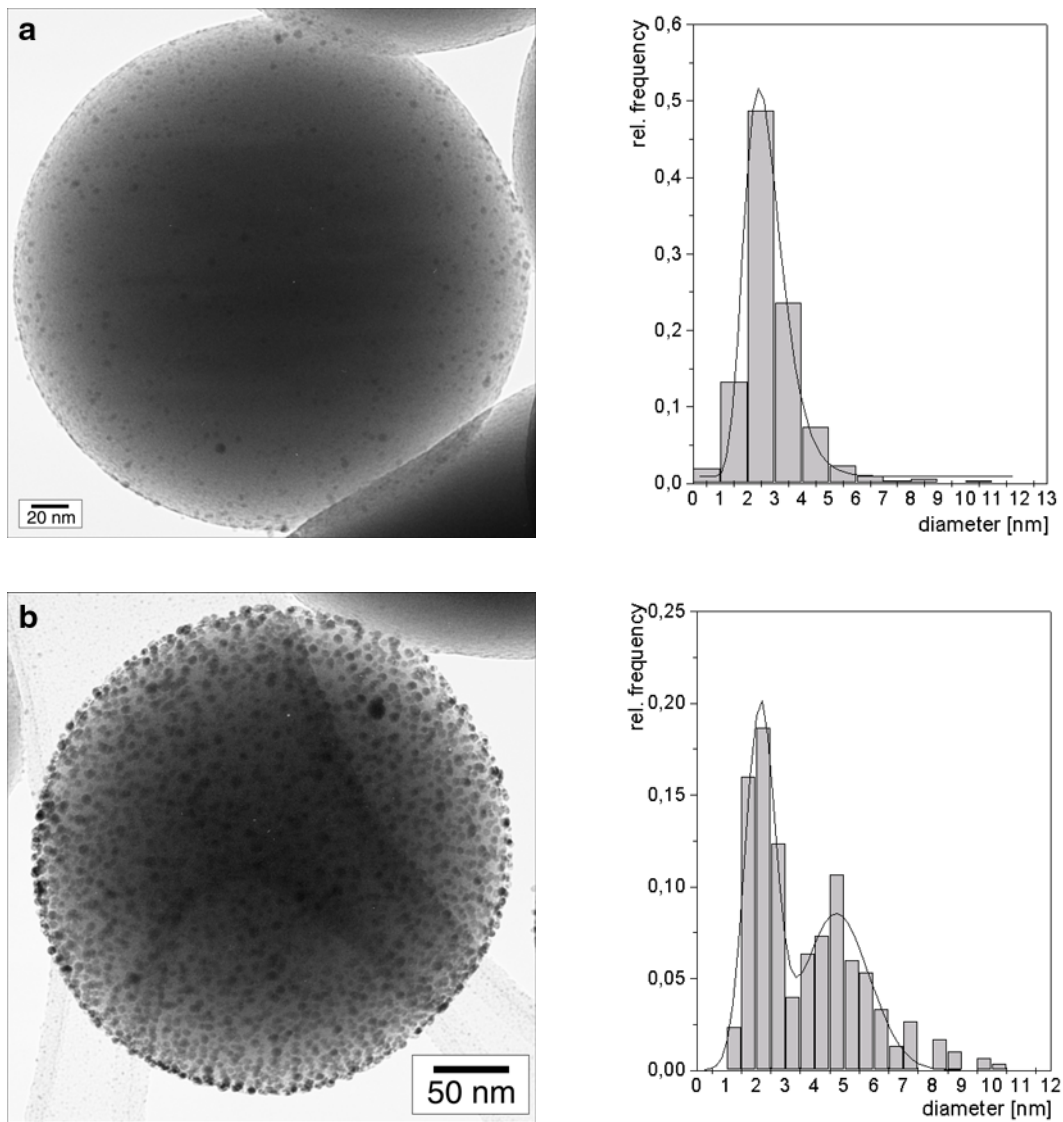
Fig. 6.24: *TEM image and size distribution of Au nanoparticles (1% precursor) on Stöber silica (300 nm) upon 2h drying at 70°C, (a) first and (b) repeated deposition.*
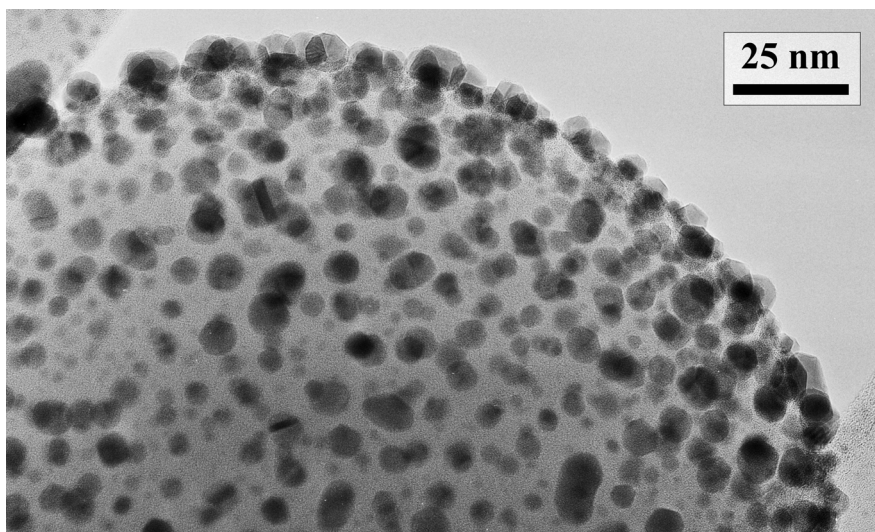
Fig. 6.25: *HREM image of Au nanoparticles (1% precursor) on Stöber silica (300 nm) upon 2h drying at 70°C: repeated deposition.*

The particle size changes from 2.4 ± 0.3 nm mean value of a monomodal distribution to 2.1 ± 0.3 nm and 4.7 ± 1.3 nm of a bimodal distribution in a remarkably uniform way, quite different from the findings with repeated deposition of Ag. The coverage increases from 17% to 52% is by far above that one obtained in a one-step procedure employing an equivalent concentration of the precursor complex [Hof02]. This behavior points to simultaneously proceeding nucleation and growth processes, similar to the case of silver.

However, with gold the nucleation rate and the growth rate obviously are well adjusted to each other so as to keep the uniformity of the nanoparticle coating while increasing the metal loading. It can be assumed that the nucleation rate is governed by the availability of reducing radicals on the silica surface, being approximately a function of free space, and the growth rate is governed by both, concentration of metal atoms and small clusters on the surface, respectively, and their mobility. Therefore, low precursor concentration and low temperature approaches are more successful in producing core-shell-like structures. A closer view to the Au nanoparticle coating achieved by the above described repeated deposition is given by the HREM image of fig. 6.25. There are some particles showing inhomogeneous image contrasts since they contain planar defects, while some particles show irregular shapes resulting from coalescence processes. This image, similar as the one shown in fig. 6.20(a), may indicate that the Au particles reside well on top of the silica surface sharing only a small contact plane with the substrate.

Short review of results

Summarizing the results of the metal coating experiments using incipient wetness impregnation one may conclude, that with both metals applied a uniform and reasonably dense nanoparticulate coverage of monodisperse silica nanospheres could be achieved. The newly introduced method, oxide surface-mediated reduction of metal complexes only slightly above room temperature, makes use of the potential of terminating hydroxyl groups for reducing metal ions. It is well suited to prepare metal nanoparticle coatings on monodisperse silica nanospheres without external reducing agents or media and absolutely free of adhesive aids or functionalizing agents usually applied to achieve particulate coatings. The general structure of particles of both metals is quite the same. Single crystalline particles of nearly cuboctahedral shape grow on the silica surface without indications of substrate-deposite interaction. With particle sizes increasing above about 5 nm, planar lattice defects and shape deviations occur indicating some changes in the growth mode. Despite the uniform arrangement of particles and relatively dense coverage of the oxide surface, the overall filling factor remains rather low. Consequently, the optical spectra mainly reflect the light scattering properties of silica nanospheres having a broad maximum at about 425 nm. Only upon higher metal loading, when resonance damping effects decrease because of increasing particle size, and particular for Au with the surface plasmon position at about 550 nm, the signature of metal particle resonances is observed. Core-shell resonances of the nanospheres studied are expected to occur not in the visible, but in the near infrared region, and only upon formation of closed shells. Although this aim was not yet attained, some improvements of the coating characteristics were

achieved by variation of precursor concentration and drying temperature. With Ag nanoparticles the coverage could be enhanced up to nearly 50%, preserving a remarkably uniform particle size and arrangement, by appropriately increasing the concentration. With Au nanoparticles the effect was even better and a coverage of 65% was achieved, but just for a moderate concentration increase, the uniform particle size was lost rapidly. Increasing the drying temperature is not useful for both metals since an increasing loss of uniformity of particle size and arrangement results, accompanied by a reduced coverage of the oxide. Another way, repetition of the incipient wetness impregnation and drying to compose a multi-step procedure, did not work well with Ag nanoparticles since the coverage did not increase accordingly, but a bimodal size distribution was produced. A similar procedure with Au, applying only half that concentration in the single step, produced a more satisfying result with a coverage increase distinctly above the one obtained by employing an equivalent concentration in a one-step procedure. It is important to note that from the observed behaviour one cannot classify the multi-step procedure as a kind of seeding treatment. The accommodation of metal atoms, freshly formed in the second step, can occur on preexisting particles, but in competition to nucleation processes on the not yet covered silica surface.

7 Summary and outlook

This thesis reports on an extensive investigation on the formation of metal nanoparticle coatings on oxide nanospheres and their characterization. These coatings, aimed at forming core-shell structures, are challenging because of the novel optical properties of such structures that may be tuned in wide ranges by variation of core size and shell thickness. The experimental realization of a corresponding investigation requires to explore suitable routes of synthesis including appropriate materials of core and shell. The attempt to form core-shell structures by metal deposition on oxide nanospheres is approached in several steps which obey the determination to avoid surface contamination by functionalizing agents and to enable moderate temperature processing. These objectives have not been considered so far in the literature concerning this subject.

The detailed steps of this approach concern various aspects of the complex investigation. One of these aspects is that of the oxide materials employed must meet some requirements. These are in brief: *(i)* the geometric characteristics of appropriate size and shape to serve as support for concentric metal shells, *(ii)* the dielectric function of suitable characteristics, and *(iii)* the surface state in terms of surface groups which may act as reducing radicals or as preferred sites of metal atom accomodation in the process of metal deposition by chemical means. Other aspects are the process of metal deposition itself, and the type of metal of which appropriate precursor compounds and suitable deposition characteristics may be found. To this aim a new method of metal coating, namely surface-mediated reduction of metal complexes at low temperatures, was introduced.

A number of oxide materials were examined with respect to their structural characteristics by electron microscopy, and to the presence of hydroxyl groups by thermal gravimetry analysis. Mesoporous non-planar oxides, readily available and non-expensive, offered the advantage of a high specific surface area accompanied by a rather high concentration of surface hydroxyl groups. Although not being useful to build core-shell structures, these materials allowed us to test the deposition of 11 different metals using various precursors. Commercially available, polydisperse nanospheres of silica, alumina, titania and hematite were tested, but only the NANOTEK silica and the CERAC titania provided sufficiently smooth surface and spherical shape to be used in metal deposition experiments. The rather low concentration of hydroxyl groups on the surface of these materials is due to their origin from pyrolysis techniques. The best choice for the purpose of core-shell structures are so-called "monodisperse" oxide nanospheres which have a very narrow size distribution. Besides commercially procured Monospher^{TM} silica of MERCK, laboratory-made Stöber silica nanospheres with mean diameters ranging from about 100 to 300 nm have been used in metal nanoparticle coating experiments. These materials have a rather high surface hydroxyl

content. Oxide nanospheres of the above size range are best suited for structural characterization by transmission electron microscopy of the coating details.

Three different routes to achieve coating of oxide nanospheres by metal nanoparticles have been explored. One, tested extensively on non-planar oxides, consists in the replacement of terminating hydroxyl groups by aluminium-hydrogen surface complexes to enable controlled reduction of metal complexes which were applied by impregnation from solution. A subsequent drying procedure at 100 to 300°C resulted in metal nanoparticles, the size, size distribution and concentration of which varied from metal to metal and also for different metal precursors of the same metal. However, generally very small metal particles are formed with sizes around 2 nm.

For particles of the ferromagnetic metals Ni, Co and Fe superparamagnetic resonance signals were observed. Its temperature dependence allowed to derive the corresponding particle size in line with TEM. Besides for their coating characteristics, the particles of paramagnetic group VIIIB metals were inspected for conduction electron spin resonance. Such signals were observed for Rh and Pt. The uniformity of the arrangement and stability of size dispersion is most remarkably for Pt particles. The group IB metals Cu, Ag and Au exhibit, in this order, an increasing tendency to form larger particles under otherwise comparable deposition conditions, leading to a bimodal size distribution for the last metal. From magnetic resonance measurements at Ag and Cu samples CESR signals could be identified. As a general observation from the magnetic resonance spectra of all samples prepared according to this route of synthesis, indications for the presence of metal ions as well as signals due to paramagnetic defect species at the silica surface were frequently found. The latter may result from re-oxidation of atomically dispersed metal at residual hydroxyl groups, simultaneously producing the former.

The second route of synthesis was chosen for polydisperse oxides of various origin. It makes use of thermally unstable organometallic precursors applied by impregnation from solution leading to the formation of organometallic surface complexes. Since no further reducing treatment is required, this procedure is well suited for the polydisperse nanospheres having only low surface hydroxyl concentration. It was used with two different organometallic precursors of Pt and Pd for silica as well as for titania nanospheres and mostly produced uniformly arranged metal particles with mean sizes around 2.5 nm and narrow size distribution. At very low precursor concentration the coating characteristics of silica did not worsen upon drying at temperatures as high as 300°C. At Pt nanoparticles on silica nanospheres prepared this way quantum size effect was evidenced by magnetic resonance measurement (CESR). Even better results were obtained for high precursor concentrations without raising the temperature above RT. On titania nanospheres, the uniformity of the metal particle arrangement was not as good and the low temperature deposition did not work quite well. Nevertheless, it may be concluded that metal deposition from organometallic precursors is well suited as prenucleation step for creating core-shell structures with oxide nanospheres of poor surface hydroxyl content.

Monodisperse silica nanospheres with a relatively high content of surface hydroxyl groups offered the exploration of a third route of synthesis. This surface-mediated process utilizes the

potential of terminating groups for reduction of metal ions of precursor compounds applied by incipient wetness impregnation. It was used for a more systematic study of the coating characteristics of Ag and Au nanoparticles. The general structural characteristics is quite the same for both metals. A dense population of uniformly arranged, rather small particles having a narrow size distribution covers the silica nanospheres upon drying at temperatures around 70°C. It is for the first time that metal particle formation at such low temperatures on oxide support without applying external reducing agents or media is reported. The particles are single crystalline below about 5 nm in size and exhibit cuboctahedral shape. Larger particles may exhibit lattice defects and shape deviations. The optical properties of these materials correspond to their overall structure of nanoparticulate composites having a very low filling factor of the metal phase. Therefore, the optical spectra are dominated by light scattering contributions of silica nanospheres peaking at about 425 nm. The latter completely cover the surface plasmon resonance of Ag nanoparticles and partly that of Au. With higher metal loadings and increasing particle size, diminishing the effect of resonance damping, the optical absorption reveals the signature of resonances due to metal particles. As long as the coating of oxide nanospheres by metal nanoparticles remains incomplete, this behaviour in principle is not expected to essentially change. Efforts to improve the coating characteristics included the variation of precursor concentration and application of a multi-step procedure. Coverages of about 50% for Ag and even 65% for Au were achieved by using higher metal loading, but this increase was accompanied by a less uniform particle arrangement. Repetition of the incipient wetness impregnation resulted in rather promising coating characteristics for Au if the single-step concentration was appropriately lowered.

In general, it can be concluded, that a low precursor concentration and low temperature approach will be most successful in producing core-shell-like structures. These are thought to evolve finally into regular core-shell structures having novel optical properties via further metal deposition by complementary processes. It may be the task of future studies to explore in more detail the processes of nucleation and growth involved in the formation of the above structures. In particular, it will be important to find out, how both processes may be separately controlled. Another issue is the poor adhesion of metals like Ag and Au on silica. It is worthwhile to spend some effort with improving this behavior since otherwise it could endanger the success of closed shell formation.

Design and fabrication of so-called "metal nanoshells", i.e., core-shell structures consisting of insulating core and metal shell with nanometer dimensions, have been extensively studied in recent years and a number of applications were proposed or even tested. Most of them make use of the enhanced structural tunability of optical resonances from the visible to the infrared as well as from large effects in molecular fluorescent enhancement and surface enhanced Raman scattering. It should be pointed out here that in the field of optical sensors and plasmon waveguides still there are numerous possibilities to replace the use of metal particles of spherical shape by "nanoshells" with greater flexibility of application and control of their optical characteristics. This is valid for biologic applications like detecting DNA or bacteria, but also for technical applications like plasmon waveguides working with ordered arrays of metal particles. Since such core-shell structures

have distinctly larger dimensions than their full-metal counterparts they are more easy to be arranged in two and three-dimensional arrays, serving this way as building blocks of nanostructured materials.

Zusammenfassung und Ausblick

Die vorliegende Dissertation berichtet über eine ausführliche Untersuchung zur Bildung und Charakterisierung von Metallnanopartikel-Beschichtungen auf Oxidnanokugeln. Diese Beschichtungen, die auf die Ausbildung von Kern-Hülle-Strukturen abzielen, sind eine Herausforderung wegen der neuartigen optischen Eigenschaften solcher Strukturren, die innerhalb weiter Grenzen durch Variation von Kerngrösse und Hüllendicke eingestellt werden können. Die experimentelle Realisierung einer entsprechenden Untersuchung erfordert, geeignete Syntheserouten einschliesslich dazu passender Materialien von Kern und Hülle zu erkunden. Der Versuch, Kern-Hülle-Strukturen durch Metallabscheidung auf Oxidnanokugeln zu bilden, wird in mehreren Schritten angenähert. Dabei wird die Festlegung befolgt, dass eine Oberflächen-Kontamination durch funktionalisierende Agentien vermieden werden und eine Behandlung bei moderaten Temperaturen stattfinden soll. Diese Zielstellung wurde in der diesbezüglichen Literatur bisher nicht berücksichtigt.

Die einzelnen Schritte dieser Annäherung betreffen verschiedene Aspekte der komplexen Untersuchung. Einer dieser Aspekte betrifft die eingesetzten Oxidmaterialien, die gewissen Anforderungen genügen sollen. Das sind kurz gesagt: *(i)* die geometrischen Merkmale Grösse und Gestalt, um als Träger für konzentrische Metall- Hüllen zu dienen, *(ii)* die dafür geeignete dielektrische Funktion, und *(iii)* der Zustand der Oberfläche was Oberflächengruppen betrifft, die als reduzierende Radikale dienen können oder als bevorzugte Plätze der Anlagerung von Metallatomen im Zuge der Metallabscheidung mit chemischen Mitteln. Andere Aspekte betreffen den Prozess der Metallabscheidung und die Metalle, für die geeignete Vorläuferverbindungen gefunden werden können. Zu diesem Zweck wurde eine neue Methode der Metall-Beschichtung, die oberflächenvermittelte Reduktion von Metallkomplexen bei niedrigen Temperaturen eingeführt.

Eine Reihe von Oxidmaterialien wurde im Hinblick auf ihre strukturellen Merkmale mittels Elektronenmokroskopie und bezüglich des Gehaltes an Hydroxylgruppen mittels Thermogravimetrischer Analyse untersucht. Leicht erhältliche und preiswerte, mesoporöse, nicht-planare Oxidmaterialien boten den Vorteil einer sehr hohen spezifischen Oberfläche in Verbindung mit einer ziemlich hohen Konzentration an Oberflächenhydroxyl. Obgleich sie nicht für Kern-Hülle-Strukturen geeignet sind, ermöglichten diese Materialien, die Abscheidung von 11 unterschiedlichen Metallen unter Benutzung verschiedener Vorläufer zu testen. Kommerziell erhältliche, polydisperse Oxidmaterialien (SiO_2, $\gamma\text{-}Al_2O_3$, TiO_2, Fe_2O_3) in Form von Nanokugeln wurden getestet, jedoch nur SiO_2 von NANOTEK und TiO_2 von CERAC wiesen eine ausreichend glatte Oberfläche und Kugelgestalt auf, um bei den Experimenten zur Metallabscheidung Verwendung zu finden. Die sehr niedrige Konzentration an Hydroxylgruppen auf der Oberfläche dieser Materialien rührt von ihrer Herstellung mittels Pyrolyseverfahren her. Die beste Wahl zum Zwecke von Kern-Hülle-

Strukturen sind sogenannte "monodisperse" Oxid-Nanokugeln, die genau genommen eine sehr enge Grössenverteilung aufweisen. Neben kommerziell beschafftem Monospher^{TM} SiO$_2$ von MERK, wurden laborgefertigte Stöber-SiO$_2$ Nanokugeln mit mittleren Durchmessern zwischen 100 und 300 nm für Beschichtungs-Experimente mit Metallnanopartikeln benutzt. Diese Materialien haben einen sehr hohen Gehalt an Oberflächen-Hydroxyl. Oxidnanokugeln im obengenannten Grössenbereich sind bestens geeignet für die strukturelle Charakterisierung der Beschichtungsmerkmale mittels Transmissionselektronenmikroskopie.

Drei verschiedene Wege wurden erprobt, um eine Beschichtung von Oxidnanokugeln mit Metallnanoteilchen zu erreichen. Die eine, ausführlich getestet an nicht-planaren Oxiden, besteht im Ersetzen von Hydroxylgruppen durch Aluminium-Wasserstoff- Oberflächenkomplexe, um eine kontrollierte Reduktion von durch Impregnation aus der Lösung aufgebrachten Metallkomplexen zu ermöglichen. Eine nachfolgende Trocknungsprozedur bei 100 bis 300°C resultierte in Metallnanopartikeln, deren Grösse, Grössenverteilung und Konzentration von Metall zu Metall und auch für unterschiedliche Vorläufer des gleichen Metalls variierte. Insgesamt jedoch, wurden sehr kleine Metallpartikel mit Grössen von etwa 2 nm gebildet.

Für Partikel der superparamagnetischen Metalle Ni, Co und Fe wurde Signale der ferromagnetischen Resonanz beobachtet, deren Temperaturabhängigkeit verfolgt wurde, um daraus die entsprechende Partikelgrösse abzuleiten. Bei Partikeln von paramagnetischen Metallen der Gruppe VIIIB interessierte neben den Beschichtungsmerkmalen auch die Leitungselektronen-Spinresonanz. Solche Signale wurden für Rh und Pt beobachtet. Die Einheitlichkeit der Anordnung und Stabilität der Grössendispersion der Pt Partikel ist höchst bemerkenswert. Die Metalle der Gruppe IB Cu, Ag und Au weisen, in dieser Reihenfolge, eine zunehmende Tendenz auf, unter ansonsten vergleichbaren Bedingungen grössere Partikel zu bilden, was zu eine bimodalen Grössenverteilung für das letzte Metall führt. Aus Messungen der magneti- schen Resonanz an Ag und Cu Proben konnten CESR Signale identifiziert werden. Als eine generelle Beobachtung aller nach dieser Syntheseroute präparierten Proben wurden häufig Anzeichen für das Vorliegen von Metallionen sowie auch Signale, die von paramagnetischen Defekten der SiO$_2$ -Oberfläche herrühren, gefunden. Die Defekte können aus einer Re-Oxidation von Metallatomen an restlichen Hydroxylgruppen resultieren, wobei gleichzeitig die Metallionen entstehen.

Die zweite Syntheseroute wurde für polydisperse Oxidnanokugeln unterschiedlicher Herkunft gewählt. Hierbei werden durch Impregnation aus der Lösung aufgebrachte, thermisch labile, organometallische Vorläufer zur Bildung von organometallischen Oberflächenkomplexen benutzt. Da keine weitere reduzierende Behandlung erforderlich ist, eignet sich diese Prozedur sehr gut für die polydispersen Nanokugeln, die nur eine geringe Konzentration an Oberflächenhydroxyl aufweisen. Sie wurde mit zwei unterschiedlichen organometallischen Vorläufern von Pt und Pd für SiO$_2$ und TiO$_2$ benutzt und ergab meistens gleichmässig angeordnete Metallpartikel mit mittleren Grössen von etwa 2.5 nm und enger Grössenverteilung. Bei sehr niedrigen Vorläufer-Konzentrationen verschlechterten sich die Beschichtungsmerkmale von SiO$_2$ auch nach Trocknung bei Temperaturen von 300°C nicht. Bei auf diese Weise hergestellten Pt Nanopartikeln auf

SiO$_2$ Nanokugeln wurde Quantum-Size-Effekt mittels magnetischer Resonanz-Messung (CESR) nachgewiesen. Noch bessere Beschichtungsergebnisse wurde mit hohen Vorläufer-Konzentrationen ganz ohne Anhebung der Temperatur erreicht. Auf TiO$_2$ Nanokugeln war die Einheitlichkeit der Metallpartikelanordnung nicht so gut und die Abscheidung bei niedrigen Temperaturen funktionierte nicht ganz zufriedenstellend. Nichtsdestotrotz kann gefolgert werden, dass die Metallabscheidung mittels organometallischer Vorläufer als Vorbekeimungs-Schritt gut geeignet ist, um Kern-Hülle-Strukturen auf Oxidnanokugeln mit geringem Hydroxylgehalt zu erzeugen.

Monodisperse SiO$_2$ Nanokugeln mit relativ hohem Gehalt an Oberflächen-Hydroxylgruppen boten sich für einen dritten Syntheseweg an. Dieser oberflächen-vermittelte Prozess nutzt die Fähigkeit von terminierenden Gruppen zur Reduktion von Metallionen der mittels einer Inzipient-Wetness-Imprägnierung aufgebrachten Vorläuferverbindungen. Er wurde für eine systematische Untersuchung der Beschichtungsmerkmale von Ag und Au Nanopartikeln eingesetzt. Die generellen Strukturmerkmale sind für beide Metalle ganz gleichartig. Eine dichte Population von einheitlich angeordneten ziemlich kleinen Partikeln bedeckt die SiO$_2$ -Nanokugeln nach Trocknung bei Temperaturen um 70°C. Die Bildung von Metallpartikeln auf Oxidträgern bei so niedrigen Temperaturen wird hier zum ersten Mal berichtet. Unter etwa 5 nm Grösse sind die Partikel einkristallin und zeigen eine kuboktaedrische Gestalt. Grössere Partikel können Facettierungen und Gestaltsabweichungen aufweisen. Die optischen Eigenschaften dieser Materialien entsprechen ihrem Gesamtaufbau als nanopartikulate Komposite mit sehr niedrigem Füllfaktor der Metallphase. Deshalb werden die optischen Spektren durch Lichtstreubeiträge von SiO$_2$ Nanokugeln mit Maximum bei etwa 425 nm dominiert. Letztere überdecken komplett die Oberflächenplasmonenresonanz von Ag Nanopartikeln und teilweise auch die von Au. Mit höherer Metallbeladung und zunehmender Partikelgrösse verringert sich der Effekt der Resonanzdämpfung und die optische Absorption zeigt Signaturen der von Metallpartikeln herrührenden Resonanzen. Solange die Beschichtung der Oxidnanokugeln mit Metallnanopartikeln unvollständig bleibt, ist eine Änderung dieses Verhaltens prinzipiell nicht zu erwarten. Die Bemühungen zur Verbesserung der Beschichtungsmerkmale schliessen die Variierung der Vorläuferkonzentration und Anwendung einer Mehrschritt-Prozedur ein. Bedeckungen von 50% für Ag und sogar 65% für Au wurden durch Anwendung einer höheren Metallbeladung erreicht, aber diese Zunahme wurde von einer weniger einheitlichen Partikelanordnung begleitet. Die Wiederholung der Inzipient-Wetness-Imprägnierung ergab vielversprechende Beschichtungsmerkmale für Au, wenn die Einzelschritt-Konzentration geeignet erniedrigt wurde.

Ganz allgemein kann geschlussfolgert werden, dass eine Annäherung mit niedriger Vorläufer-konzentration und niedriger Temperatur für die Herstellung von kern- hülle-artigen Strukturen am erfolgreichsten ist. Durch weitere Metallabscheidung mittels komplementärer Prozesse wird deren Entwicklung zu regulären Kern-Hülle-Strukturen mit neuartigen optischen Eigenschaften angenommen. Es wird die Aufgabe von künftigen Untersuchungen sein, die bei der Bildung der obigen Strukturen beteiligten Prozesse von Keimbildung und Wachstum detaillierter zu untersuchen. Insbesondere wird es wichtig sein herauszufinden, wie beide Prozesse separat gesteuert

werden können. Eine andere Frage ist die der schlechten Adhäsion von Metallen wie Ag und Au auf SiO_2. Es verdient einigen Aufwand, dieses Verhalten zu verbessern, da ansonsten der Erfog der Bildung von geschlossenen Hüllen in Frage steht.

Design und Herstellung von sogenannten "Metall-Nanoshells", das sind Kern- Hülle-Strukturen mit isolierendem Kern und Metallhülle in Nanometerabmessungen wurden in den letzten Jahren ausführlich untersucht und es wurde eine Reihe von Anwendungen vorgeschlagen oder sogar getestet. Die meisten von ihnen machen von der erhöhten strukturellen Einstellbarkeit der optischen Resonanzen vom sichtbaren bis zum infraroten Bereich Gebrauch, sowie auch von grossen Effekten bei der molekularen Fluoreszenzerhöhung und der oberflächen-erhöhten Ramanstreuung. Es sollte hier betont werden, dass auf dem Gebiet der optischen Sensoren und Plasmonen-Wellenleiter noch zahlreiche Möglichkeiten bestehen, die Verwendung von Metallpartikeln mit Kugelgestalt durch "Nanoshells" mit größerer Flexibilität der Anwendung und Einstellung ihrer optischen Eigenschaften zu ersetzen. Das gilt für biologische Anwendungen wie die Detektierung von DNA oder Bakterien, und ebenso für technische Anwendungen wie Plasmon-Wellenleiter, die mit strukturierten Anordnungen von Metallpartikeln arbeiten. Da solche Kern-Hülle-Strukturen deutlich grössere Abmessungen als ihre Ganzmetall-Gegenstücke haben, können sie einfacher in zwei oder dreidimensionale Anordnungen gebracht werden und auf diese Weise als Bausteine für nanostrukturierte Materialien dienen.

8 Acknowledgements

Many people around me helped directly or indirectly to make this work a succes. I am grateful to all of them. If I forgot somebody, this is not because I do not appreciate them, it is only because it is human to forget and I ask them to forgive me.

First of all, I want to thank my wife, Dr. Manuela Miclea for continuous help over these years, for being on my side at the times of special effort in writing this thesis as well as for moral and technical support. Special thanks are given to my parents for offering me the possibility to study at the University.

I would like to thank to Prof. Dr. Ulrich Gösele for offering me the opportunity to work as a researcher in his department in the Max Planck Institute and to be able to finish this work.

Special thanks are given to my supervisors Doz. Dr. Manfred Dubiel and Dr. Herbert Hofmeister who helped me since I started my work at the Max Planck Institute of Microstructure Physics. Part of my knowledge are due to Dr. Herbert Hofmeister and to the challenge which he continuously posed in me. All scientific discussions and coordination of my work made by him were very useful and helpful for me.

I am also grateful to Prof. Dr. Helmut Drevs and Mrs. Katrin Lehrack from College Merseburg, Department of Chemistry and Environmental Engineering for preparation of samples and discussons concerning the chemistry of organometallics.

My special thanks are goes to Dr. Wolfgang Mörke from Martin Luther University, Departament of Chemistry, Institute for Analytics and Environmental Chemistry in helping me to understand and perform the electron magnetic resonance measurements and for preparation of silica nanospheres. I appreciate very much his friendship and human qualities.

Many thanks to my colleagues Christian Mohr, Jörg Schilling and Kornelius Nielsch for their friendly attitude and permanent support, to Dr. Norbert Engler, Dr. Frank Müller and Dr. Ralf Wehrspohn for helping me in developing the programms and for scientific disscusions and also for helping me in learning german language.

I am very grateful to my professors from the University of Bucharest, Faculty of Phyiscs, Department of Electronics and Biophysics, especially to Conf. Dr. Liviu Giurgiu, Conf. Dr. Nicolae Gherbanovski and Lect. Dr. Mihai P. Dinca for their professionalism and permanent care for students.

Last but not least to all my Roumanian collegues and friends from the Max Planck Institute which supported me day by day my sincere "*multumesc*".

Bibliography

[Ade51]   A. Aden and M. Kerker, *Scattering of electromagnetic waves from two concentric spheres*, J. Appl. Phys. **22**, (1951) 1242–1245.

[And75]   J. R. Anderson, *Structure of metallic catalysts*, Academic Press, New York (1975).

[Ash76]   N. W. Ashcroft and N. D. Mermin, *Solid state physics*, Harcourt College Publ., Fort Worth (1976).

[Bet87]   H. Bethge and J. Heydenreich, *Electron microscopy in solid state physics*, Elsevier Science Pub. (1987).

[Bha85]   R. Bhandari, *Scattering coefficients for a multilayered sphere: analytic expressions and algorithms*, Appl. Opt. **24**, (1985) 1960–1967.

[Bia78]   R. S. d. Biasi and T. Devezas, *Anisotropy field of small magnetic particles as measurement by resonance*, J. Appl. Phys. **49**, (1978) 2466–2469.

[Bog99]   N. E. Bogdanchikova, V. P. Petranovskii, R. M. Machorro, Y. Sugi, V. M. G. Soto, and S. M. Fuenes, *Stability of silver clusters in mordenites with different SiO_2/Al_2O_3 molar ratio*, Appl. Surf. Sci. **150**, (1999) 58–64.

[Boh98]   K. F. Bohren and D. R. Huffman, *Absorption and scattering of light by small particles*, John Wiley & Sons Inc. (1998).

[Bon88]   L. Bonneviot and G. L. Haller, *EPR characterizations of Ti^{3+} ions at the metal-support interface in Pt/TiO_2 catalysts*, J. Catal. **113**, (1988) 96–105.

[Bor81]   J. P. Borel, *Thermodynamical size effect and the structure of metallic clusters*, Surf. Sci. **106**, (1981) 1–9.

[Bor86]   Y. Borensztein, P. D. Andrès, R. Monreal, T. Lopez-Rois, and F. Flores, *Blue shift of the dipolar plasma resonance in small silver particles on an alumina surface*, Phys. Rev. B **33**, (1986) 2828–2830.

[Bra00]   M. M. Branda, R. A. Montani, and N. J. Castellani, *The distribution of silanols on the amorphous silica surface: a Monte Carlo simulation*, Surf. Sci. **446**, (2000) L89–L94.

[Bro00]   K. Brown, D. G. Walter, and M. J. Natan, *Seeding of Au nanoparticle solution. 2 Improved control of particle size and shape*, Chem. Mater. **12**, (2000) 306–313.

[Bru35]   D. A. G. Bruggeman, *Berechnung verschidener physikalischer Konstanten von heterogenen Substanzen. I. Dielektrizitätskonstanten und Leitfähigkeiten der Mischkörper aus isotropen Substanzen*, Ann. Phys.(Leipzig) **24**, (1935) 636–679, in german.

[Bäu99]   M. Bäumer and H. J. Freund, *Metal deposition on well-ordered oxide films*, Prog. Surf. Sci. **61**, (1999) 127–198.

[Bur98]   F. Burmeister, C. Schäfle, B. Keilhofer, C. Bechinger, J. Boneberg, and P. Leiderer, *From mesoscopic to nanoscopic surface structures: lithography with colloid monolayers*, Adv. Mat. **10**, (1998) 495–497.

[Bur99]   F. Burmeister, W. Badowsky, T. Braun, S. Wieprich, J. Boneberg, and P. Leiderer, *Colloid monolayer lithography - A flexible approach for nanostructuring of surfaces*, Appl. Surf. Sci. **144-145**, (1999) 461–466.

[Bur00]   F. Burmeister, J. Boneberg, and P. Leiderer, *Mit Kapillarkräften zu Nanostrukturen*, Phys. Bl. **56**, (2000) 49–51, in german.

[Cam97]   C. T. Campbell, *Ultrathin metal films and particles on oxide surfaces: srtuctural, electronic and chemisorptive properties*, Surf. Sci. Rep. **27**, (1997) 1–111.

[Châ85]   A. Châtelain, P. Buffat, P. Stadelmann, and R. A. Weeks, *Precipitation of small iron particles in amorphous silica: ferromagnetic resonance experiments*, J. Non-Cryst. Solids **71**, (1985) 335–344.

[Cla97]   P. Claus, S. Schimpf, R. Schödel, W. Mörke, and D. Hönicke, *Hydrogenation of crotoaldehyde on Pt/TiO$_2$ catalysts: Influence of the phase composition of titania on activity and itramolecular selectivity*, Appl. Catal. A **165**, (1997) 429–441.

[Cla00]   P. Claus, A. Brückner, C. Mohr, and H. Hofmeister, *Supported gold nanoparticles from quantum dot to mesoscopic size scale: Effect of electronic and structural properties on catalytic hydrogenation of conjugated functional groups*, J. Am. Chem. Soc. **122**, (2000) 11 430–11 439.

[deC95]   D. deCaro, V. Agelou, A. Duteil, B. Chaudet, R. Mazel, C. Roucau, and J. S. Bradley, *Preparation from organometallic precursors, characterization and some reactivity of cooper and gold collids sterically protected by nitrocellulose, polyvinivpyrrolidone, or polydimethyl phenyl oxide*, New J. Chem. **19**, (1995) 1265–1274.

[Dok99]   A. Dokoutchaev, J. T. James, S. C. Koene, S. Pathak, G. K. S. Prakash, and M. E. Thornpson, *Colloidal metal deposition onto functionalized polystyrene microspheres*, Chem. Mater. **11**, (1999) 2389–2399.

[Dor97]   J. L. Dorman, D. Fioriani, and E. Tronc, *Magnetic relaxation in fine particle system*, Adv. Chem. Phys. **XCVIII**, (1997) 283–494.

[Dre98]   H. Drevs, W. Mörke, J. Jarsetz, T. Bieruta, and H. Hofmeister, *Characterisation of nanosized nickel prepared by reactions of Ni-σ-organyl complexes on silica. An electron paramagnetic and ferromagnetic resonance study*, Appl. Organomet. Chem. **12**, (1998) 312–325.

[Dre02]   H. Drevs, K. Lehrack, and E. Hecht, *Synthesis and crystal structure of lithiumtetraphenylplatinate(II) and -palladate(II)*, J. Organometal. Chem. In preparation.

[Dwy53]   F. P. Dwyer and A. M. Sargeson, *The preparation of tris-acetylacetone-Rhodium (III) and tris-acetyacetone-Iridium (III)*, J. Am. Chem. Soc. **75**, (1953) 984 – 985.

[Dyr97] K. Dyrek and M. Che, *EPR as tool to invesigate the transition metal chemistry on oxide surfaces*, Chem. Rev. **97**, (1997) 305–331.

[Edi91] J. W. Edington, *Practical electron microscopy in materials science*, TechBooks (1991).

[Fed93] S. Fedrigo, W. Harbich, and J. Buttet, *Collective dipole oscillations in small silver clusters embedded in rare-gas matrices*, Phys. Rev. B **47**, (1993) 10 706–10 715.

[Fuj00] M. Fuji, S. Ueno, T. Takei, T. Watanabe, and M. Chikazawa, *Surface structural analysis of fine silica powder modified with butyl alcohol*, Coll. Polym. Sci **270**, (2000) 30 –36.

[Gan15] R. Gans, Annal.Phys. **47**, (1915) 270.

[Gie94a] H. Giesche, *Synthesis of monodispersed silica powders. I. Particle properties and reaction kinetics*, J. Eur. Cer. Soc. **14**, (1994) 189–204.

[Gie94b] H. Giesche, *Synthesis of monodispersed silica powders. II. Controlled growth reaction and continuous production process*, J. Eur. Cer. Soc. **14**, (1994) 205–214.

[Gie97] M. Giersig, L. M. Liz-Marzán, T. Ung, D. Su, and P. Mulvaney, *Chemistry of nanosized silica-coated metal particles - EM study*, Ber. Bunsenges. Phys. Chem. **101**, (1997) 1617 – 1620.

[Gie00a] M. Giersig and M. Hilgendorf, *Ordered colloidal magnetic particles by magnetophoretic deposition*, volume Cluster and nanostructure interface, 203–208, World Scientific Publ. (2000).

[Gie00b] H. Giesche, *Fine Particles, Synthesis, Characterisation and Mechanism of growth*, chapter 2.1, 126–146, Marcel Dekker, New York (2000).

[Gle95] H. Gleiter, *Nanostructured materials: state of art and perspectives*, NanoStructured Mater. **6**, (1995) 3–14.

[Gom00] S. Gomez, K. Philippot, V. Colliere, B. Chaudet, F. Senacq, and P. Lecante, *Gold nanoparticles from self-assembled gold(I) amine precursors*, Chem. Commun. **19**, (2000) 1945–1946.

[Gon99] F. Gonella, F. Caccavale, L. D. Bogomolova, and V. A. Jachkin, *Application of electron paramagnetic resonance to the study of Cu^{2+} ions in Cu-Na ion-exchanged glasses*, Appl. Phys. A **68**, (1999) 1–8.

[Gor77] D. A. Gordon, R. F. Marzke, and W. S. Glaunsinger, *Size distribution and ESR of uniform microcrystals of platinum*, J. de Physique Col. C2 **38**, (1977) 87–91.

[Gra76] C. G. Granqvist and R. A. Buhrman, *Ultrafine metal particles*, J. Appl. Phys. **47**, (1976) 2200–2222.

[Gra77] C. G. Granqvist and o. Hunderi, *Optical properties of ultrafine gold particles*, Phys. Rev. B **16**, (1977) 3513–3534.

[Gri81] D. L. Griscom, *Particle size effects in the FMR spectra of fine-grained precipitates in glass*, IEEE Trans. Magn. **Mag-17**, (1981) 2718–2719.

[Gri84]   D. L. Griscom, *Electron spin resonance studies of trapped hole centres in irradiated alkali silicate glasses: a critical comment on current models for HC_1 and HC_2*, J. Non-Cryst. Solids **64**, (1984) 229–247.

[Güt52]   A. Güttler, *Die Miesche Theorie der Beugung durch dielektrische Kugeln mit absorbierendem Kern und ihre Bedeutung für Probleme der intersellare Materie und atmosphärischen Aerosols*, Ann. Phys. **11**, (1952) 65–98, in german.

[Gun97]   P. L. J. Gunter, J. W. Niemantsverdriet, F. H. Riberio, and G. A. Somorjai, *Surface science approach to modeling supported catalysts*, Catal. Rev. - Sci. Eng. **39**, (1997) 77–168.

[Hal86]   W. P. Halperin, *Quantum size effects in metal particles*, Rev. Mod. Phys **58**, (1986) 533–606.

[Hen98]   C. R. Henry, *Growth, structure and morphology of supported metal clusters studied by surface science techniques*, Cryst. Res. Technol. **33**, (1998) 1119–1140.

[Hod00]   J. H. Hodak, A. Henglein, and G. V. Hartland, *Photophysics of nanometer sized metal particles: Electron-phonon coupling and coherent excitation of breathing vibrational modes*, J. Phys. Chem. B **104**, (2000) 9954 –9965.

[Hof82a] H. Hofmeister, H. Haefke, and M. Krohn, *Habit of gold particles vapor-deposited onto silver bromide films*, J. Cryst. Growth **58**, (1982) 507–516.

[Hof82b] H. Hofmeister, H. Haefke, and A. Panov, *Growth of gold particles vapor-deposited onto silver bromide films*, J. Cryst. Growth **58**, (1982) 500–506.

[Hof98]   H. Hofmeister, *Forty Years study of fivefold twinned structures in small particles and thin films*, Cryst. Res. Tech. **33**, (1998) 3–25.

[Hof01]   H. Hofmeister, F. Huisken, B. Kohn, R. Alexandrescu, S. Cojocaru, A. Crunteanu, I. Morjan, and L. Diamandescu, *Filamentary iron nanostructures from laser-induced pyrolysis of iron pentacarbonyl and etylene mixtures*, Appl. Phys. A **71**, (2001) 7 – 11.

[Hof02]   H. Hofmeister, P. T. Miclea, and W. Mörke, *Metal nanoparticle coating of oxide nanospheres for core-shell structures*, Particle and Particle Systems Charact. In preparation.

[Hua97]   W. C. Huang and J. T. Lue, *Optical properties of quantum confined small metallic particles with diffuse surface*, J. Phys. Chem. Solids **58**, (1997) 1529–1538.

[Höv93]   H. Hövel, S. Fritz, A. Hilger, U. Kreibig, and M. Vollmer, *Width of cluster plasmon resonances: bulk dielectric functions and chemical interface damping*, Phys.rev. B **48**, (1993) 18 178–18 188.

[Jai75]   S. C. Jain, N. D. Arora, and T. R. Reddy, *Conduction electron spin resonance of colloidal silver particles in KCl crystals*, Phys. Lett. **54A**, (1975) 53–54.

[Jan01]   N. R. Jana, L. Gearheart, and C. J. Murphy, *Seed-mediated growth approach for shape-controlled synthesis od spheroidal and rod-like gold nanoparticles using surfactant template*, Adv. Mater. **13**, (2001) 1389–1392.

[Ji01]   T. Ji, V. G. Lirtsman, Y. Avny, and D. Davidov, *Preparation, characterization, and application of Au-shell/polystirene beads and Au-shell/magnetic beads*, Adv. Mater. **13**, (2001) 1253 – 1256.

[Joh99]   C. Johansson, T. Aklint, M. Hanson, M. Andersson, N. Tarras-Wahlberg, E. Olsson, B. Kalska, R. Wappling, and A. Rosen, *Deposited nano-meter sized iron clusters*, NanoStructured Mater. **12**, (1999) 287 – 290.

[Kat79]   J. R. Katzer, G. C. A. Schuit, and J. H. C. v. Hooff, *Paramagnetic platinum and oxygen species an supported platinum*, J. Catal. **59**, (1979) 278–292.

[Kaw70] A. Kawabata, *Electronic properties of fine metallic particles. III. ESR absorption line shape*, J. Phys. Soc. Jpn. **29**, (1970) 902–904.

[Köh98]   K. Köhler, W. Mörke, and T. Bieruta, *Magnetic resonance (FRM, EPR) of chromium dioxide supported on titania*, Colloids and Surfaces A **144**, (1998) 81–87.

[Kha00]   A. K. Khattak, M. Afzal, M. Saleem, G. Yasmeen, and R. Ahmad, *Surface modifications of alumina by metal doping*, Colloids and Surfaces A **162**, (2000) 99–106.

[Kis99]   L. B. Kiss, J. Söderlung, G. A. Niklasson, and C. G. Granqvist, *New approach to the origin of lognormal size distribution of nanoparticles*, Nanotechnology **10**, (1999) 25–28.

[Kit96]   C. Kittel, *Introduction to solid state physhics*, John Wiley and Sons, Inc., New York (1996).

[Knö78]   H. Knözinger and P. Ratnasamy, *Catalytic aluminas: Surface models and characterization of surface sites*, Catal. Rev. - Sci. Eng. **17**, (1978) 31–70.

[Kos00]   M. Kosmulski, P. Eriksson, C. Brancewicz, and J. B. Rosenholm, *Zeta potentials of monodispersed, spherical silica particles in mixed solvents as a function of cesium chloride concentration*, Colloids and Surfaces A **162**, (2000) 37 – 48.

[Kou82]   M. Koudelka, J. Sanchez, and J. Augustynski, *Electrochemical and surface characteristics of the photocatalytic platinum deposits on TiO_2*, J. Phys. Chem. **86**, (1982) 4277–4180.

[Kre70]   U. Kreibig, *Kramers Kronig analysis of the optical properties of small silver particles*, Z. Phys. **234**, (1970) 307–318.

[Kre74]   U. Kreibig, *Electronic properties of small silver particles: the optical constant and their temperature dependence*, J. Phys. F **4**, (1974) 999–1014.

[Kre95]   U. Kreibig and M. Vollmer, *Optical Properties of Metal Clusters*, Springer-Verlag, Berlin (1995).

[Kre97a] U. Kreibig, *Handbook of optical properties*, volume II Optics of small particles, interfaces, and surfaces, chapter Optics on nanosized materials, 145–190, CRC Press (1997).

[Kre97b] U. Kreibig, M. Gratz, and A. Hilger, *Mie resonances: Sensors for physical and chemical cluster interface properties*, Ber. Bunsenges. Phys. Chem. **101**, (1997) 1593–1604.

[Kub62]   R. Kubo, *Electronic properties of fine metllic particles. I.*, J. Phys. Soc. Jpn **17**, (1962) 975–986.

[Kub84]   R. Kubo, A. Kawabata, and S. Kobayashi, *Electronic properties of small particles*, Ann. Rev. Mater. Sci **14**, (1984) 49–66.

[Li95]   X. Li and M. A. Vannice, *ESR studies of well-dispersed Ag crystallites on SiO_2*, J. Catal. **151**, (1995) 87–95.

[Lov71]   D. Loveridge and S. Parke, *Electron spin resonance of Fe^{3+}, Mn^{2+}, and Cr^{3+} in glasses*, Phys. Chem. Glasses **12**, (1971) 19.

[Lue01]   J. T. Lue, *A review of characterization and physical property studies of metallic nanoparticles*, J. Phys. Chem. Solids **62**, (2001) 1599 – 1612.

[May00]   A. B. R. Mayer, W. Grebner, and R. Wannemacher, *Preparation of silver-latex composites*, J. Phys. Chem. B **104**, (2000) 7278–7285.

[MC97]   J. M. Montejano-Carrizales, F. Aguilera-Granja, and J. L. Móran-López, *Direct enumeration of the geometrical characteristics of clusters*, NanoStructured Materials **8**, (1997) 269–297.

[MG04]   J. C. Maxwell-Garett, *Colors in metel galsses and in metallic films*, Philos. Trans. R. Soc. London **A203**, (1904) 385 – 420.

[Mic00]   P. T. Miclea, W. Mörke, K. Lehrack, H. Drevs, and H. Hofmeister, *Metal nanoparticles by direct reduction on non-planar silica substrates*, Proc.Autumn School on Material Science and Electron Microscopy **Berlin**, (2000) 360–361.

[Mie08]   G. Mie, *Beiträge zur Optik trüben Medien, speziell kolloidaler Metallösungen*, Ann. Phys. **25**, (1908) 377–445, in german.

[Mit98]   G. Mitrikas, C. C. Trapalis, N. Boukos, V. Psyharis, L. Astrakas, and G. Kordas, *Size distribution and EPR of silver nanoparticles in SiO_2 matrix*, J. Non-Cryst. Solids **224**, (1998) 17–22.

[Mit01]   G. Mitrikas, C. C. Trapalis, and G. Kordas, *Tailoring the particle size of sol-gel derived silver nanoparticles in SiO_2*, J. Non-Cryst. Solids **286**, (2001) 41–50.

[Mon71]   R. Monot, A. Châtelain, and J. P. Borel, *Conduction electron spin resonance in small particles of pure gold*, Phys. Lett. **34A**, (1971) 57–58.

[Mor80]   A. Morrish, *The physical principles of magnetism*, Robert E. Krieger Publ. Company, Inc. Hungtington, New York (1980).

[Mör90]   W. Mörke, M. Hirschfelder, S. Gehre, and K. Doerffel, *Algorithm for the determination of avarege particle size and number of superparamagnetic crystallites from dynamic susceptibility measurements (Ferromagnetic resonance)*, Chemometrics and Intelligent Laboratory Systems **8**, (1990) 87–90.

[Mör94]   W. Mörke, R. Lambert, U. Schubert, and B. Breitscheidel, *Metal complexes in inorganic matrices. 11. Composition of highly dispersed bimetalic Ni, Pd alloy particles prepared by sol-gel proccesing: electron microscopy and ferromagnetic resonance study*, Chem. Mater. **6**, (1994) 1659–1666.

[Mör96]   W. Mörke, T. Bieruta, J. Jarsetz, C. Görsmann, and U. Schubert, *Characterisation of highly dispersed bimetallic Ni-Cu alloy particles by ferromagnetic resonance*, Colloids and Surfaces A **115**, (1996) 303–309.

[Née49]   M. L. Néel, *Théorie du trainage magnétique des ferromagnétiques en grains fins avec applications aux terres cuites*, Annal. Geophys. **5**, (1949) 99–136, in french.

[Nor78]   S. Norrman, T. Andersson, and C. G. Granqvist, *Optical properties of discontinuous gold films*, Phys. Rev. B **18**, (1978) 674–695.

[Oki96]   K. Okitsu, H. Bandow, and Y. Maeda, *Sonochemical preparation of ultrafine palladium particles*, Chem. Mater. **8**, (1996) 315–317.

[Old98]   S. J. Oldenburg, R. D. Averitt, S. L. Westcott, and N. J. Halas, *Nanoengineering of optical resonances*, Chem. Phys. Lett. **288**, (1998) 243–247.

[Ott61]   M. Otter, *Temperaturabhängigkeit der optischen Konstanten massiver Metalle*, Z. Phys. **161**, (1961) 539–549, in german.

[Pak62]   G. E. Pake, *Paramagnetic resonance - An introduction monograph*, W. A. Benjamin, Inc., New York (1962).

[Pal98]   B. Palpant, B. Prével, J. Lermé, E. Cottancin, M. Pellarin, M. Treilleux, A. Perez, and M. Vialle, J. L.and Broyer, *Optical properties of gold clusters in the size range* $2 - 4$ *nm*, Phys. Rev. B **57**, (1998) 1963–1970.

[Per60]   J. B. Peri and R. B. Hannan, *Surface hydroxyl groups on* $\gamma - Alumina$, J. Phys. Chem. **64**, (1960) 1526–1530.

[Pil01]   M. P. Pileni, *Self-assemblies of nanocrystals: fabrication and collective properties*, Appl. Surf. Sci. **171**, (2001) 1–14.

[Por97]   J. Porstendorfer, *Numerische Berechnung von Extinctions- und Streuspektren sphäroidaler Metallpartikel belibiger Größe in dielektrischer Matrix*, Dissertation, Martin Luther Universität Halle (Saale), in german (1997).

[Rim00]   D. S. Rimai, D. J. Quesnel, and A. A. Busnaina, *The adhesion of dry particles in the nanometer to micrometer-size range*, Colloids and Surfaces A **165**, (2000) 3 – 10.

[Rog00]   A. Rogach, A. Susha, F. Caruso, G. Sukhorukov, A. Kornowski, S. Kershaw, H. Möhwald, A. Eychmüller, and H. Weller, *Nano- and microengineering: Three-dimensional colloidal photonic crystals prepared from submicrometer-sized polystyrene latex spheres pre-coated with luminescent polyelectrolyte/nanocrystal shells*, Adv. Mater. **12**, (2000) 333–337.

[Rud81]   G. Rudakoff, W. Vogelsberger, S. Döring, R. Töpel, G. Müller, C. und Diekers, and J. Miesel, *Eine volumetrische Methode zur Bestimmung der Silanolgruppenkoncentrazion amorpher Kieselsäuren*, Wiss. Ztschr. Friedrich-Schiller-Univ. Jena Math.-Naturwiss. **30**, (1981) 569–577, in german.

[Sab00]   R. Sabia and L. Ukrainczyk, *Surface chemistry of* SiO_2 *and* TiO_2-SiO_2 *glasses as determined by titration of soot particles*, J. Non-Cryst. Solids **277**, (2000) 1–9.

[Sau01] T. K. Sau, A. Pal, N. R. Jana, Z. L. Wang, and T. Pal, *Size controlled synthesis of gold nanoparticles using photochemically prepared seed particles*, J. Nanopart. Res. **3**, (2001) 257–261.

[Sch58] E. Schlömann, *Ferromagnetic resonance in polycrystalline ferrites with large anisotropy .I.*, J. Phys. Chem. Solids **6**, (1958) 257–266.

[Sch00] S. Schwarz, K. Lunkwitz, B. Keßler, U. Spiegler, E. Killmann, and W. Jaeger, *Adsorption and stability of colloidal silica*, Colloids and Surfaces A **163**, (2000) 17 – 27.

[Set94] S. A. Sethi, M. S. Pedersen, A. R. Thölén, and S. Morup, *Formation and phase analysis of surface oxides on ultrafine particles of Fe*, volume Nanophase materials, 81–84, Kluwer Acad. Publ. (1994).

[Sha81] V. K. Sharma and A. Baiker, *Superparamagnetic effects in the ferromagnetic resonance of silica supported nickel particles*, J. Chem. Phys. **75**, (1981) 5596–5601.

[Stö68] W. Stöber, A. Fink, and E. Bohn, *Controlled growth of monodisperse silica spheres in the micron size range*, J. Coll. Interf. Sci. **26**, (1968) 62 –69.

[Sur73] G. Suran, A. Stankoff, and F. Hoffmann, *Ferromagnetic resonance in polycrystalline magnetostrictive films with large isotropic planar strain*, Phys. Rev. B **8**, (1973) 1109–1118.

[Tem00] A. C. Templeton, J. J. Pietron, R. W. Murray, and P. Mulvaney, *Solvent Refractive index and core charge influences on the surface plasmon absorbance of alkanethiolate monolayer-protected gold clusters*, J. Phys. Chem. B **104**, (2000) 564–570.

[Vee89] J. A. R. v. Veen, *An enquiry into the surface chemistry of TiO_2 (Anatase)*, Z. Phys. Chem **162**, (1989) 215–229.

[Ver99] M. Verelst, T. O. Ely, C. Amiens, E. Snoeck, P. Lecante, A. Mosset, M. Respaud, J. M. Broto, and B. Chaudet, *Synthesis and characterisation of CoO, Co_3O_4, and mixed Co/CoO nanoparticles*, Chem. Mater. **11**, (1999) 2702–2708.

[Vid99] O. Vidoni, K. Philippot, C. Amiens, B. Chaudet, O. Balmes, J. O. Malm, J. O. Bovin, F. Senocq, and M. J. Casanove, *Novel, sponge-like ruthenium particles of controllable size stabilized only by organic solvents*, Angew. Chem. Int. Ed. **38**, (1999) 3736–3738.

[Wan00] Z. L. Wang, *Characterization of nanophase materials*, Wiley-VCH, New York (2000).

[Wel00] J. D. Wells, L. K. Koopal, and A. d. Keizer, *Monodisperse, nonporous, spherical silica particles*, Colloids and Surfaces A **166**, (2000) 171 –176.

[Wes98a] A. R. West, *Solid state chemistry and its applications*, John Wiley and Sons, New York (1998).

[Wes98b] S. L. Westcott, S. J. Oldenburg, T. R. Lee, and N. J. Halas, *Formation and adsorbtion of clusters of gold nanoparticles onto functionalized silica nanoparticle surfaces*, Langmuir **14**, (1998) 5396–5401.

[Whi76] L. K. White and R. L. Belford, *Quadrupole coupling constants and square-planar Copper(II)-sulfur complexes from single-crystal electron paramagnetic resonance spectroscopy*, J. Am. Chem. Soc. **98**, (1976) 4428–4438.

[Wil96]   D. B. Williams and C. B. Carter, *Transmission electron microscopy - A textbook for material science*, Plenum Press (1996).

[Wis79]   W. J. Wiscombe, *Mie scattering calculations: advances in technique and fast, vector-speed computer codes*, NCAR Technical Note 1–64, republished in 1996.

[Wyr99]   R. Wyrwa and H. Görls, *Ungewönliche Molekülstrukturen für Platin(II)-at-Komplexe*, Z. Anorg. Allg. Chem. **625**, (1999) 1904–1907, in german.

[Yac80]   M. J. Yacamán, *New techniques for electron microscopy characterisation of small metal particles*, volume Growth and properties of small clusters, 225 – 232, Elsevier Science Publ (1980).

[Yok89]   H. Yokoi, A. Kadowaki, and S. Ikoma, *The preparation of stable colloidal polyvinyl-alcohol composites of Cu_2O and Cu*, Bull. Chem. Soc. Japan **62**, (1989) 1698–1700.

[Yon91]   Y. Yonezawa, T. Sato, S. Kurota, and K. Kuge, *Photochemical formation of colloidal silver - petizing action of acetone ketyl radical*, J. Chem. Soc. Farad. Trans **87**, (1991) 1905–1910.

[Zak01]   M. I. Zaki, M. A. Hasan, F. A. Al-Sagheer, and L. Pasupulety, *In situ FTIR spectra of pyridine absorbed on SiO_2-Al_2O_3, TiO_2, and CeO_2: general considerations for the identification of acid sites on surfaces of finely divided metal oxides*, Colloids and Surfaces A **190**, (2001) 261–274.

[Zha96]   X. Q. Zhao, B. X. Liu, Y. Liang, and Z. Q. Hu, *Oxidation behaviour and magnetic properties of metalic ultrafine particles*, J. Mag. Magn. Mater. **164**, (1996) 401–410.

[Zho93]   H. S. Zhou, I. Honma, H. Komiyama, and J. W. Haus, *Quantum size effect in metal coated nanoparticles*, in *Mat. Res. Soc. Symp. Proc.*, volume 283, 939–944 (1993).

[Zhu00]   L. T. Zhuravlev, *The surface chemistry of amorphous silica. Zhuravlev model*, Colloid. Surf. A **173**, (2000) 1–38.

[Zou93]   R. D. Zou, W. Gonzalez, *Stabilization and the sintering of porous Pt/SiO_2: A new approach*, Appl. Catal. A **102**, (1993) 181–200.

A Eidesstattliche Erklärung

Ich erkläre, dass ich keine anderen als die von mir angegebenen Quellen und Hilfsmittel zur Erstellung meiner Dissertation verwendet habe. Den benutzten Werken wörtlich oder inhaltlich entnommene Stellen sind als solche gekennzeichnet.

Paul- Tiberiu Miclea

Halle / Saale, im Januar 2002

B Curriculum Vitae

PERSONAL DATA

Name:	MICLEA
First name:	PAUL-TIBERIU
Permanent address:	2 Sureanu Str., Apt.8, Sibiu, Jud. Sibiu, ROMANIA
Date of birth:	January 23, 1971
Place of birth:	Petrosani, Jud. Hunedoara, Romania
Sex:	Male
Citizenship:	Romanian
Marrital status:	Married
Military stage:	Satisfied (1990)

EDUCATION

1985-1989: High School No.4, Sibiu

June 1989: Graduation of high school

1991-1996: Faculty of Physics, Bucharest University

June 1996: Graduation with title Licentiate in Physics (GPA: 9.46),
major in Electronic Physics Diploma Thesis:
"*Study of cyclotronic resonance in a hot cathode discharge*"
under the leadership of Conf. Dr. N.Gherbanovschi

1996-1997: Faculty of Physics, Bucharest University, preparation of MS degree

June 1997: Graduation with title Master of Science degree (GPA:10),
specialty Electronic Physics, Dissertation Thesis:
"*Electronic system for measuring and controlling the deposition rate
and the thickness of the deposited layers in a vacuum deposition set-up*"
under the leadership of Conf. Dr. Liviu Giurgiu

1999-2002: PhD Student at Faculty of Physics,
Martin Luther University Halle-Wittenberg, Thesis title:
"*Formation and characterization of metal nanoparticle coating oxide
nanospheres*"
under the leadership of Prof. U. Gösele and Doz. Dr. M. Dubiel.

1996-1998: Research Assistant at Institute of Atomic Physics,
National Institute for Laser, Plasma and Radiation Physics
Solid State Quantum Electronics Laboratory
Chief of Laboratory- Dr.V.Lupei

1998: Physicist at InterNET S.R.L,
Keitley and Stanford Research System representative in Romania

1999-2001: Physicist at Martin Luther University Halle-Wittenberg
Institute for Analytics and Environmental Chemistry

2001-present: Physicist at Max Planck Institute of Microstructure Physics Halle
Nanoparticles and nanophotonics group.

Computer skills: MS Windows, MS DOS, Linux, Microsoft, Microcal Origin, Grace, Mathcad, StarOffice, TeX

Image Processing: CorelDraw, Scion Image, Adobe, Gimp, DigitalMicrograph

Programming Languages: Turbo Pascal, Delphi

Languages spoken: English, German, French, Romanian (native language)

Paul-Tiberiu Miclea

C List of publications

1. A. Dinca, P. T. Miclea, V. Lupei, T. Skettrup, M. P. Dinca
   Multiple solutions provided by analytical synthesis in admittance matching:
   application to dicroic mirrors
   J. Mod. Opt.,**45**, 3 (1997), 605-618
2. A. Dinca, P. T. Miclea, V. Lupei, M. P. Dinca
   Regularities observed among the solutions obtained for two-side optical admittance
   matching
   Proc. Suppl. Balkan Physics Letters, **5**, 3 (1997), 1403-1406
3. A. Dinca, V. Lupei, P. T. Miclea, M. P. Dinca
   Dicroic mirror for high power Nd:YAG laser
   Proc. SPIE, **2889**, (1996), 418-427
4. A. Dinca, P. T. Miclea, V. Lupei, M. P. Dinca
   Solution of the single-layer synthesis with symmetrical three-layer periods
   Proc. SPIE, **3405** (1997), 1162-1165
5. P. T. Miclea, H. Drevs, W. Mörke, K. Lehrack, H. Hofmeister
   Dispersion behaviour of nanosized metal particles on silica by chemical synthesis
   Spring Meeting of German Physcal Society, Regensburg, 2000
6. P. T. Miclea, W. Mörke, K. Lehrack, H. Drevs, H. Hofmeister
   Metal nanoparticles by direct reduction on non-planar silica substrates
   Proc.Autumn School on Material Science and Electron Microscopy Berlin
   (2000), 360-361
7. P. T. Miclea, K. Lehrack, H. Drevs, W. Mörke, H. Hofmeister
   Preparation and characterization of metal nanoparticles coatings on oxide nanospheres
   Spring Meeting of German Physcal Society, Hamburg, 2001
8. P. T. Miclea, K. Lehrack, H. Drevs, H. Hofmeister, W. Mörke,
   Conduction electron spin resonance and electron microscopy study of Rh and Ir
   nanoparticles on hydride silica
   Spring Meeting of German Physcal Society, Berlin, 2001
9. H. Hofmeister, P. T. Miclea, W. Mörke
   Metal nanoparticle coating of oxide nanospheres for core-shell structures
   Particle and Particle Systems Charact., (2002), in preparation